Max-Planck-Institut
für Meteorologie

MAX-PLANCK-GESELLSCHAFT

International Max Planck Research School
on Earth System Modelling

Initialization and predictability of Arctic sea ice in a global climate model

Steffen Tietsche

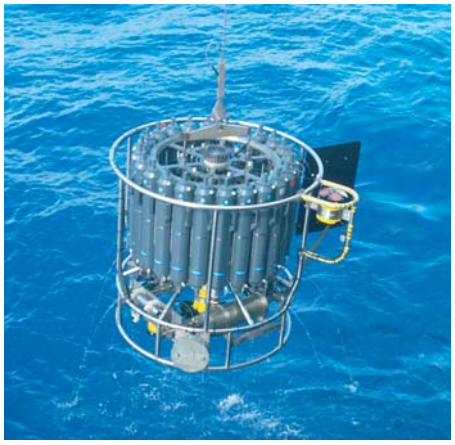

Berichte zur Erdsystemforschung 115/2012

Reports on Earth System Science

Hinweis

Die Berichte zur Erdsystemforschung werden vom Max-Planck-Institut für Meteorologie in Hamburg in unregelmäßiger Abfolge herausgegeben.

Sie enthalten wissenschaftliche und technische Beiträge, inklusive Dissertationen.

Die Beiträge geben nicht notwendigerweise die Auffassung des Instituts wieder.

Die "Berichte zur Erdsystemforschung" führen die vorherigen Reihen "Reports" und "Examensarbeiten" weiter.

Notice

The Reports on Earth System Science are published by the Max Planck Institute for Meteorology in Hamburg. They appear in irregular intervals.

They contain scientific and technical contributions, including Ph. D. theses.

The Reports do not necessarily reflect the opinion of the Institute.

The "Reports on Earth System Science" continue the former "Reports" and "Examensarbeiten" of the Max Planck Institute.

Anschrift / Address

Max-Planck-Institut für Meteorologie
Bundesstrasse 53
20146 Hamburg
Deutschland

Tel.: +49-(0)40-4 11 73-0
Fax: +49-(0)40-4 11 73-298
Web: www.mpimet.mpg.de

Layout:

Bettina Diallo, PR & Grafik

Titelfotos:
vorne:
Christian Klepp - Jochem Marotzke - Christian Klepp
hinten:
Clotilde Dubois - Christian Klepp - Katsumasa Tanaka

Berichte zur Erdsystemforschung 115/2012

Initialization and predictability of Arctic sea ice in a global climate model

SteffenTietsche

aus Potsdam

Hamburg 2012

Reports on Earth System Science 115/2012

ISSN 1614-1199

Steffen Tietsche
Max-Planck-Institut für Meteorologie
Bundesstrasse 53
20146 Hamburg

Als Dissertation angenommen
vom Department Geowissenschaften der Universität Hamburg

auf Grund der Gutachten von
Prof. Dr. Jochem Marotzke
und
Dr. Dirk Notz

Hamburg, den 26. Januar 2012
Prof. Dr. Jürgen Oßenbrügge
Leiter des Departments für Geowissenschaften

ISSN 1614-1199

Initialization and predictability of Arctic sea ice in a global climate model

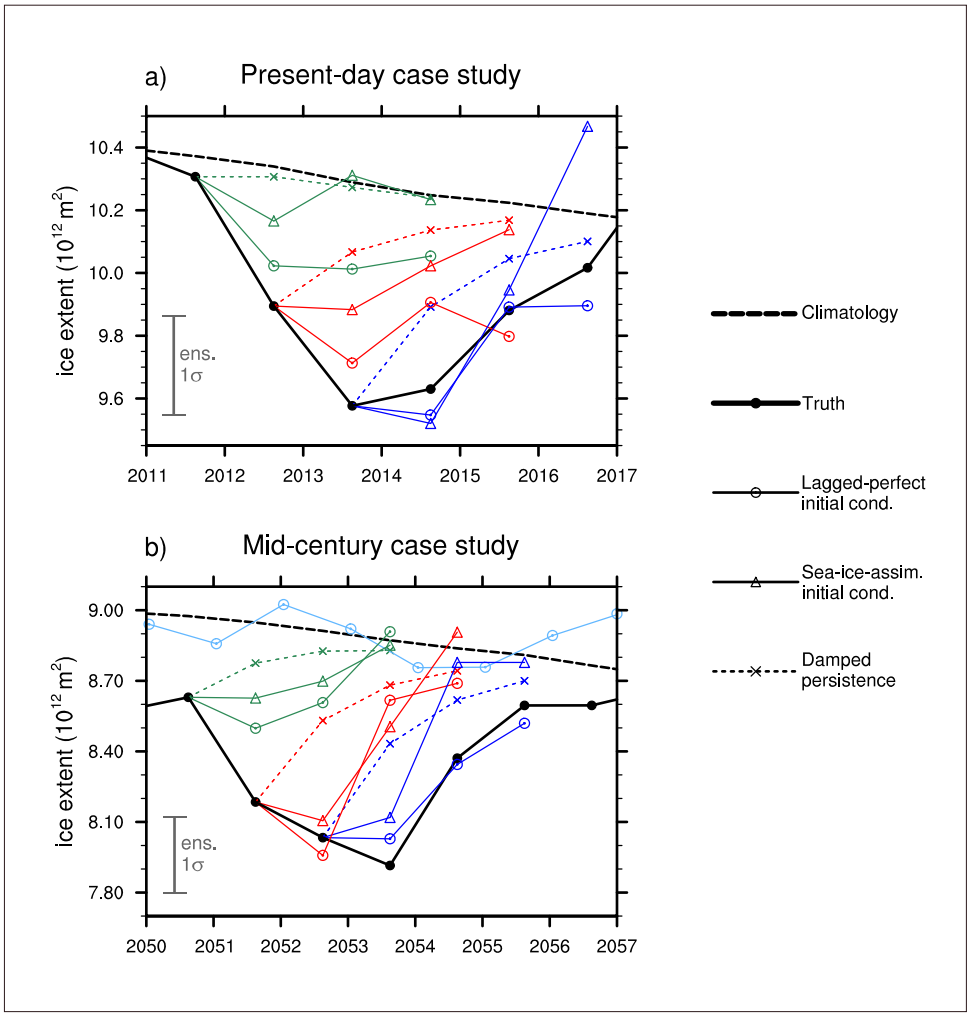

Steffen Tietsche

Hamburg 2012

Abstract

The state of sea ice, which plays an important role in shaping Earth's climate, exhibits vast changes on multiple time scales. For the climate of the present day and the near future, this thesis investigates initialization and predictability of Arctic sea ice in a global climate model (GCM).

To predict the mean state, knowledge of nonlinear thresholds is required, where the mean state changes rapidly and irreversibly. I investigate the existence of such a threshold for the transition between perennial and seasonal sea-ice cover in the Arctic during the 21st century, which could in principle be caused by the destabilizing ice–albedo feedback. I find that Arctic sea ice at all times recovers even from extreme prescribed losses within typically two years, because the large-scale Arctic energy budget adapts to compensate the prescribed anomaly. This indicates that there is no such threshold.

To predict natural variability, knowledge of the initial conditions is required. I investigate the initialization of Arctic sea ice in a GCM by assimilating sea-ice concentration observations. I develop a Newtonian relaxation scheme that successfully constrains concentration and thickness of Arctic sea ice in the GCM to observations. The choice of the assimilation technique is supported by analysis of a conceptual model of local ice growth as well as analysis of assimilation error statistics.

I assess the relative importance of sea-ice initial conditions by performing ensemble predictions under the perfect-model assumption. Predictive skill achievable for Arctic sea ice is comparable between sea-ice-assimilated initial conditions and perturbed-perfect initial conditions for lead times of up to one year. I find that the large interannual negative anomalies that are expected to occur throughout the 21st century are partly predictable for up to three years ahead. However, sea-ice predictability decreases as Arctic sea-ice cover becomes thinner.

Contents

1 Introduction

1.1 Motivation and research questions

In regions of the Earth that are sufficiently cold, sea ice forms from ocean water and floats at its surface. The ice forms an insulating layer that strongly moderates the exchange of heat, momentum and freshwater between the ocean and the atmosphere. It greatly decreases absorption of solar radiation at the surface, since its albedo is much higher than that of the sea water it forms from. The surface-albedo effect of sea ice contributes to the increase of Earth's climate sensitivity [*Rind et al.*, 1995] and to the amplification of climate change in polar regions [*Serreze and Francis*, 2006]. Sea ice affects the atmospheric circulation and surface conditions in mid-latitudes [*Murray and Simmonds*, 1995; *Honda et al.*, 2009]. Regionally, changes in the sea-ice cover have a large impact on highly adapted ecosystems and human societies [*Johannessen and Miles*, 2011].

Throughout Earth's history, the *mean state* of sea ice has undergone vast changes. There were climates with virtually no sea-ice cover at all [*Sluijs et al.*, 2006], and there might have been climates that had the entire ocean surface covered with sea ice [*Hoffman et al.*, 1998]. Owing to the positive ice–albedo feedback, transitions between these different states potentially exhibit critical thresholds, at which the mean state loses stability and a rapid shift to a new mean state occurs (see *McNeall et al.* [2011] for a recent review).

Sea ice exhibits considerable *natural variability*, i.e. fluctuations around its mean state on time scales from single years to many decades. The variability of sea ice is connected with other modes of natural variability in the climate system such as the variability of the meridional overturning circulation, which transports heat into high latitudes [*Jungclaus et al.*, 2005], or the El Niño-Southern Oscillation and

the Arctic Oscillation, which change atmospheric circulation patterns impacting the high latitudes [*Gloersen*, 1995; *Rigor et al.*, 2002].

Today, around 5% of the global ocean surface is ice-covered. In the Arctic, the last decades have seen a strong decrease in sea-ice extent [*Parkinson and Cavalieri*, 2008] and volume [*Kwok and Rothrock*, 2009]. This decrease is thought to be mainly due to a change in the mean state in response to increased greenhouse-gas forcing, but natural variability might have contributed to the decrease as well [*Serreze et al.*, 2007a; *Kattsov et al.*, 2010].

Successful predictions of Arctic sea ice are only possible if the attribution of observed changes either to changes in the mean state or to unforced variability is resolved. For changes in the mean state, the boundary conditions matter. For changes caused by natural variability, the initial conditions matter. These two problems correspond to the two kinds of predictability introduced by *Lorenz* [1975]. Predictability on interannual to decadal time scales is always a mixture of the two [*Collins and Allen*, 2002].

There is an ongoing scientific debate about the existence of a nonlinear threshold for the changing mean state of Arctic sea ice, which would make predictions of the second kind much more uncertain (e.g. *Merryfield et al.* [2008]; *Eisenman and Wettlaufer* [2009]). This debate was spurred by the recent extreme minimum of Arctic summer sea ice in 2007, which seemed to break the trend of sea-ice decline observed in the decades before. Was it the onset of a rapid shift in the Arctic sea-ice mean state caused by the passing of a critical threshold or rather an anomalous random excursion from the slowly changing mean state? This leads to the first set of research questions addressed in this thesis:

> **Does the ice–albedo feedback lead to threshold behavior during the transition of the Arctic Ocean to a seasonally ice-free state? If not, what are the mechanisms that allow the sea ice to recover from anomalous losses?**

To study predictability of the first kind, the initial climate state must be sufficiently well constrained from observations, and suitable data assimilation techniques need to be developed to initialize climate models with the observed climate state [*Schwierz et al.*, 2006; *Hurrell et al.*, 2009]. However, the investigation of sea-ice data

assimilation has mostly been restricted to sea-ice–ocean models lacking an interactive atmosphere (e.g. *Lindsay and Zhang* [2006]; *Stark et al.* [2008]). Furthermore, sea-ice data assimilation is hindered by the sparseness of thickness observations available. The second set of research questions raised in this thesis addresses these open issues:

> **Is it possible to improve the simulation of sea-ice concentration and thickness in a global climate model by assimilating only observations of sea-ice concentration? How do sea-ice concentration and sea-ice thickness interact under different atmospheric and oceanic conditions, and how is this reflected in the choice of appropriate assimilation methods?**

The relative importance of the sea-ice initial state with respect to the initial state of other components of the climate system has to be tested by performing actual predictions on seasonal to decadal time scales. Since the sea-ice cover will very likely continue to shrink in the future [*Arzel et al.*, 2005], and since predictability depends on the initial climate state [*Hermanson and Sutton*, 2009], predictions should be performed at different times during the 21st century. A valuable approach for establishing upper bounds of predictability is the so-called perfect-model assumption. Predictions of Arctic sea ice under the perfect-model assumption have been performed by *Holland et al.* [2010] for perfect initial conditions and present-day conditions. The third set of research questions raised in this thesis takes that discussion one step further:

> **How predictable are large negative interannual anomalies of Arctic sea ice? How much of this predictability can be realized by using initial conditions obtained by the sea-ice assimilation methods developed in this thesis? How does the change in the mean state during the 21st century affect predictability of the first kind?**

1.2 Thesis outline

The main part of this thesis consists of three chapters, which are written in the style of journal publications. Thus, they each contain their own abstract, introduction and conclusions, and can be read independent of one another. The first of these chapters has been published already, the second is submitted for publication, and the third is in preparation for submission.

In **Chapter 2**, I examine the recovery of Arctic sea ice from prescribed ice-free summer conditions in simulations of 21st century climate in the global climate model ECHAM5/MPI-OM. An analysis of the large-scale Arctic energy budget after the perturbation reveals the mechanisms that allow for the recovery. This work has been published in *Geophysical Research Letters*[1] and is reproduced here with minor editorial modifications.

In **Chapter 3**, I investigate the initialization of northern-hemisphere sea ice in ECHAM5/MPI-OM by assimilating sea-ice concentration data. I develop a simple assimilation method based on Newtonian relaxation that also improves the representation of sea-ice thickness. I apply conceptual models and analyse the model background error covariance statistics to better understand the assimilation errors that occur. This work has been submitted for publication in *Journal of Geophysical Research*[2].

In **Chapter 4**, I study the limits of dynamical predictability of Arctic sea ice with the earth system model MPI-ESM-LR and the usefulness of initial conditions obtained by the sea-ice data assimilation methods developed in Chapter 3. I perform ensemble prediction experiments under the perfect-model assumption for cases of extreme negative interannual sea-ice anomalies as they occur in the MPI-M CMIP5 RCP45 climate projections, comparing predictability for present-day conditions to

[1] Tietsche, S., D. Notz, J. H. Jungclaus, and J. Marotzke (2011), Recovery mechanisms of Arctic summer sea ice, *Geophys. Res. Lett.*, *38*, L02707, doi:10.1029/2010GL045698

[2] Tietsche, S., D. Notz, J. H. Jungclaus, and J. Marotzke (2011), Sea-ice data assimilation in a global coupled climate model – physical and statistical aspects, *Journal of Geophysical Research*, submitted

predictability in the middle of the 21st century when the ice pack is much thinner. This work is in preparation for submission to *Journal of Climate*[3].

In **Chapter 5**, I give a concise summary of the main results of this thesis.

[3]Tietsche, S., D. Notz, J. H. Jungclaus, and J. Marotzke (2012), Predictability of large negative Arctic sea-ice anomalies, *Journal of Climate*, in preparation

2 Recovery mechanisms of Arctic summer sea ice

We examine the recovery of Arctic sea ice from prescribed ice-free summer conditions in simulations of 21st century climate in an atmosphere–ocean general circulation model. We find that ice extent recovers typically within two years. The excess oceanic heat that had built up during the ice-free summer is rapidly returned to the atmosphere during the following autumn and winter, and then leaves the Arctic partly through increased longwave emission at the top of the atmosphere and partly through reduced atmospheric heat advection from lower latitudes. Oceanic heat transport does not contribute significantly to the loss of the excess heat. Our results suggest that anomalous loss of Arctic sea ice during a single summer is reversible, as the ice–albedo feedback is alleviated by large-scale recovery mechanisms. Hence, hysteretic threshold behavior (or a "tipping point") is unlikely to occur during the decline of Arctic summer sea-ice cover in the 21st century.

2.1 Introduction

Arctic summer sea-ice extent has decreased substantially in recent years, and it will very likely continue to decrease owing to anthropogenic climate change. Because of the ice–albedo feedback, which reinforces the retreat, the transition from a perennial to a seasonal sea-ice cover might be associated with nonlinear threshold behavior. Nevertheless, other mechanisms stabilize Arctic sea ice [*Notz*, 2009; *Eisenman and Wettlaufer*, 2009], and the present study investigates how these mechanisms lead to the recovery from prescribed ice losses in an atmosphere–ocean general circulation model (AOGCM) for the climate of the near future.

The possibility of multiple equilibria and threshold behavior for polar ice caps, which implies the possibility of abrupt and irreversible changes in polar climate, has long been studied using energy balance models that incorporate the most relevant physical processes [*North*, 1984; *Merryfield et al.*, 2008; *Eisenman and Wettlaufer*, 2009]. The results of those studies, however, depend strongly on the choice and parametrization of large-scale processes. Therefore, studies with AOGCMs are desirable to decide if threshold behavior during the retreat of Arctic sea ice is a robust phenomenon. The IPCC-AR4 model runs provide a wealth of AOGCM projections of Arctic climate for the 21st century, and they do not exhibit clear evidence of a critical threshold for summer sea ice [*Winton*, 2006].

Nevertheless, abrupt partial loss of Arctic summer sea ice is a common feature of those runs [*Holland et al.*, 2006]. Surprisingly, these abrupt partial losses are often followed by an equally rapid temporary recovery. This suggests that Arctic sea ice has a preferred equilibrium state that varies smoothly with the climatic forcing, and that there are recovery mechanisms that counteract the destabilizing ice–albedo effect after abrupt losses.

A valuable tool for understanding those mechanisms are experiments which perturb Arctic sea-ice conditions systematically. To our knowledge, this sea-ice perturbation approach in an AOGCM has so far only been applied by *Schröder and Connolley* [2007], who showed that sea ice recovers from a complete removal within a few years. However, they restricted their experiments to a preindustrial climate and did not address the mechanisms of the sea-ice recovery.

Here, we report the recovery of the Arctic from a prescribed loss of summer sea ice

in the AOGCM ECHAM5/MPI-OM at different times during the 21st century, and investigate the mechanisms of recovery by analyzing the Arctic energy budget. In these perturbation experiments, the initial conditions are such that the ice–albedo feedback, as well as the other feedbacks related to sea-ice anomalies, are most pronounced. Thus, these experiments answer the question of whether perturbations of sea-ice cover alone are able to trigger an irreversible climate change in the Arctic.

2.2 Model and experiments

The global AOGCM we use consists of the atmosphere component ECHAM5 [*Roeckner et al.*, 2003] with a T31 horizontal resolution and 19 vertical levels, and the ocean component MPI-OM [*Marsland et al.*, 2003] with a curvilinear grid that has a horizontal resolution of 50–200 km in the Arctic and 40 vertical levels. A dynamic–thermodynamic sea-ice model based on *Hibler III* [1979] is included. The model setup we use is a coarse-resolution version of the IPCC-AR4 model described by *Jungclaus et al.* [2006]. This higher-resolution model setup has been tested extensively and performs well in simulating Arctic climate [*Chapman and Walsh*, 2007].

We use ECHAM5/MPI-OM to perform a climate projection for the 21st century according to the IPCC-A1B emission scenario [*Nakićenović et al.*, 2000]. In this reference run, annual mean surface air temperature in the Arctic rises from $-14°C$ in the 1900s to $-4°C$ in the 2090s. Arctic sea-ice extent declines, and the Arctic Ocean is typically ice-free by the end of summer from 2070 onward (see Figure 2.1; we note that the sea-ice decline here is somewhat faster than in the higher-resolution version of the model). Between 2000 and 2040, when the rate of decline is maximal, Arctic summer sea-ice extent exhibits strong year-to-year fluctuations. As noted by *Holland et al.* [2008] and *Notz* [2009], this increase in variability is mostly due to changes in the ice thickness distribution and does not necessarily indicate proximity to some critical threshold.

To examine the recovery mechanisms of Arctic summer sea ice, we simulate the consequences of an ice-free Arctic Ocean during summer. We set up experiments to start on 1st July from initial conditions that are taken from the reference run, but are perturbed by converting the entire Northern Hemisphere sea ice to water

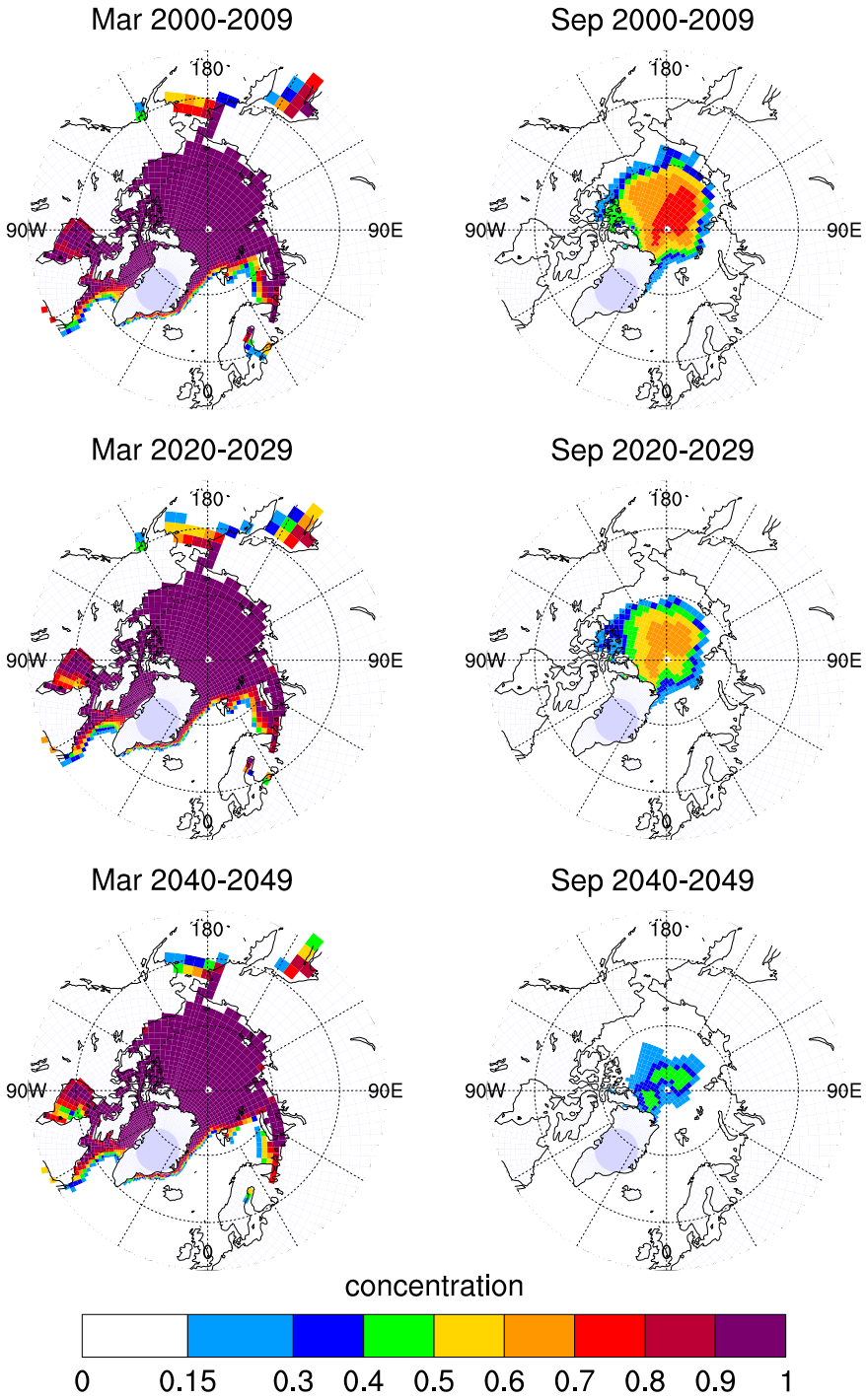

Figure 2.1: Arctic sea-ice concentrations for March and September in the A1B reference run, averaged over the specified decades.

with the same properties as the sea surface water below the ice. Such conversion of relatively fresh sea ice to salty sea water has the advantage of leaving the properties of sea surface water unchanged. The start date is chosen such that the effect of the perturbation is maximal: starting from ice-free conditions earlier in the year leads to immediate re-freezing, and hence both earlier and later start dates imply shorter exposure of open water to sunlight, and a less pronounced ice–albedo effect.

One might expect the Arctic Ocean to stay ice-free after the initial perturbation for several months, and possibly to stay seasonally ice-free in the following years because (i) in July air temperatures are usually above zero, and the ocean accumulates sensible heat throughout summer, (ii) the absence of sea ice implies a large excess of latent heat in the ocean surface layer, (iii) with sea ice absent, the ocean albedo is significantly lowered leading to increased shortwave absorption, and (iv) when cooling starts in autumn, the sea surface water will be more salty, causing convection to reach deeper and delay sea-ice formation.

Every 20 years between 1980 and 2060, three such experiments are started in consecutive years (e.g. 2019, 2020, 2021), so that we can analyze five different time slices with a three-member ensemble each. After the initial perturbation, we let the model run freely without any further manipulation.

In the following, we discuss the development of anomalies that arise due to the modified initial conditions, concentrating on field means over the Arctic Ocean and the atmospheric column above it. We define the Arctic Ocean domain to be bounded by the Bering Strait, the Fram Strait, and by the shortest connection from Spitsbergen to the northern end of Novaya Zemlya continued to the Siberian coast. The resulting area of the Arctic Ocean is $8.4 \cdot 10^{12}$ m^2.

To characterize the time-dependent state of Arctic summer sea ice in the reference run, we quantify it by (i) the centered ten-year running mean of September sea-ice extent $\overline{X}(T)$ and (ii) the centered ten-year running standard deviation of September sea-ice extent $\sigma_X(T)$. We then consider sea-ice extent inside the range of $\overline{X}(T) \pm \sigma_X(T)$ to be typical for the reference run.

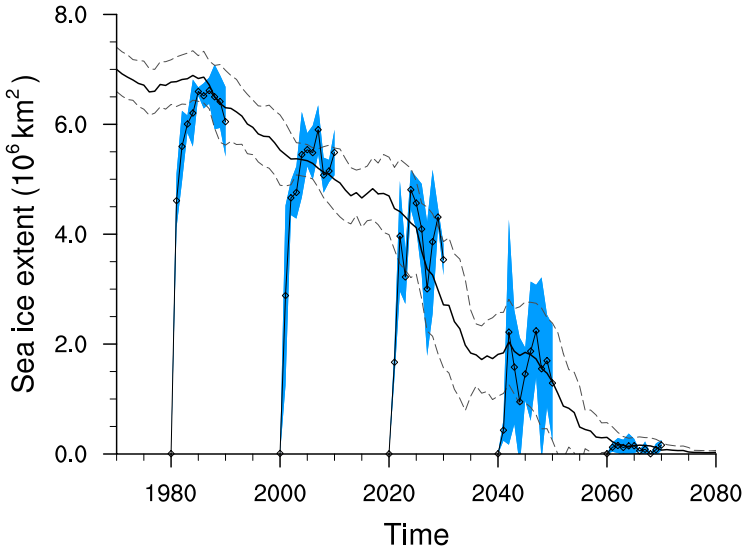

Figure 2.2: September Arctic sea extent. The thick black line is a 10-year moving average of the reference run, the dashed lines enclose the standard deviation of the reference run for the same 10-year window. The mean (diamonds) and the standard deviation (blue shading) of the perturbed model ensemble are shown at the year around which the ensemble is centered.

2.3 Results

2.3.1 Sea-ice extent and temperature anomalies

All our experiments start from sea-ice free conditions on 1st July. As expected, the Arctic Ocean remains ice-free for several months, and significant sea-ice cover does not develop before November. However, sea ice then grows very rapidly, since the growth rate for thin ice is much higher than for thick ice, which acts as a negative feedback on thickness during the growth season [*Bitz and Roe*, 2004; *Notz*, 2009]. The ensemble mean September ice extent reaches values typical for the reference run in the fifth year after the perturbation for the 1980 time slice, in the fourth year for 2000, and already in the second year for 2020 and 2040 (Fig. 2.2). September sea-ice volume takes longer to recover in the late 20th century when the sea ice is still thick, but it has the same time scale of recovery as sea-ice extent from 2000 on (see Figure 2.3). We conclude that there is no threshold in the changing reference state from which on the recovery of sea ice would be inhibited.

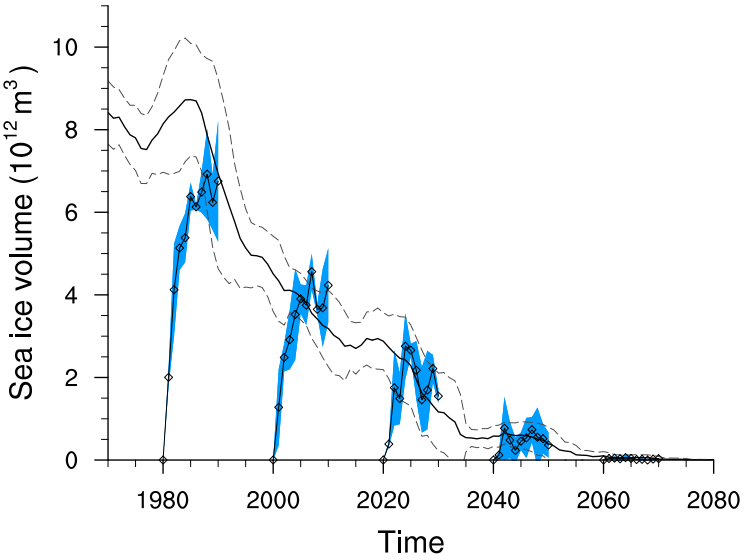

Figure 2.3: September Arctic sea-ice volume. The thick black line is a 10-year moving average of the reference run, the dashed lines enclose the standard deviation of the reference run for the same 10-year window. The mean (diamonds) and the standard deviation (blue shading) of the perturbed model ensemble are shown at the year around which the ensemble is centered.

Sea ice responds similarly to the initial perturbation in all time slices, and we consistently find the same mechanisms to be responsible for the recovery. Therefore, we keep the presentation concise and show only the analysis of the time-slice ensemble starting in 2019/20/21.

We first consider anomalies in surface air temperature (SAT) and sea surface temperature (SST), because they are directly linked to the anomalies in sea-ice cover (Fig. 2.4). At the sea surface, shortwave heating leads to a strong warming in the first summer of the experiment, and in the course of summer this temperature anomaly is mixed to an average depth of 50 m (see Figure 2.5). However, the temperature anomaly does not penetrate deeper, and no excess heat is stored below the surface mixed layer. The water temperature in the uppermost ocean layer (12 m deep) shows a pronounced warming anomaly of 2.7 K, whereas the average temperature of the upper 50 m in the ocean rises by 1.3 K. We note that the magnitude of the ocean temperature anomaly is mainly due to the absence of melting ice that provides a latent heat sink. Without this effect, the surface heat flux anomaly would only

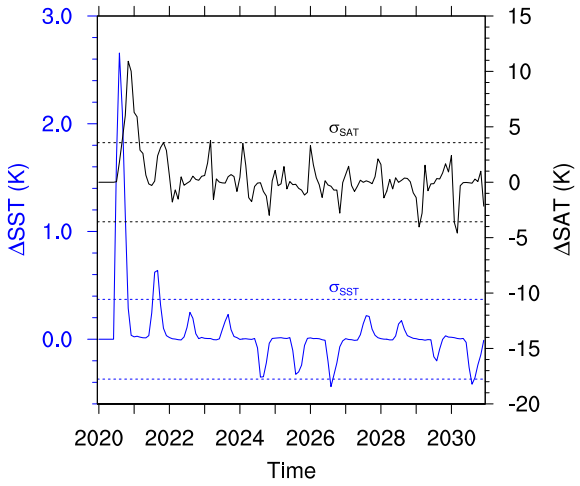

Figure 2.4: The 2020-ensemble mean of the difference in sea surface temperature (ΔSST) and surface air temperatures (ΔSAT) between the experiment and the reference run averaged over the Arctic Ocean domain. The dashed lines indicate the natural variability of the reference run, given by the standard deviation of September temperature in the 2020–2030 decade.

warm the upper 50 m by 0.3 K.

The SST anomaly only lasts until November; by then sufficient heat has been extracted from the surface water to cool it to the freezing temperature. Sea ice then forms from open water very rapidly, and partly recovers. In the next summer the sea-ice cover is still below normal, and larger shortwave absorption leads to a second positive SST anomaly. However, after the second year the SST anomalies are not larger than the natural variability of the reference run.

For SAT a large positive anomaly occurs between October and February after the initial perturbation, with a peak of almost 11 K in November (Fig. 2.4). After February, there are no further SAT anomalies stronger than natural variability. The warming is mainly restricted to the lower troposphere (see Figure 2.6), which is a result that has also been found in GCM studies that prescribed permanent ice-free conditions in the Arctic Ocean [*Royer et al.*, 1990; *Winton*, 2008] and in observations of recent Arctic climate change [*Screen and Simmonds*, 2010]. The peak of the SAT anomaly occurs about four months later than the SST anomaly; the reason for this becomes clear when considering the energy budget.

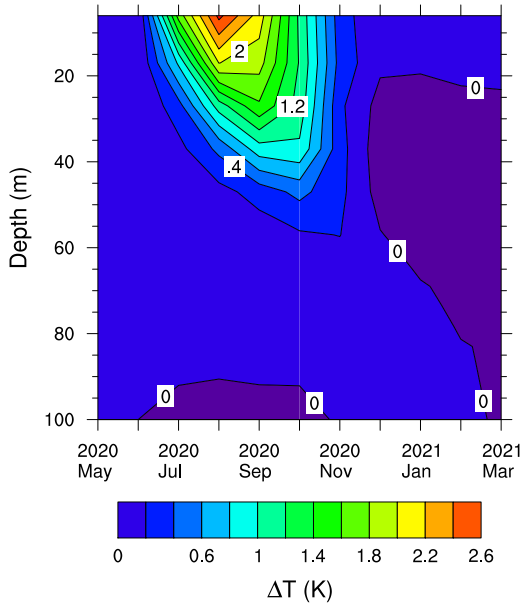

Figure 2.5: Depth profile of the ocean temperature anomaly during the first year after the perturbation for the 2020-ensemble.

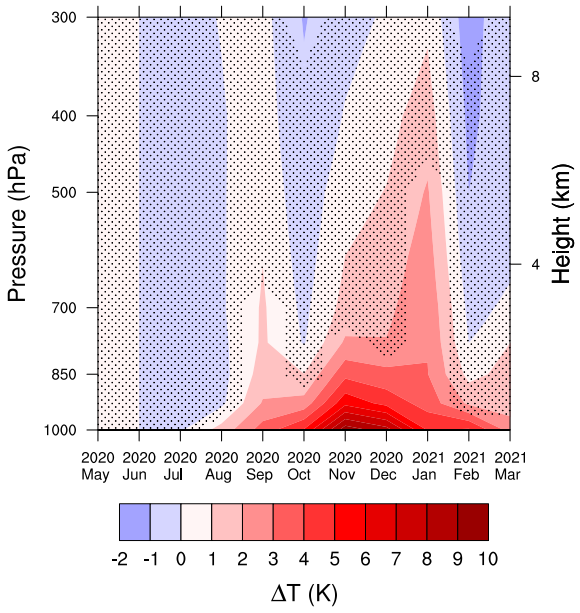

Figure 2.6: Height profile of the atmosphere temperature anomaly during the first year after the perturbation for the 2020-ensemble. In the stippled area, the temperature anomaly is smaller than one standard deviation of the reference run at the respective height and the respective month during the 2020-2030 decade.

2.3.2 Energy budget of the Arctic Ocean domain

In the following, we examine accumulated heat fluxes and heat content changes for the Arctic Ocean domain. For ease of comparison, we introduce the Arctic energy unit $1\,\mathrm{AEU} \equiv 2.21 \cdot 10^{19}\mathrm{J}$, which is the energy accumulated when a heat flux of $1\,\mathrm{Wm}^{-2}$ acts over the area of the Arctic Ocean domain ($8.4 \cdot 10^{12}$ m^2) for one average month (30.5 days). All numbers for energy budget anomalies are rounded to ten AEU, to account for uncertainty arising from energy budget residuals and ensemble spread. The Arctic energy budget anomalies in the experiments are summarized in Fig. 2.7b, a schematic inspired by *Nakamura and Oort* [1988] and *Serreze et al.* [2007b].

We start our discussion of the energy budget anomalies with the oceanic heat transport. As shown by *Serreze et al.* [2007b], heat transport into the Arctic Ocean by advection of warm water and export of sea ice is only between 4 and 7 Wm^{-2} (March and August mean, respectively). Our model shows comparable results for oceanic heat transport into the Arctic. When we compare the reference run to the perturbed run, no significant changes of oceanic heat transport are visible. This is plausible, since immediately after the perturbation, sea surface water has the same properties as in the reference run. During summer warming a temperature anomaly develops, and during winter freeze-up a salinity anomaly develops, but the resulting density anomaly is small compared to the seasonal cycle. Hence, we find that anomalies in oceanic heat transport into the Arctic are unimportant for the observed recovery of the Arctic energy budget.

Consequently, the oceanic heat content anomaly is determined by the remaining two factors: (i) the latent heat anomaly induced by the initial conditions of the experiment and (ii) the surface heat flux anomaly. The latent heat anomaly for the 2020 experiment has a magnitude of 130 AEU. The ability of the Arctic Ocean to store this excess heat over the course of winter is the key determinant for the evolution and stability of Arctic sea-ice cover [*Serreze and Francis*, 2006]. When starting from ice-free conditions on 1st July, the ice–albedo effect at first reinforces the ocean heat content anomaly: net shortwave heat flux is strongly increased by about $25\,\mathrm{Wm}^{-2}$, whereas the upward heat fluxes are only increased by $5\,\mathrm{Wm}^{-2}$ (Fig. 2.7a). However, from September on the effect of shortwave flux is negligible,

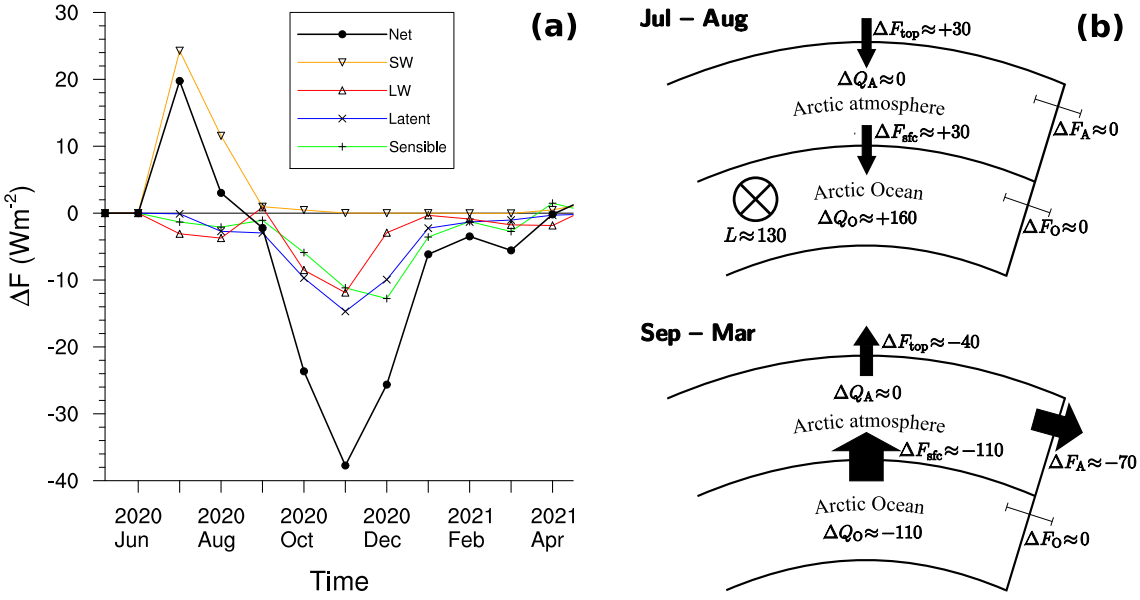

Figure 2.7: Mean energy budget anomalies for the Arctic Ocean domain. Shown are the values of the 2020 time-slice experiments for the first nine months after starting from ice-free conditions on 1st July. (a) Downward surface heat flux anomaly. (b) Atmospheric and oceanic energy budget anomalies for the Arctic. All numbers are in energy units of $1\,\mathrm{AEU} \equiv 2.21 \cdot 10^{19}\mathrm{J}$, which corresponds to the energy accumulated by a flux of $1\,\mathrm{Wm}^{-2}$ into the area of the Arctic Ocean domain during one month. Numbers are rounded to ten. Arrow widths are proportional to size of anomalies. Top: summer phase (July to August). Bottom: winter phase (September to March). Definition of symbols: ΔF_{top} is accumulated top-of-atmosphere net heat flux anomaly; ΔF_{sfc} is accumulated net surface heat flux anomaly; $\Delta F_{A/0}$ is accumulated atmospheric/oceanic lateral heat transport anomaly; $\Delta Q_{A/O}$ is the anomaly of atmospheric/oceanic heat content change; L is the latent heat anomaly of the ice-free initial conditions.

and the upward heat fluxes at the surface are increased with a peak anomaly of almost $40\,\mathrm{Wm}^{-2}$ in November. Thus, sea-ice free summer conditions cause the ocean to gain excess heat through the surface during summer, but they also cause enhanced heat loss through the surface in the following autumn and winter, when the insulating sea-ice cover is anomalously thin.

The atmospheric energy budget anomaly is tightly coupled to the surface heat flux. During the summer phase from July to August, when the downward surface heat flux is amplified, the atmosphere only plays a passive role: the excess shortwave absorption of 30 AEU at the surface is balanced by an increase of net shortwave flux at the top of the atmosphere. Atmospheric heat content and lateral heat transport are not significantly affected (Fig. 2.7b). However, during the longer winter phase from September to March, when the upward surface heat flux is amplified, the warming of the atmosphere leads to a decreased atmospheric heat transport into the Arctic Ocean domain by 70 AEU. At the same time, more longwave radiation is emitted at the top of the atmosphere, which accumulates to 40 AEU.

2.4 Conclusions

In our perturbation experiments, we observe how different feedbacks in the Arctic compete to enhance or dampen a strong negative anomaly in sea ice, equivalent to a strong positive anomaly in oceanic heat content. In summer, the oceanic heat anomaly is enhanced by the ice–albedo feedback, but in winter the excess oceanic heat is lost to the atmosphere due to a lack of insulating sea-ice cover. This leads to an anomalously warm atmosphere, which in turn causes increased heat loss by longwave radiation at the top of the atmosphere and decreased heat gain by atmospheric advection from lower latitudes. A lasting impact of the ice–albedo feedback is not possible because the large-scale heat fluxes quickly adapt to release the excess oceanic heat from the Arctic.

Hence, we find that even dramatic perturbations of summer sea-ice cover in the Arctic are reversible on very short time scales of typically two years. This suggests that a so-called tipping point, which would describe the sudden irreversible loss of Arctic summer sea ice during warming conditions, is unlikely to exist.

These results also have implications for the value of sea-ice initial conditions for climate predictions on decadal time scales: if even the strong anomalies in sea-ice cover that we examine here are reversible within a few years, then small errors in sea-ice initial conditions should not affect the predictions significantly. Intrinsic memory of the thin Arctic sea-ice cover of the 21st century seems to span only a few years.

3 Sea-ice data assimilation in a global climate model – physical and statistical aspects

We investigate the initialization of northern-hemisphere sea ice in the global climate model ECHAM5/MPI-OM by assimilating sea-ice concentration data. The analysis updates for concentration are given by Newtonian relaxation, and we discuss different ways of specifying the analysis updates for mean thickness. Because the conservation of mean ice thickness or actual ice thickness in the analysis updates leads to poor assimilation performance, we introduce a proportional dependence between concentration and mean thickness analysis updates. Assimilation with these proportional mean-thickness analysis updates significantly reduces assimilation error both in identical-twin experiments and when assimilating sea-ice observations, reducing the concentration error by a factor of four to six, and the thickness error by a factor of two. To understand the physical aspects of assimilation errors, we construct a simple prognostic model of the sea-ice thermodynamics, and analyze its response to the assimilation. We find that the strong dependence of thermodynamic ice growth on ice concentration necessitates an adjustment of mean ice thickness in the analysis update. To understand the statistical aspects of assimilation errors, we study the model background error covariance between ice concentration and ice thickness. We find that the spatial structure of covariances is best represented by the proportional mean-thickness analysis updates. Both physical and statistical evidence supports the experimental finding that proportional mean-thickness updates are superior to the other two methods considered and enable us to assimilate sea ice in a global climate model using simple Newtonian relaxation.

3.1 Introduction

For skillful seasonal to decadal predictions, good initial conditions of atmosphere–ocean global climate models (AOGCMs) are of paramount importance. So far, global prediction studies have been restricted to the initialization of the oceanic and atmospheric state (e.g., *Smith et al.* [2007]; *Pohlmann et al.* [2009]). However, slow surface processes might constitute a substantial source of untapped predictability [*Hurrell et al.*, 2009; *Shepherd et al.*, 2011]. One of the most important of these surface processes is arguably the existence of sea ice at high latitudes. *Holland et al.* [2010] and *Blanchard-Wrigglesworth et al.* [2011a] have shown that Arctic sea ice has inherent predictability of up to two years. Moreover, anomalies in Arctic sea ice can have an influence far beyond the Arctic by changing the large-scale atmospheric circulation [*Honda et al.*, 2009; *Budikova*, 2009] and the oceanic thermohaline circulation [*Koenigk et al.*, 2006; *Levermann et al.*, 2007]. Hence, the initialization of sea ice in an AOGCM with suitable data assimilation techniques is an important step towards more skillful seasonal to decadal predictions. Here, we investigate data assimilation techniques for the initialization of northern-hemisphere sea ice in the AOGCM ECHAM5/MPI-OM.

The most important parameters of sea ice are the *sea-ice concentration*, which is the fraction of surface area covered by sea ice, and the *sea-ice mean thickness*, which is the volume of sea ice present per surface area. While the observational record of ice concentration in the Arctic is dense in space and time and relatively reliable since the late 1970s, observations for ice thickness are sparse. Hence, sea-ice data assimilation suffers from a large uncertainty about the true thickness. Initial conditions derived from the assimilation inherit this uncertainty, which in turn severely limits the reliability of sea-ice predictions.

Previous studies have demonstrated that the assimilation of observed sea-ice concentration in ice–ocean models improves the simulated concentration [*Lisæter et al.*, 2003; *Lindsay and Zhang*, 2006; *Stark et al.*, 2008]. However, the improvement in ice thickness is not straightforward, and *Dulière and Fichefet* [2007] emphasized that the assimilation can easily deteriorate the model performance if inappropriate assimilation techniques are chosen.

These findings from ice concentration assimilation in ice–ocean models forced by

atmospheric surface conditions cannot be directly transferred to ice-concentration assimilation in AOGCM, because in AOGCM the atmospheric surface conditions are not necessarily consistent with the assimilated sea-ice state. Rather, they develop interactively from large-scale dynamics and from local interaction with the sea-ice state. This makes the impact of ice-concentration assimilation on ice thickness less obvious and calls for dedicated studies on sea-ice data assimilation in AOGCM. However, to our knowledge, the only such published study is by *Saha et al.* [2010], who did not describe the impact of the ice concentration assimilation on ice thickness.

Here, we assimilate observations of northern hemisphere sea-ice concentration and compare different methods of prescribing changes in mean ice thickness associated with changes in ice concentration during the assimilation step. We systematically assess the assimilation performance both for concentration and thickness, and use conceptual arguments to explain the differences in assimilation performance.

The rest of the paper is organized as follows: Section 3.2 describes the global climate model used for this study, in particular the sea-ice component. Section 3.3 introduces the sea-ice data assimilation methods which we use to investigate feasibility of sea-ice data assimilation. The assimilation performance is evaluated first in a perfect-model framework (Sec. 3.4) and then with actual observations of sea-ice concentration (Sec. 3.5). Section 3.6 uses both simple models and AOGCM case studies to develop a conceptual understanding of assimilation errors, while Section 3.7 analyzes the model error statistics. Section 3.8 presents conclusions.

3.2 The coupled global climate model

3.2.1 The atmosphere and ocean models

Our AOGCM consists of the atmosphere component ECHAM5 [*Roeckner et al.*, 2003] with a T31 horizontal resolution and 19 vertical levels, and the ocean component MPI-OM [*Marsland et al.*, 2003] with a curvilinear grid that has a horizontal resolution of 50–200 km in the Arctic and 40 vertical levels. The time step of the atmosphere model is 40 minutes, the time step of the ocean and sea-ice models is 144 minutes. The ocean and atmosphere exchange surface fields once a day before the first time step. The model setup is a coarse-resolution version of the IPCC-AR4

model described by *Jungclaus et al.* [2006].

3.2.2 The sea-ice model

The sea-ice model in ECHAM5/MPI-OM is based on *Hibler III* [1979] and *Semtner* [1976]. It consists of three prognostic equations for the mean ice thickness $h_m(x, y, t)$, the ice concentration $C(x, y, t)$, and the ice velocity $\mathbf{v}(x, y, t)$:

$$\partial_t h_m = \nabla \cdot (h_m \mathbf{v}) + S_h \tag{3.1}$$

$$\partial_t C = \nabla \cdot (C\mathbf{v}) + S_C \tag{3.2}$$

$$\partial_t \mathbf{v} = -f(\mathbf{k} \times \mathbf{v}) - g\nabla\zeta + \frac{\boldsymbol{\tau}_a}{\rho_i h_m} + \frac{\boldsymbol{\tau}_o}{\rho_i h_m} + \nabla \cdot \boldsymbol{\sigma} \tag{3.3}$$

The divergence terms on the right-hand side of (3.1) and (3.2) describe the redistribution of ice volume and concentration by advection with ice velocity $\mathbf{v}$. S_h and S_C are the thermodynamic sources of mean thickness and concentration, respectively, which describe local melting and freezing. The change of ice velocity $\mathbf{v} = (v_x, v_y)$ is determined by the momentum balance (3.3), where f is the Coriolis parameter, $\mathbf{k}$ the vertical unit vector, g the Earth's gravitational acceleration, ζ the sea surface height above sea level, ρ_i the ice density, $\boldsymbol{\tau}_{a/o}$ the stress of wind from above and ocean current from below, and $\boldsymbol{\sigma}$ the sea-ice internal stress tensor. The terms on the right-hand side of (3.3) from left to right correspond to forces that originate in the Coriolis effect, the tilt of the sea surface, the drag from atmosphere and ocean, and internal sea-ice stresses.

These equations are based on the model assumption that within a grid cell, a fraction C of the area is covered by ice with the constant thickness h_t, given by

$$h_t = h_m / C, \tag{3.4}$$

and the remaining fraction $1-C$ of the area is open water. It is further assumed that the sea water in a grid cell that contains sea ice is always at a representative sea-water freezing temperature of $-1.9\,^{\circ}\mathrm{C}$. Thus, any heat flux imbalance over either the ice-covered or the open-water part of the grid cell is immediately converted into ice growth or melt, and so the thermodynamic source of mean ice thickness in eq.

(3.1) is given by

$$S_h = Cg_i + (1 - C)g_w. \tag{3.5}$$

The two different growth rates, g_i for the ice-covered part of the grid cell and g_w for the open water part, are calculated from the surface energy balance of the coupled model, assuming a linear temperature profile within the ice [*Semtner*, 1976].

The thermodynamic source term for ice concentration S_C is parametrized in terms of the ice growth rates according to *Hibler III* [1979]:

$$S_C = \Theta(g_w)\frac{g_w}{h_0}(1 - C) + \Theta(-S_h)\frac{C}{2h_m}S_h, \tag{3.6}$$

with Θ the Heaviside step function (i.e. $\Theta(x) = 1$ if $x \geq 0$, $\Theta(x) = 0$ if $x < 0$). The first term on the righthand-side of (3.6) is active when new ice forms from open water; the parameter $h_0 = 0.5\,\mathrm{m}$ is chosen such that open water freezes over within a few days if there is strong ice growth, which is consistent with observations. The second term approximates the decrease in ice concentration when thick ice melts, assuming that the thickness of the ice floe is distributed linearly between 0 and $2h_t$.

3.3 Sea-ice data assimilation approach

In this study, we exclusively utilize daily data of Arctic sea-ice concentration. In Sec. 3.4, these data are derived from model output, whereas in Sec. 3.5 they are derived from satellite observations. For the concentration analysis updates, we choose here the simplest possible approach: the Newtonian relaxation of the model state towards observations. This approach is feasible here since sea-ice concentration observations are both dense and relatively reliable. The analysis updates of other sea-ice related variables like mean ice thickness, sea surface temperature, and sea surface salinity are derived from the concentration analysis updates.

We perform long assimilation runs for the period 1979–2007, spanning almost the entire satellite observational record of northern hemisphere sea-ice concentration. We primarily consider the global performance of sea-ice data assimilation, averaged over different regions and different years, rather than focus on specific case studies. On the one hand, this complicates the attribution of failure or success of a method

to physical causes, since we deal with the average over a plethora of different local conditions. On the other hand, we can verify that there are no spurious drifts in the AOGCM induced by the sea-ice data assimilation and that the performance is robust over a range of climatic conditions.

In the following, we use the notation of *Bouttier and Courtier* [1999] and denote the model background state of a variable x by x^b, the analysis by x^a, and the analysis update by $\Delta x = x^a - x^b$.

3.3.1 Analysis updates of ice concentration

We obtain the analyzed sea-ice concentration C^a once a day by correcting the model background concentration C^b with an analysis update ΔC that corresponds to Newtonian relaxation towards observed values C^o:

$$C^a = C^b + \Delta C \quad \text{with} \quad \Delta C = K_N(C^o - C^b). \tag{3.7}$$

The scalar constant K_N determines the strength of the analysis update. We choose $K_N = 0.1$. This approach is akin to data assimilation by nudging, where the same analysis update would be applied at each time step of the model. In the absence of model tendencies, the analysis update (3.7) leads to the exponential relaxation of an initial departure of the model background state from the observation on a *relaxation time scale* of $T_R = 10\,\text{days}$.

3.3.2 Analysis updates of mean ice thickness

We consider analysis updates of mean ice thickness h_m as a function of analysis updates of ice concentration:

$$h_m^a = h_m^b + \Delta h_m \quad \text{with} \quad \Delta h_m = f(\Delta C) \tag{3.8}$$

Our motivation to follow this approach is twofold: (i) reliable and dense satellite observation of mean ice thickness are not available to date, and (ii) anomalies in ice concentration and mean ice thickness have a very high correlation of 0.7 averaged over the Arctic, as diagnosed from a long AOGCM run (not shown). By choosing f

so that it approximates those correlations, we can try to estimate the mean thickness from observation of sea-ice concentration alone.

As we will see in Sections 3.4 and 3.5, the assimilation error differs substantially between different choices for the functional dependence f, and in Sections 3.6 and 3.7 we will discuss possible sources of assimilation errors in detail. We introduce and discuss the following three choices:

Analysis updates with conserved mean thickness (CMT) With this method, the analysis update of mean ice thickness h_m is always zero, no matter the value of the concentration analysis update:

$$\Delta h_m = 0. \tag{3.9}$$

The analyzed actual ice thickness h_t^a is then given by $h_t^a = h_t^b \, C^b/C^a$. From idealized experiments with prescribed perturbations in thermodynamic atmospheric forcing, *Dulière and Fichefet* [2007] concluded that this is the best approach when model error is mainly due to ice advection.

Analysis updates with conserved actual thickness (CAT) We assume that the model has the correct actual ice thickness h_t, and demand that $\Delta h_t \equiv h_t^a - h_t^b \stackrel{!}{=} 0$. Applying eqs. (3.4) and (3.8), we see that this is guaranteed if we choose

$$\Delta h_m = h_t^b \Delta C. \tag{3.10}$$

$h_t^b = h_t^b(x, y, t)$ is the spatially and temporally varying actual thickness in the model background. Thus, for the same concentration analysis update, mean-thickness analysis updates will be small for low background actual thickness, and large for high background actual thickness. *Dulière and Fichefet* [2007] found that this method performs best when model error is mainly due to ice thermodynamics.

Proportional mean thickness analysis updates (PMT) *Dulière and Fichefet* [2007] report best assimilation results for a combination of CMT and CAT, depending on whether errors are related to errors in the thermodynamic or the dynamic forcing of the sea ice. However, in an AOGCM the attribution of errors in the sea-ice

state to either dynamical or thermodynamical processes is not practicable. Hence, we propose a simple new scheme that – as we will show – performs well independent of the source of the errors. This is a scheme where the mean-thickness analysis updates have a fixed proportionality to the concentration analysis updates:

$$\Delta h_m = h^* \Delta C. \tag{3.11}$$

The proportionality constant h^* is a free parameter. In our experiments, we use a value of $h^* = 2\,\mathrm{m}$. That means that for an assimilation update of 1 % we change the mean ice thickness by 2 cm. However, we found that the assimilation performance is not very sensitive to changing h^* in the range $0.5\,\mathrm{m} \leq h^* \leq 4\,\mathrm{m}$. Our choice of h^* is supported by the frequency of occurrence of mean thickness and concentration in the AOGCM (Section 3.6.4) and the model background error covariance between concentration and thickness diagnosed from the AOGCM (Section 3.7).

3.3.3 Analysis updates of sea-surface temperature and salinity

Growth and melt of sea ice are strongly coupled to the properties of the sea water directly below and adjacent to the ice. Thus, sea-ice data assimilation schemes for a model with a prognostic ocean need to find a satisfying solution to adjust sea surface salinity (SSS) and sea surface temperature (SST) when changing the sea-ice state through the analysis updates.

In ECHAM5/MPI-OM, the assimilation of SST in the presence of sea ice is implicitly provided by the assumption of thermodynamic equilibrium between sea ice and the water in the ocean surface layer. If sea ice is present in the observations, but not in the model, positive analysis updates of ice concentration merely lead to a decrease in SST until the freezing point is reached. In this case, analysis updates for sea ice are effectively zero, while we have negative analysis updates of SST. As soon as ice starts to form, SST stays constant at the freezing temperature, and the analysis updates change only the sea-ice concentration and thickness.

The SSS plays an important role for the establishment or inhibition of oceanic convection in the presence of sea ice. If there is convection, the entrainment of warm water from below during the deepening of the surface mixed layer can inhibit ice

growth considerably (see, for instance, *Lemke* [1987]). Since growth and melt of sea ice provide substantial freshwater fluxes into the ocean surface water, the treatment of SSS in the analysis update will strongly interact with the sea-ice analysis. The character of this interaction, however, is very variable and depends on the specific local conditions. Since the covariance between ice concentration and SSS shows such a high degree of complexity [*Lisæter et al.*, 2003], it is not feasible to prescribe a global time-independent functional relation between the analysis updates that exploits the existing covariance structures. We therefore restrict ourselves to the most simple approach: whenever mean ice thickness is changed in the analysis update, we adjust the salinity of the surface ocean layer such that the analysis update does not introduce artificial sources or sinks of salt.

3.4 Assimilating sea-ice data in a perfect model

3.4.1 Rationale and method

When assimilating observed sea-ice concentration in an AOGCM, we face two basic problems: (i) the ice thickness and the state of the ocean below sea ice are poorly observed, hence we cannot determine if the assimilation improves those variables, and (ii) we cannot decide if problems in the assimilation are due to drawbacks in the assimilation scheme, or due to model biases.

Those issues can be addressed in a so-called perfect-model study. In the data assimilation context, this means that we treat model output from a reference run as observations, and assimilate it back into a different run of the same model. When both model runs start from different but climatologically equivalent initial conditions and are exposed to the same external forcing, the model is perfect with respect to the reference-run observations. This allows us to disentangle the effects of model bias and data assimilation method and to answer the question, "If the model were perfect, would we be able to initialize it successfully with a given data assimilation approach?".

The reference run R is started from a long control run with preindustrial conditions, and then exposed to the observed greenhouse-gas forcing from 1900 onwards. In the reference run, the overall decrease of northern-hemisphere sea-ice extent is

comparable to observations, although the retreat of summer-time sea ice is somewhat underestimated. A detailed description of the deficiencies of the IPCC-AR4 version of this model in simulating northern-hemisphere sea ice is given by *Koldunov et al.* [2010].

From the reference run, we branch off a perturbed run P in 1979. The applied perturbation is very small but is quickly amplified by chaotic processes, and we obtain an equivalent but different realization of natural climate variability in the perturbed run. Important large-scale modes of climate variability, like ENSO, the slow components of the Atlantic meridional overturning circulation, and interannual variations in sea-ice cover are out of phase between the two runs.

The assimilation run A starts from the same initial conditions as the perturbed run P, but assimilates the ice concentration from the reference run R. The time period considered is 1979 to 2007, so that we can later compare the assimilation of ice concentration from model output to the assimilation of ice concentration from satellite observations.

To quantify the usefulness of the data assimilation, we measure the mismatch of a climate variable X between any two timeseries with the root–mean–square differences between the two timeseries:

$$\delta X_{T_1 T_2} = \sqrt{\langle (X_{T_1}(t) - X_{T_2}(t))^2 \rangle}. \tag{3.12}$$

The expectation value $\langle \cdot \rangle$ is meant to be taken over time for aggregated quantities like northern-hemisphere sea-ice extent, and over time and space for field variables like sea-ice concentration.

Using (3.12), we can compare the natural variability δX_{RP} with the assimilation error δX_{RA}. Only if $\delta X_{RA} < \delta X_{RP}$ does the assimilation actually improve the initialization of X in the model. For a perfect initialization of X, we would have $\delta X_{RA} = 0$.

3.4.2 Results

The most relevant quantities when investigating sea-ice data assimilation are the mean ice thickness h_m and the ice concentration C. In the following, we will therefore

restrict ourselves to quantifying the improvement of these quantities.

Fig. 3.1 shows how successfully the different assimilation schemes allow the assimilation run A to match the yearly-mean sea-ice extent and sea-ice volume of the reference run R. The reference run has generally decreasing sea-ice extent and sea-ice volume in response to the warming background climate. Additionally, there are year-to-year variations as well as decadal-scale variations in the sea-ice state. For instance, between 1988 and 1991 sea-ice extent increases, stays relatively high until 1998, and then drops sharply to the lowest value of the time series in 2000. We consider a sea-ice data assimilation successful only if (i) A has the same climatology as R, i.e. the multi-year running means are the same, (ii) A shows similar decadal-scale anomalies as R, and (iii) A has year-to-year anomalies comparable to R.

The CMT assimilation scheme fails in all three criteria: it does not reproduce the decreasing trend in sea-ice volume, the period between 1984 and 1992 that should see a negative anomaly in sea-ice volume actually has a positive anomaly, and the small year-to-year fluctuations are not captured at all. The CAT run has a negative bias, but reasonably captures year-to-year and decadal variations. Finally, the PMT run meets all three criteria set above, and by far provides the best assimilation performance.

Table 3.1 shows the time-averaged error in sea-ice extent δSIE and sea-ice volume δSIV as defined in eq. (3.12). Although all assimilation methods decrease the error in sea-ice extent with respect to the reference run, we see that only PMT reduces the error in sea-ice volume below the level set by natural variability (no assimilation).

To analyze the seasonal cycle of the assimilation errors, we calculate the discrepancy in concentration δC and mean thickness δh_m for the Arctic Ocean with eq. (3.12), taking the time mean separately for each month of the year (Fig. 3.2). Since the Arctic Ocean is essentially ice-covered during winter, even the no-assimilation run exhibits only small natural variations in sea-ice concentration, with $\delta C_{RP} \approx 5-8\,\%$. The summer melt, however, is much more variable, and concentration variability in the no -ssimilation run reaches 24% in September and October. Clearly, all assimilation methods are able to significantly reduce the concentration discrepancy δC, although there are marked differences between the methods. The CMT gives the worst performance, and the PMT gives the best performance, reducing concentration error to about 5% year-round.

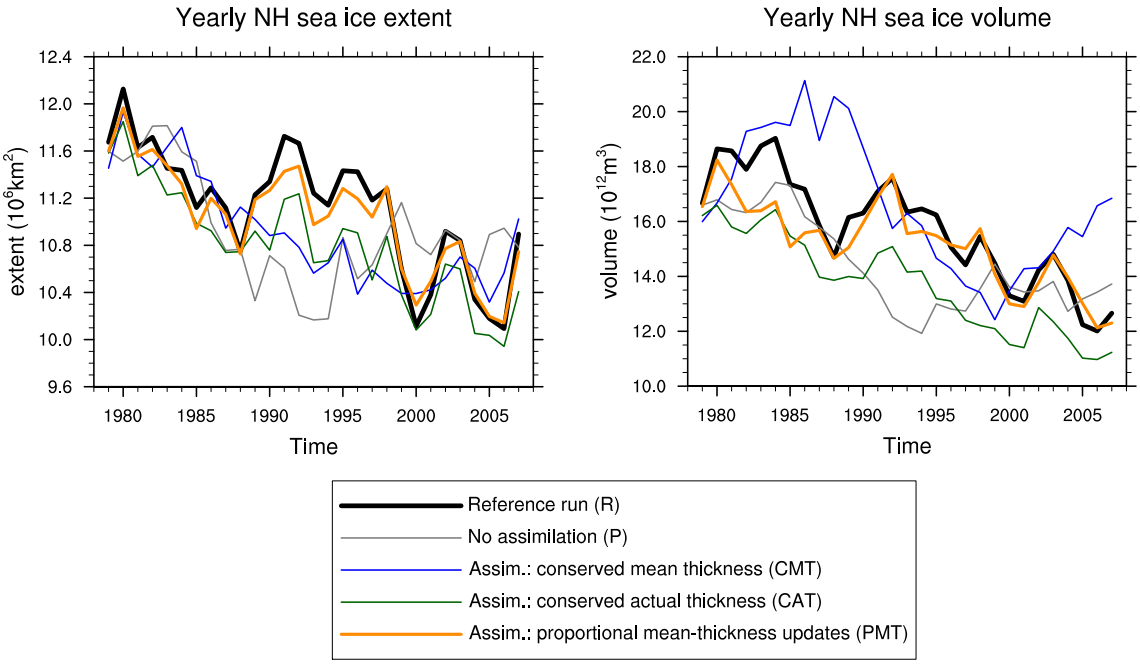

Figure 3.1: Yearly-mean sea-ice extent (left) and sea ice volume (right) in the northern hemisphere for the perfect-model study. Shown are the reference run (black), the perturbed run with no assimilation (gray), and the assimilation runs (colors) that assimilate sea-ice concentration from the reference run. The corresponding time-averaged global extent and volume errors δSIE and δSIV are given in Table 3.1.

	Perfect model		Observations
	δSIV(10^{12}m^3)	δSIE (10^{12}m^2)	δSIE(10^{12}m^2)
no assimilation	2.1	0.6	0.4
CMT assimilation	2.4	0.5	0.5
CAT assimilation	2.1	0.4	0.4
PMT assimilation	1.0	0.1	0.1

Table 3.1: Comparison of the time-averaged difference in ice extent and ice volume between a reference run and (i) a run without data assimilation, (ii) an assimilation with conservation of mean thickness (CMT), (iii) an assimilation with conservation of actual thickness (CAT), and (iv) an assimilation with proportional mean-thickness updates (PMT).

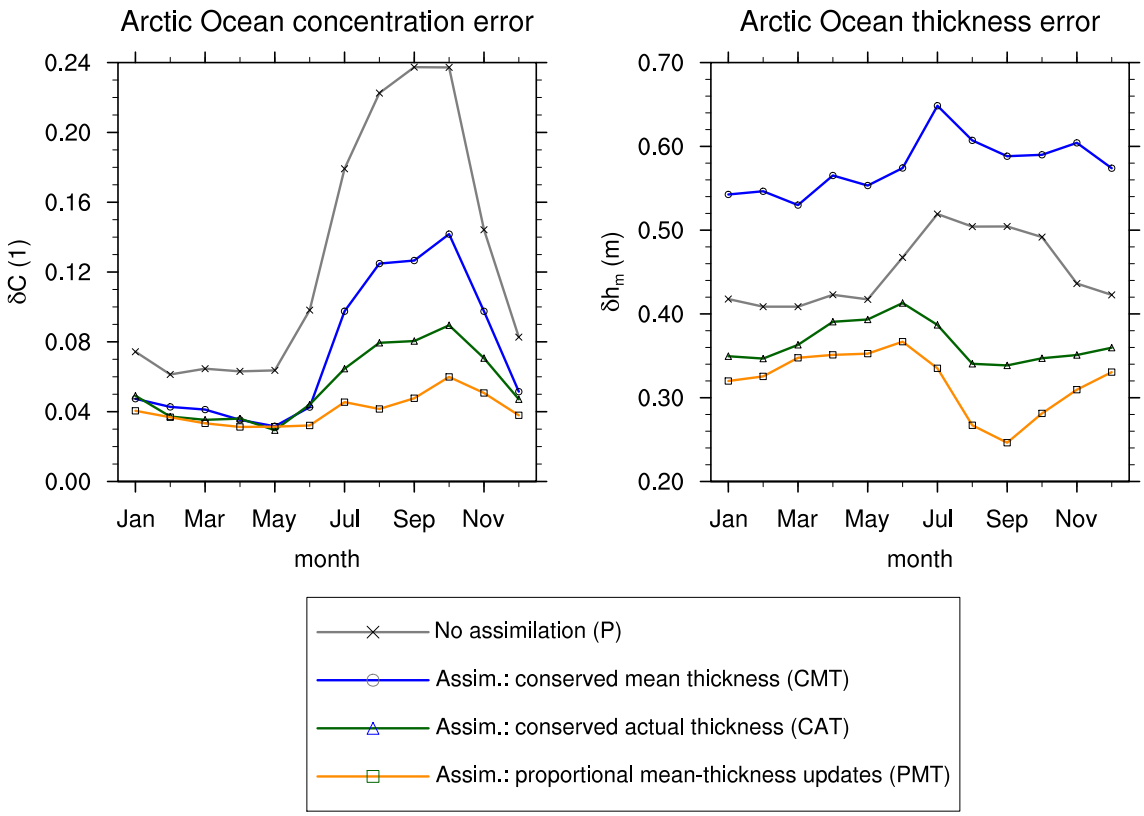

Figure 3.2: The average point-wise root-mean-square error in sea-ice concentration δC (left) and sea-ice mean thickness δh_m (right) in the Arctic Ocean for each month of the year for the perfect-model study. All errors are obtained from the differences to the reference run.

The error in mean thickness δh_m is shown in the right panel of Fig. 3.2. The natural variability $\delta h_m(R, P)$ is about 40 cm in winter and about 50 cm in summer. It is evident that the CMT does not decrease, but even *increases* the error of mean ice thickness, i.e. $\delta h_m(R, P) < \delta h_m(R, A)$. This is quite a dramatic failure of the data assimilation method. In Sections 3.6 and 3.7 we will see that there are good conceptual arguments why the CMT is not a suitable assimilation method in an AOGCM. The two other methods (CAT and PMT) successfully reduce the thickness error. Again, PMT has the lowest thickness error; it is about $25-30$ cm year-round. Note that the assimilation is most successful in summer, as it halves the error in the mean ice thickness compared to the natural variability.

3.5 Assimilating sea-ice observations

We now investigate how successfully we can assimilate satellite observations of sea-ice concentration into the coupled climate model. The observations are derived from Nimbus-7 SMMR and DMSP SSM/I passive microwave data, processed by the NSIDC with the NASA team algorithm [*Cavalieri et al.*, 1996, updated 2008]. Temporal resolution of the data is every two days, which we interpolate to daily values. The horizontal resolution is 25km, which we interpolate to the model resolution of about 50–200km. For an estimate of uncertainty in the sea-ice concentration observations, the reader may refer to *Tonboe and Nielsen* [2010], who arrive at an error estimate of around 10% on average. The assimilation methods we employ in this section are exactly the same as in the perfect-model study.

3.5.1 Ice concentration

From Fig. 3.3 we see that the annual-mean state of ice extent in ECHAM5/MPI-OM without data assimilation is reasonably close to the observed state. Of course, there are marked differences between the free model and the observations that are caused by natural variability – for instance, at the observed extreme extent minimum in 2007 the model actually has a temporary extent maximum.

Fig. 3.3 shows the northern-hemisphere yearly-mean ice extent from observations, from the AOGCM with no data assimilation, and from the AOGCM when concen-

tration observations are assimilated. Comparing Fig. 3.3 with Fig. 3.1, we see that the conclusions regarding the performance of the different methods are the same as in the perfect-model study: CMT fails as a sea-ice data assimilation approach in all quality criteria, CAT reproduces natural variability somewhat, but has a biased mean state, and PMT has both an acceptable mean state and reproduces natural variability satisfyingly. Considering the time-averaged measure for the assimilation error in sea-ice extent, δSIE, we see that only PMT is able to reduce δSIE below the no-assimilation case (see Table 3.1).

The seasonal cycle of sea-ice concentration error in the Arctic (Fig. 3.4) also resembles the result from the perfect-model study (Fig. 3.2). Note, however, that during summer the free model state now exhibits larger errors of up to 30%. Also, the errors for CMT and CAT are twice as large as in the perfect-model study, while the PMT shows only a slight increase in δSIE compared to the perfect model study.

In summary, we find that assimilating observations in ECHAM5/MPI-OM gives results for ice-extent and ice- concentration error that are very similar to the results of assimilating output of the same model. This indicates that the overall assimilation performance is dominated by deficiencies in the assimilation techniques, rather than model biases.

3.5.2 Ice thickness

There are currently only few large-scale ice thickness measurements available, and their reliability is not well known. For the purpose of comparing our simulated ice thickness with observations, we choose the ice thicknesses from ICESat laser altimeter measurements between 2005 and 2008 processed by *Yi and Zwally* [2010]. These data have complete coverage of mean sea-ice thickness data north of 65°N. Unfortunately, they are only available for a few discontinuous months, when the laser altimeter on the satellite was in operation. Due to the details of the measurement techniques, the thickness field from ICESat data can only be given as monthly means.

We compare the ice thickness averaged over the Arctic Ocean from ICESat measurements with the ice thickness from the PMT assimilation run. Uncertainty for the Arctic-Ocean average thickness from observations is estimated by *Kwok and*

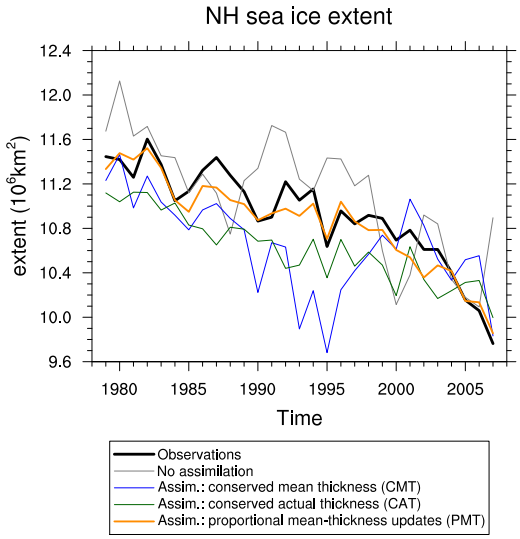

Figure 3.3: Yearly-mean ice extent in the northern hemisphere from observations (black), a model run with no assimilation (gray), and from the different assimilation methods (colors). The corresponding time-averaged global extent errors δSIE are given in Table 3.1.

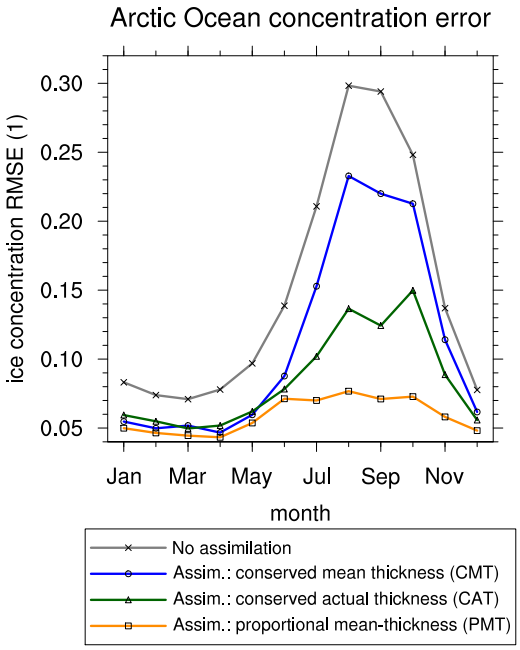

Figure 3.4: The average point-wise error in sea-ice concentration for the Arctic Ocean for each month of the year. All errors are obtained from the differences to the observed concentration fields.

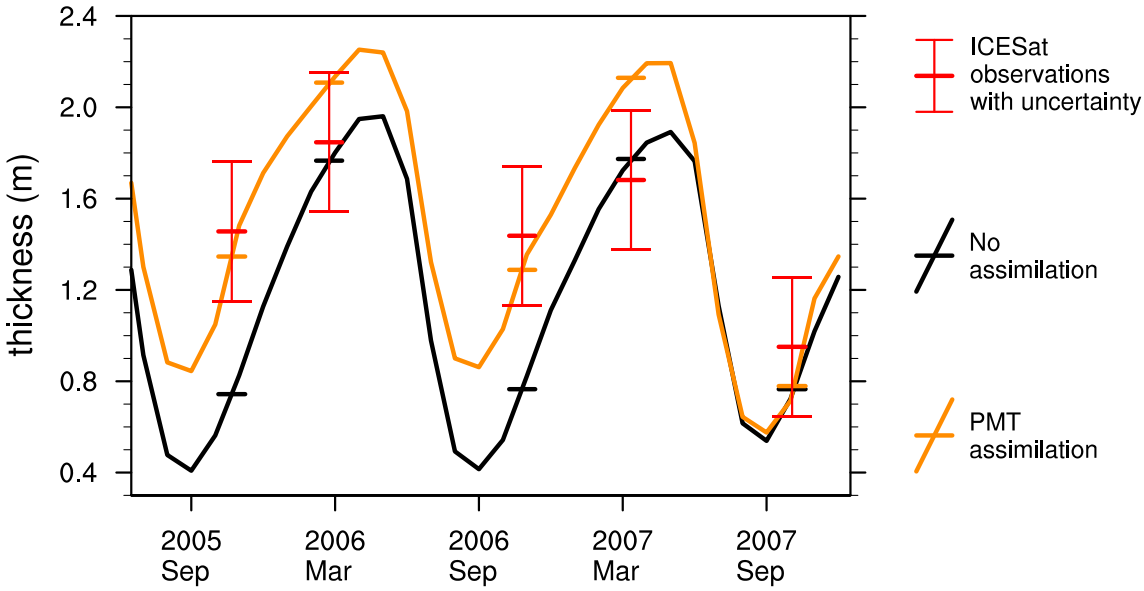

Figure 3.5: Comparison of modelled Arctic average ice thickness with ICESat observations. ICESat observations are only available as an average value for the time periods given by the red horizontal bars, and the model averages for the same time periods given by the orange and black horizontal bars.

Rothrock [2009] to be about 30 cm. Fig. 3.5 shows the average Arctic Ocean ice thickness from 2005 to 2007 in the model without assimilation and in the PMT assimilation run, in comparison with the ICESat observation. While the PMT assimilation improves the agreement between model and observations during early freeze-up in November 2005 and 2006, it causes the model to overestimate ice thickness later in the growth season (March 2006 and 2007). We feel that at present we cannot decide whether this is due to deficiencies in the model or deficiencies in the observations. However, the negative ice-volume anomaly in November 2007, which is very prominent in the observations, is captured well by the assimilation run.

We would like to point out that a thorough evaluation of modelled thickness with respect to observations is impossible at present, due to sparseness and uncertainty of sea-ice thickness observations. Therefore, we interpret the comparison of model thickness with ICESat thickness merely as a first indication that there is some skill in initializing sea-ice thickness anomalies in our experimental setup, and refer the reader to the perfect-model study for a robust quantification.

3.6 Physical aspects of understanding assimilation errors: how the ice model thermodynamics respond to analysis updates

We have seen in the previous sections that assimilating sea-ice data in an AOGCM does not necessarily lead to an improvement of the simulated sea-ice state. In particular, the assimilation of ice concentration can deteriorate the representation of ice thickness. In this section, we present lines of reasoning from a physical point of view that help to understand these assimilation errors.

After each analysis update, the model-calculated tendencies of prognostic variables are different than the tendencies before the analysis update. This can create undesired side-effects on unobserved variables and create feedback loops that impede skillful assimilation. We focus on sea-ice concentration as the observed variable, and mean sea-ice thickness as the most important variable that is not observed. We will see that the poor performance of CMT can be explained by analyzing how the model's *ice thermodynamics* respond to analysis updates. Some remarks on how the model's *ice advection* responds to analysis updates are given in Appendix 3.B.

3.6.1 A simple prognostic ice growth model

We discuss the equations for the sea-ice thermodynamics as they are implemented in ECHAM5/MPI-OM. After several simplification we arrive at a closed set of prognostic equations for the ice concentration C and mean ice thickness h_m. These equations constitute a simple ice-energy-balance model (IEBM), which we use to analyze the ice growth rate for different atmospheric forcing regimes and to study how the analysis updates affect the thermodynamics of the ice.

The first simplification we make is to neglect sea-ice advection. Since melting and freezing of ice are local processes, we can solve the prognostic equations for mean thickness (3.1) and concentration (3.2) for each point in space separately. The thermodynamic source terms for sea-ice mean thickness S_h (eq. (3.5)) and sea-ice concentration S_C (eq. (3.6)) are determined by a balance of atmospheric and oceanic heat fluxes at the sea-ice interfaces. An oceanic heat flux is established when sea

water warmer than the freezing temperature is brought into contact with the ice, while an atmospheric heat flux occurs at the interface between atmosphere and sea-ice or open water.

Since the dominant contribution to the sea-ice energy balance in the Arctic is typically the surface radiation [*Maykut and Untersteiner*, 1971; *Serreze et al.*, 2007b], we neglect oceanic and atmospheric turbulent surface heat fluxes as a first approximation and write

$$g_{w,i} = -\frac{1}{\rho L}\left((1-\alpha_{w,i})\mathrm{SW}_{\downarrow} + \mathrm{LW}_{\downarrow} - \sigma T_{w,i}^4\right), \tag{3.13}$$

where the subscript w denotes the open-water part of the surface, and i denotes the ice-covered part. The heat fluxes are converted to growth rates by multiplying with the negative ratio of sea-ice density ρ and the latent heat of fusion for water L. $\mathrm{SW}_{\downarrow}$ and $\mathrm{LW}_{\downarrow}$ are the downwelling shortwave and longwave radiation at the surface, and $\alpha_{w,i}$ is the albedo of open water or sea ice. In ECHAM5/MPI-OM, the surface temperature of open water in a partly ice-covered grid cell is always at a representative sea-water freezing temperature $T_w = -1.9\,^{\circ}\mathrm{C}$, and the ice surface temperature T_i is calculated from the balance of heat fluxes at the ice surface. We prescribe the atmospheric downwelling radiation as an external forcing and determine S_h and S_C as a function of ice state and forcing. Thereby, we can convert (3.1) and (3.2) into a closed set of two coupled ordinary differential equations, which are forced by the time-dependent downwelling radiation at the surface. Please refer to Appendix 3.A for details of the derivation.

3.6.2 Dependence of ice growth on atmospheric forcing

With (3.13) we have an explicit expression for the ice growth rate, and we can study how it depends on the atmospheric forcing. If we are able to identify forcing regimes that differ among each other in the way the sea-ice thermodynamics reacts to changes in concentration, we will have important information for assessing the effects of the data assimilation on the prognostic equations.

Fig. 3.6 shows the net growth rates derived from the IEBM for a typical sea-ice state of 1 m mean thickness and 70% concentration. We can identify three different

regimes, which are separated by the zero-growth contour over open water $g_w = 0$ and the zero-growth contour over ice $g_i = 0$. Importantly, the zero-growth contours are independent of the state of the ice and constitute the boundaries between three different forcing regimes.

In the *winter regime*, freezing occurs both over ice and over open water ($g_w > 0$, $g_i > 0$). The net ice growth rate g decreases for increasing concentration, because shortwave absorption is negligible and the longwave heat loss over open water dominates. For the *autumn/spring regime*, growth rates are generally small. Open-water growth rate is negative, whereas growth rate over ice is positive ($g_w < 0$, $g_i > 0$). In the *summer regime*, melting occurs both over open water and over ice ($g_w < 0$, $g_i < 0$). The net growth rate increases with increasing concentration, because the shortwave-albedo effect dominates over the longwave heat loss.

3.6.3 Dependence of ice growth on ice concentration

To quantify the dependence of growth rate on ice concentration, we select two representative forcing conditions: one for winter with $\mathrm{SW}_\downarrow = 0\,\mathrm{Wm}^{-2}$ and $\mathrm{LW}_\downarrow = 220\,\mathrm{Wm}^{-2}$ (marked with a blue dot in Fig. 3.6), and one for summer with $\mathrm{SW}_\downarrow = 160\,\mathrm{Wm}^{-2}$ and $\mathrm{LW}_\downarrow = 300\,\mathrm{Wm}^{-2}$ (marked with a red dot in Fig. 3.6). We calculate growth rates from the radiative budget of the IEBM described above, but there are two other contributions to the growth rate that we have neglected so far: the sensible and latent atmospheric heat flux, and the oceanic heat flux. Capturing these effects goes beyond the scope of the IEBM, but we can diagnose them from daily-mean fields of a long AOGCM run.

Fig. 3.7 shows a synthesis of ice growth rates derived from the IEBM, and the occurrence of ice growth rates as diagnosed from the AOGCM. During summer (Fig. 3.7a–c), the single curve obtained from the IEBM approximates the occurrence of growth rates diagnosed from the AOGCM quite well, implying that oceanic contributions to ice melt as well as turbulent atmospheric heat fluxes are negligible. This is readily explained since the near-surface atmosphere is close to the melting point, so that turbulent heat fluxes at the surface are small. At the same time, the ocean surface is warmed and becomes fresher, so that it gains buoyancy, and therefore convection is inhibited. Both in the IEBM and in the AOGCM, we observe

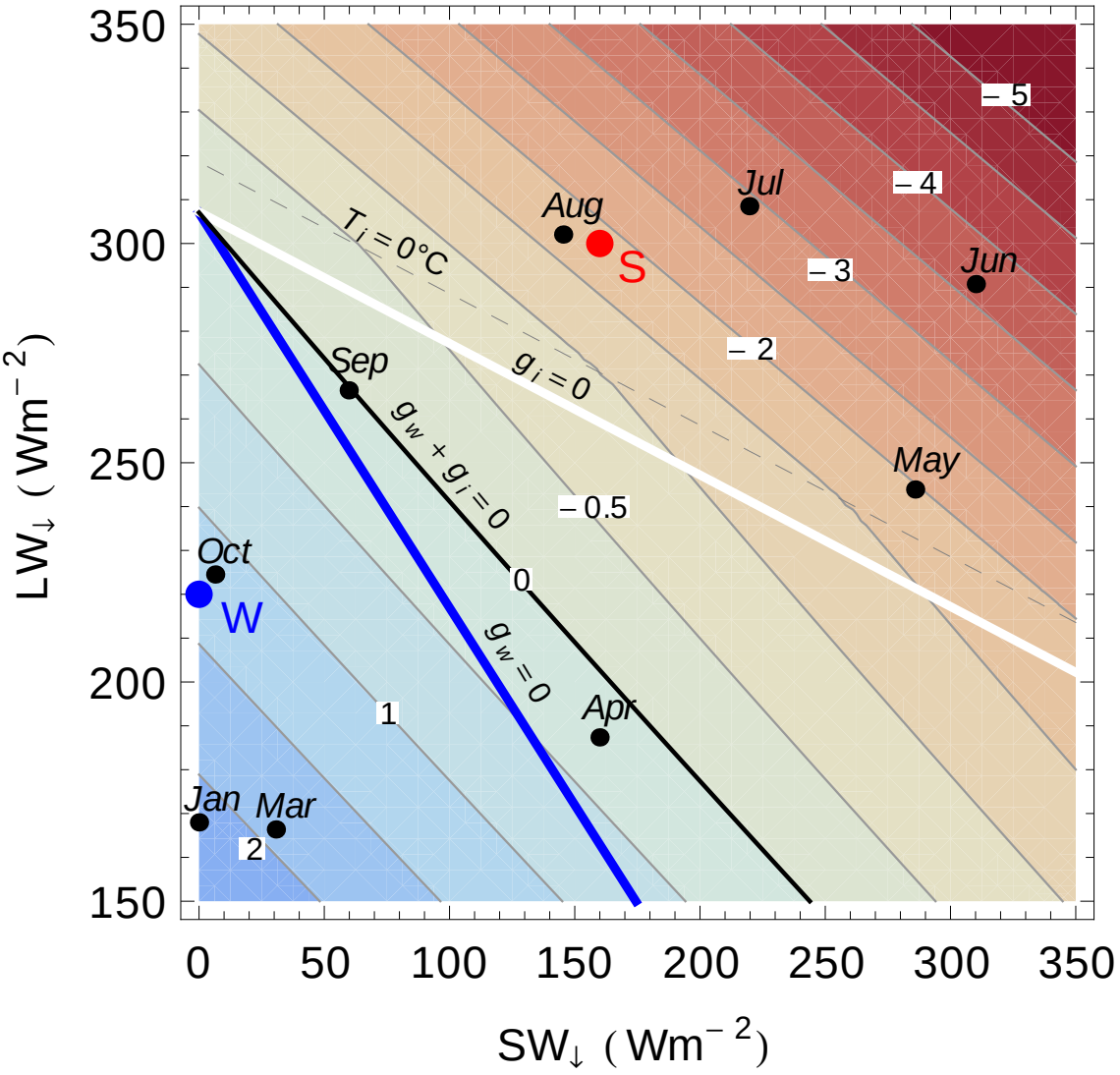

Figure 3.6: Contour plot of ice growth rates in cm/day for mean ice thickness $h_m = 1\,\mathrm{m}$ and ice concentration $C = 0.7$. On the x-axis is the downwelling shortwave radiation, on the y-axis the downwelling longwave radiation. The black dots correspond to the typical monthly-mean forcing in the Arctic according to *Maykut and Untersteiner* [1971]. The blue and white lines mark the zero-crossing of the growth rates for open water and over ice, which are independent of the state of the ice. The thick black line is the zero-crossing of net growth rate, and depends on the state of the ice. At the dashed gray line, the ice surface temperature is at the melting point of 0°C. The larger blue and red dots, labelled "W" and "S", mark typical winter and summer conditions, for which the conditional probability distributions of growth rate in Fig. 3.7 are calculated.

a strong dependence of net ice growth rate on concentration: for the chosen atmospheric summer forcing, ice melts at the rate of 1cm/day for 100% ice concentration, whereas it melts at a rate of more than 4cm/day for very low ice concentration.

In winter, the IEBM is not a good approximation to the sea-ice thermodynamics in the AOGCM. As Fig. 3.7d shows, the curve determined from the radiative budget in the IEBM is actually at the lower boundary of the probability distribution of atmospheric growth rates. For open-water conditions, the IEBM predicts an atmospheric growth rate of 2cm/day, whereas the most frequent value in the AOGCM is 5cm/day, and even values of 8cm/day occur quite often. The missing contribution comes from the turbulent atmospheric heat flux, which can be very large over open water during winter. Only if the near-surface atmosphere stratification is very stable and near-surface winds are very weak, does the turbulent heat flux become so small that the AOGCM exhibits the dependence derived from the radiation budget in the IEBM.

Additionally, in winter the oceanic contribution to ice growth becomes large (Fig. 3.7e). The oceanic contribution can be due to horizontal advection of warm water under the ice, upwelling of warm water through Ekman suction, or entrainment of warm water when the surface mixed layer deepens. The model shows high ocean–ice heat fluxes predominantly close to the ice edge. The diagnostic we use does not differentiate between the processes, but we believe that the major contribution comes from entrainment of warm water from below during the deepening of the surface mixed layer. As *Lemke* [1987] pointed out, especially at the onset of freezing the convection can be vigorous enough to explain the magnitude of the ocean–ice heat flux that we see in the model.

For low ice concentration in winter, the ocean–ice heat flux strongly inhibits ice growth. The most frequent value of the heat flux, expressed as an equivalent melt rate, is 4cm/day, and even much larger values are possible (Fig. 3.7e). This compensates the large atmosphere–ice heat flux (Fig. 3.7d), so that the net growth rate in winter depends only weakly on the concentration (Fig. 3.7f). Nevertheless, since sea ice is closely coupled to the surface mixed layer below, it is the heat content of the coupled system sea-ice–surface-mixed layer that is essential for the evolution of the ice. This heat content is determined by the atmospheric heat flux, and we therefore argue that the atmospheric growth rate in winter is more important than the net

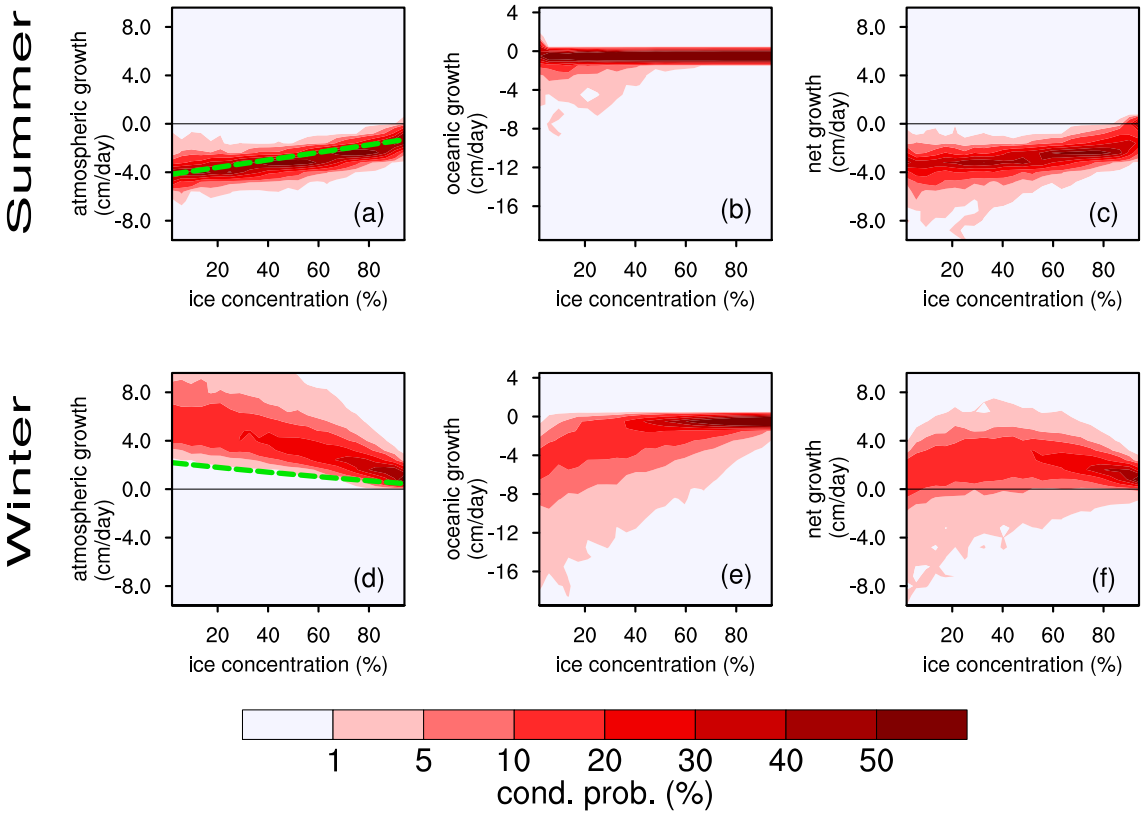

Figure 3.7: Conditional probability densities with which heat fluxes contributing to sea-ice growth occur for a given sea-ice concentration. The occurrence probabilities are diagnosed from a long run of ECHAM5/MPI-OM for representative summer (a–c) and winter (d–f) conditions. Heat fluxes are given as equivalent ice growth rates (1cm/day $\widehat{=} 35\,\mathrm{Wm}^{-2}$). Heat fluxes shown in (a)+(d) are between the ice and the atmosphere, and in (b)+(e) between the ice and the ocean. (c)+(f) show the net growth rates of the sea-ice, which are equivalent to the sum of atmospheric and oceanic heat flux into the ice. The dashed green line is the dependence found in the simple radiative ice-energy balance model.

growth rate. The heat that goes from the mixed layer into the ice and inhibits ice growth cools the sea water, so that ice formation is affected at a later time.

3.6.4 Implications for sea-ice data assimilation

The dependence of ice growth rate on the concentration, as detailed in the previous section, has important implications for sea-ice data assimilation. In summer, the melt rate decreases strongly with increasing concentration. A positive analysis update of concentration will therefore lead to less melt. Through the dependence of the concentration rate of change on the thickness rate of change (eq. (3.6)), this will lead to still higher values of concentration, so that a positive feedback on the analysis updates is established. In winter, the (atmospheric) growth rate strongly decreases with increasing concentration. A positive analysis update of concentration will lead to less growth, and through (3.6) a negative feedback on the analysis updates is established.

We use the IEBM from the previous section to quantify this effect and illustrate the difference between the CMT and PMT assimilation techniques. With a continuous version of the relaxation terms discussed in Sec. 3.3, the IEBM equations read

$$\frac{\mathrm{d}C}{\mathrm{d}t} = S_C = \Theta(g_w)\frac{g_w}{h_0}(1-C) + \Theta(-S_h)\frac{C}{2h_m}S_h + T_R^{-1}(C-C^o) \tag{3.14}$$

$$\frac{\mathrm{d}h}{\mathrm{d}t} = S_h = g_i C + (1-C)g_w + f(T_R^{-1}(C-C^o)). \tag{3.15}$$

The last term on the right-hand side of (3.14) assimilates (nudges) the idealized concentration observations C^o into the model with a relaxation time T_R of 10 days. The last term on the right-hand side of (3.15) represents the different forms of the functional dependence between the mean-thickness analysis update and the concentration update that we investigate (CMT, CAT or PMT).

As an idealized test case, we prescribe constant forcing for one month and compare the evolution of C and h_m with and without the assimilation terms. We choose the same winter and summer forcing as in the last section and focus on those combinations of modeled and observed ice conditions that are problematic for the data assimilation.

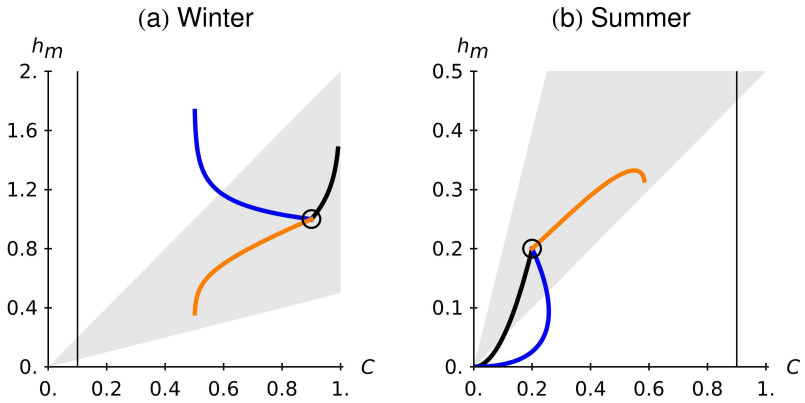

Figure 3.8: Trajectories of the sea-ice state in the ice energy balance model (IEBM) with and without assimilation for one month of constant winter conditions (a), and summer conditions (b). The black trajectory is the IEBM without assimilation, the blue trajectory is with CMT assimilation, and the orange trajectory is with PMT assimilation. The target ice concentration is marked by a thin vertical line, and trajectories start with the same initial conditions marked by a circle. The nudging parameters are as in the AOGCM experiments. Mean ice thickness for a given concentration in the AOGCM is typically within the gray shaded area.

For the winter test case (Fig. 3.8a), the trajectories start from high concentration and 1 m mean thickness. Since the forcing implies freezing conditions, both concentration and mean thickness increase when there is no nudging. When we nudge the model to low ice concentration, the concentration initially decreases, but after one month the model and nudging tendencies for concentration almost compensate, and concentration stays constant at an intermediate level. For the mean ice thickness, we observe contrasting behavior for PMT and CMT. The CMT trajectory still goes to higher thickness, and even outgrows the free trajectory. It therefore enters a state of low sea-ice concentration and high mean ice thickness, which is rather unphysical and not typically seen in the AOGCM. On the other hand, the PMT trajectory decreases mean ice thickness, and hence stays within the region of typical ice states.

For the summer test case (Fig. 3.8b), we let the trajectories start at low concentration and 0.2 m mean thickness. The trajectory without the relaxation term goes to an ice-free state within a month. When we nudge towards high concentration, the behavior of PMT and CMT is again very different. The CMT trajectory loses ice volume; since for constant forcing the concentration loss is higher for thinner ice

(see eq. (3.6)), concentration only initially increases, but soon the thermodynamic tendency outweighs the nudging tendency. Consequently, the CMT trajectory also becomes ice-free within a month, even though the data assimilation aims at increasing the ice concentration. On the other hand, the PMT trajectory gains ice volume, and stays inside the region of typical ice states.

In the coupled model, an indication for the problematic behavior of the CMT method is found in the winter-time Barents Sea (Fig. 3.9). During the 1990s, the Barents Sea was mainly ice-free during winter, as derived from the satellite observations, whereas the model without assimilation is biased towards ice-covered conditions. When assimilating the observed ice concentration, the ice concentration in this area decreases, but the decreased concentration leads to enhanced thermodynamic ice growth rates. As a result, there is unrealistically high ice volume in conjunction with a reduced ice concentration if the CMT method is employed. Only when we apply PMT, this effect is averted, as the nudging updates of ice volume compensate the excessive thermodynamic growth rates. Fig. 3.9 shows the comparison of ice concentration and mean thickness for both methods.

3.7 Statistical aspects of understanding assimilation errors: model error covariances and weight matrices

We now take a different view on assimilation errors: instead of examining the sea-ice prognostic equations and how analysis updates affect them, we examine the covariance structure of thickness and concentration errors in the AOGCM. There is a well-established theory that connects these so-called model background errors with the optimal analysis update (see, for instance, *Bouttier and Courtier* [1999] or *Kalnay* [2003]). The analysis updates we apply are not optimal, but derived from the simple nudging approach. Nevertheless, we can map our different choices for the analysis update to different model background errors that are implied under the assumption of optimality. If then the implied model background errors are clearly unrealistic, we can argue that the assimilation method is prone to fail, since it is very

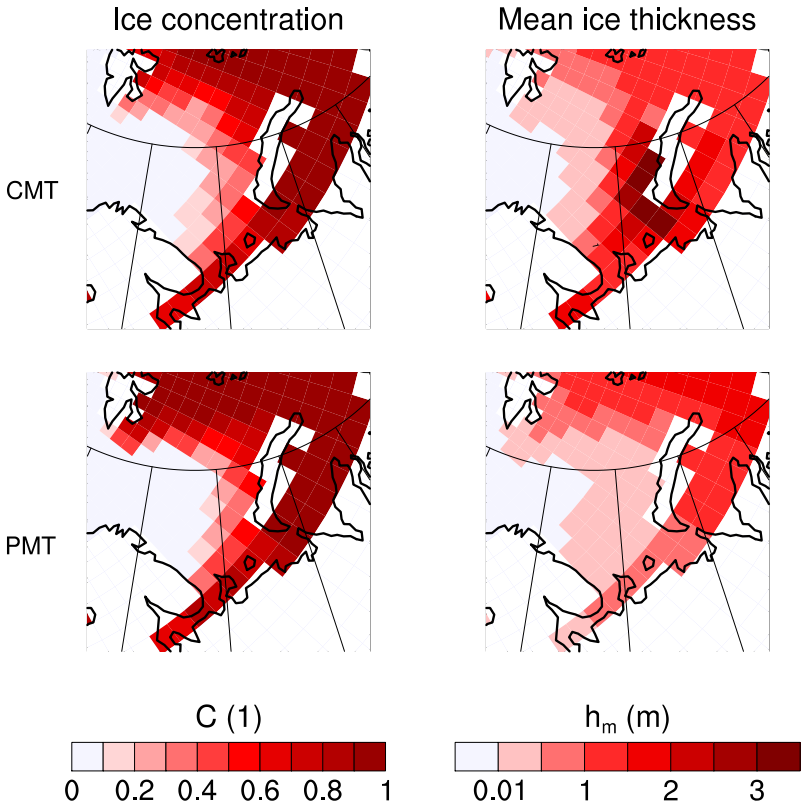

Figure 3.9: Average March conditions 1990–1999 when assimilating observed sea-ice concentration in the AOGCM with the CMT method (top) and the PMT method (bottom). Ice concentration is similar in CMT and PMT, and quite close to observations (left). However, mean ice thickness (right) is much too high for CMT, and realistic for PMT.

far from being optimal. We use a notation closely following *Bouttier and Courtier* [1999] and briefly introduce the basic terminology in the following paragraphs, before we apply the general terms to our setup from eq. (3.19) on.

The state of a model that has v variables and p grid points is encoded in the *state vector* $\boldsymbol{x}$, a column vector with $p \cdot v$ entries. To obtain the analysis $\boldsymbol{x}_a$, i.e. our estimate of the true state $\boldsymbol{x}_t$, the model background $\boldsymbol{x}_b$ is updated with a term that depends on the departure of the model state from the observations $\boldsymbol{y}$:

$$\boldsymbol{x}_a = \boldsymbol{x}_b + \boldsymbol{K}(\boldsymbol{y} - \boldsymbol{H}\boldsymbol{x}_b). \tag{3.16}$$

The *observation operator* $\boldsymbol{H}$ maps the o observations to the vp-dimensional state vector $\boldsymbol{x}$ and therefore is a matrix with dimensions $o \times vp$. The $(vp \times o)$-dimensional matrix $\boldsymbol{K}$ determines how discrepancies between observations and the model state translate to analysis updates. It is called the gain, or *weight matrix*. If the weight matrix is chosen according to

$$\boldsymbol{K}^{\text{opt}} = \boldsymbol{B}\boldsymbol{H}^T(\boldsymbol{H}\boldsymbol{B}\boldsymbol{H}^T + \boldsymbol{R})^{-1}, \tag{3.17}$$

then the analysis (3.16) is the best linear unbiased estimator of the true state [*Bouttier and Courtier*, 1999].

The optimal weight matrix $\boldsymbol{K}^{\text{opt}}$ is related to the covariance matrices of background and observation errors $\boldsymbol{B}$ and $\boldsymbol{R}$, defined by

$$\boldsymbol{B} := \langle(\boldsymbol{\epsilon}_b - \bar{\boldsymbol{\epsilon}_b})(\boldsymbol{\epsilon}_b - \bar{\boldsymbol{\epsilon}_b})^T\rangle \qquad \boldsymbol{R} := \langle(\boldsymbol{\epsilon}_o - \bar{\boldsymbol{\epsilon}_o})(\boldsymbol{\epsilon}_o - \bar{\boldsymbol{\epsilon}_o})^T\rangle. \tag{3.18}$$

The model background error $\boldsymbol{\epsilon}_b := \boldsymbol{x}_b - \boldsymbol{x}_t$ describes the discrepancy between the modelled and the true state *just before* an analysis update. Therefore, ϵ_b depends not only on the error of the model itself, but also on the applied analysis updates and the time interval between them. The observation error $\boldsymbol{\epsilon}_o := \boldsymbol{y} - \boldsymbol{H}\boldsymbol{x}_t$ expresses that the reported value of an observation is not a perfect image of reality, but is distorted due to instrumental and discretization errors. $\boldsymbol{B}$ has dimensions $pv \times pv$, and $\boldsymbol{R}$ has dimensions $o \times o$.

After introducing the general terminology, we now apply it to our setup. Because the simplicity of the setup allows for several algebraic simplifications, we can de-

rive concise expressions that are useful for understanding the interplay between ice thickness and ice concentration errors. We order the state vector $\boldsymbol{x}$ so that it starts with the entries for ice concentration C and ice mean thickness h, followed by all other model variables:

$$\boldsymbol{x} := \Big(C_1, \quad \ldots, \quad C_p, \quad h_1, \quad \ldots, \quad h_p, \quad \ldots\Big)^T. \tag{3.19}$$

Sea-ice concentration is the only variable observed, and we are not interested in issues related to the interpolation from observation points to model points. Thus, we can assume a very simple form for the observation operator:

$$\boldsymbol{H} = \Big(\boldsymbol{I} \quad \boldsymbol{0} \quad \ldots\Big), \tag{3.20}$$

with $\boldsymbol{I}$ denoting the $p \times p$ identity matrix and $\boldsymbol{0}$ denoting the $p \times p$ zero matrix. Furthermore, the observation error covariance matrix $\boldsymbol{R}$ reduces to the $p \times p$ matrix $\boldsymbol{R}_{CC}$.

We partition the model error covariance matrix and the weight matrix into $p \times p$ submatrices that respectively describe the covariance between each two variables in the model and the gains for each model variable resulting from the concentration observations:

$$\boldsymbol{B} = \begin{pmatrix} \boldsymbol{B}_{CC} & \boldsymbol{B}_{hC} & \ldots \\ \boldsymbol{B}_{Ch} & \boldsymbol{B}_{hh} & \ldots \\ \vdots & \vdots & \ddots \end{pmatrix} \quad \boldsymbol{K} = \begin{pmatrix} \boldsymbol{K}_{CC} \\ \boldsymbol{K}_{Ch} \\ \vdots \end{pmatrix} \tag{3.21}$$

Using equations (3.19)–(3.21), the analysis update (3.16) can be written as

$$\begin{pmatrix} \boldsymbol{C}_a \\ \boldsymbol{h}_a \\ \vdots \end{pmatrix} = \begin{pmatrix} \boldsymbol{C}_b \\ \boldsymbol{h}_b \\ \vdots \end{pmatrix} + \begin{pmatrix} \boldsymbol{K}_{CC} \\ \boldsymbol{K}_{Ch} \\ \vdots \end{pmatrix} (\boldsymbol{C}_o - \boldsymbol{C}_b), \tag{3.22}$$

and the optimal weight matrix (3.17) reduces to a form that shows how the concen-

tration and thickness background errors enter the optimal weight matrix:

$$\boldsymbol{K}^{\text{opt}} = \begin{pmatrix} \boldsymbol{B}_{CC} \\ \boldsymbol{B}_{Ch} \\ \vdots \end{pmatrix} \left(\boldsymbol{B}_{CC} + \boldsymbol{R}_{CC} \right)^{-1}. \tag{3.23}$$

Eq. (3.23) tells us how to obtain the optimal analysis update when we already know the correct statistics of the background and observation errors. Determining these error statistics is a difficult task within the data assimilation framework. Here, we are only interested in conceptual statements that can be derived from the error covariances, and so we estimate them using simplifying assumptions. We assume that the observation error covariance $\boldsymbol{R}_{CC}$ is spatially uncorrelated and corresponds to a constant uncertainty of 10%. This value is a reasonable average error for concentration observation according to *Tonboe and Nielsen* [2010]. We estimate the background error covariances $\boldsymbol{B}_{CC}$ and $\boldsymbol{B}_{Ch}$ from the daily differences between concentration and thickness of two long independent model runs. These background errors apply when the time interval between analysis updates is very large. For shorter time intervals between the analysis updates (one day for our setup), the absolute magnitude of the covariances is smaller, but we expect their *spatial structure* to be the same. For instance, in the central Arctic the sea-ice concentration is usually high, and thus we expect a low concentration background error variance, whereas in areas that experience a pronounced seasonal cycle of both thickness and concentration we expect substantial background error covariance.

For the analysis updates of mean thickness, eq. 3.23 defines the optimal weight matrix

$$\boldsymbol{K}_{Ch}^{\text{opt}} = \boldsymbol{B}_{Ch} \left(\boldsymbol{B}_{CC} + \boldsymbol{R}_{CC} \right)^{-1}. \tag{3.24}$$

In our setup, we use weight matrices derived not from the optimality condition, but from an ad hoc nudging approach. Nevertheless, we can ask the following question: "Suppose the weight matrix $\boldsymbol{K}_{Ch}$ we use is optimal, and we know the background error covariance for concentration $\boldsymbol{B}_{CC}$, what would be the corresponding background error covariance between concentration and thickness $\boldsymbol{B}_{Ch}$?" If the background covariance that is implied by a prescribed nudging weight matrix $\boldsymbol{K}_{Ch}$ looks unre-

alistic, we can conclude that the weight matrix is far from being optimal and reject an assimilation scheme that uses this weight matrix as being inconsistent.

For CMT, we do not update mean thickness at all, and so

$$\boldsymbol{K}_{Ch}^{\mathrm{CMT}} = \mathbf{0} \quad \overset{\text{Optimality}}{\Longleftrightarrow} \quad \boldsymbol{B}_{Ch}^{\mathrm{CMT}} = \mathbf{0}. \tag{3.25}$$

For CAT, we see from eq. (3.10) that nudging weights vary in time and space, depending on the background actual thickness. We derive a time-averaged analysis update by diagnosing a diagonal matrix $\boldsymbol{h}_t$ that contains the time average of actual ice thickness at each grid point over a long model run on the diagonal. With this, the average weight matrix and implied background error covariance are

$$\boldsymbol{K}_{Ch}^{\mathrm{CAT}} = K_N \boldsymbol{h}_t \quad \overset{\text{Optimality}}{\Longleftrightarrow} \quad \boldsymbol{B}_{Ch}^{\mathrm{CAT}} = K_N \boldsymbol{h}_t (\boldsymbol{B}_{CC} + \boldsymbol{R}_{CC}). \tag{3.26}$$

Finally, for PMT the weights are constant. Together with their implied background error covariance they are given by

$$\boldsymbol{K}_{Ch}^{\mathrm{PMT}} = K_N h^* \boldsymbol{I} \quad \overset{\text{Optimality}}{\Longleftrightarrow} \quad \boldsymbol{B}_{Ch}^{\mathrm{PMT}} = K_N h^* (\boldsymbol{B}_{CC} + \boldsymbol{R}_{CC}). \tag{3.27}$$

The different background error covariances are compared in Fig. 3.10 by showing maps of their scaled diagonal elements. The absolute value of the covariances are not important, since they depend on the time interval between the analysis updates. However, the spatial distribution of high and low covariances has a large influence on the assimilation performance, as they determine the relative strengths of the optimal weights.

From Fig. 3.10b we see that background error covariances diagnosed from free model runs are low in the perennial ice zone of the central Arctic, since there the concentration is always high, and low at the southern edge of the seasonal ice zone, since there the mean ice thickness is always low. In between, there is a region where mean ice thickness and ice concentration co-vary strongly.

The CMT analysis updates imply a covariance structure that is unrealistic: it is zero everywhere. This implies a perfect representation of thickness forecasts in the model, which is a bad assumption, as we have seen in Section 3.6. Therefore, the CMT weight matrix is far from being optimal. Already from this simple anal-

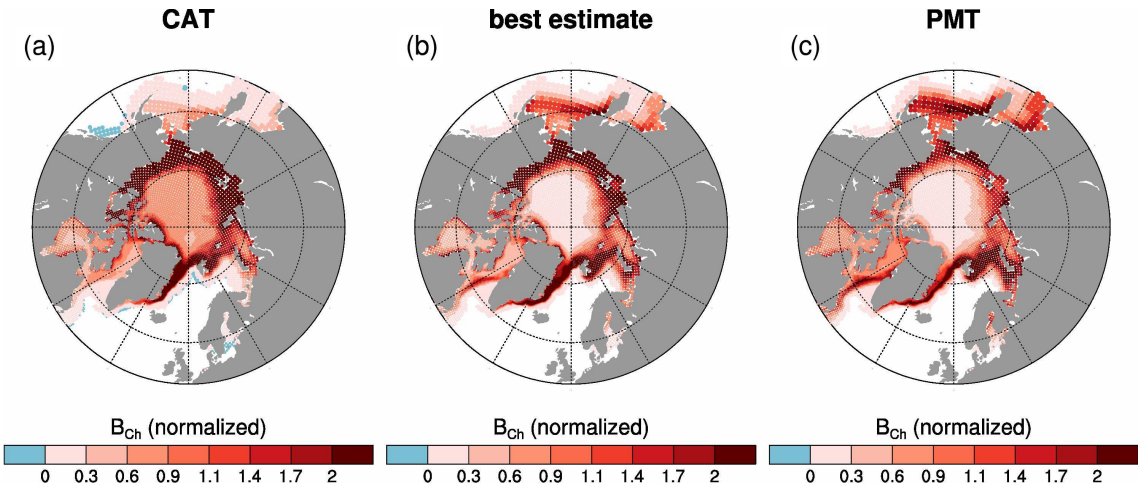

Figure 3.10: Scaled diagonal elements of the background error covariance matrices; (a) implied when analysis updates conserve actual thickness, (b) best estimate from a long free model run, and (c) implied by proportional mean-thickness analysis updates. The background error covariance implied by analysis updates that conserve mean thickness is zero everywhere. For an interpretation of the figure see main text.

ysis of background error covariance one could have expected the poor assimilation performance seen in Section 3.4 and 3.5.

The CAT updates imply a covariance structure that resembles our best guess reasonably well, so that one would expect a useful assimilation performance (Fig. 3.10a). However, some discrepancies stand out: The implied thickness-concentration covariance is too high in the central Arctic, indicating that the weights for updating mean thickness are too large there. This is potentially problematic, because large analysis updates in areas of thick ice create problems related to ice advection (see Appendix 3.B). On the other hand, the implied covariance is too low in the Bering Sea, the Labrador Sea, and the Barents Sea. One would expect the method to have difficulties assimilating observations there, since the analysis weights are too small.

Finally, the PMT updates shown in Fig. 3.10c imply a concentration-thickness covariance structure that is very close to our best guest. There is a tendency to underestimate covariance in the Arctic shelf seas, and to overestimate it in the Hudson and Baffin Bays, but overall there is good agreement.

We conclude that the comparison of the background error covariances implied by the chosen nudging weight matrices $\boldsymbol{K}_{Ch}$ corroborates the experimentally found

differences between the assimilation performance of the CMT, CAT, and PMT methods. Moreover, we think that the examination of implied background error covariance is a useful guideline for designing weight matrices: only if the implied background error covariance looks plausible, we can expect a good performance of the assimilation method.

3.8 Summary and conclusion

This study is one of only few to deal with sea-ice data assimilation in a global climate model. We restrict ourselves to observations of northern-hemisphere sea-ice concentration, and employ a simple Newtonian relaxation approach. Analysis updates for the mean sea-ice thickness in a grid cell are prescribed as a function of the concentration analysis updates.

We assess the assimilation performance for three different approaches for the mean thickness analysis updates. The first approach keeps the mean thickness constant during the analysis update (CMT). The second approach keeps the actual ice thickness constant (CAT). CMT and CAT have been suggested and used before in sea-ice data assimilation [*Dulière and Fichefet*, 2007], but we find that in our assimilation setup they do not give satisfying results. Therefore, we introduce a third approach, which prescribes a fixed proportionality between concentration updates and mean thickness updates (PMT).

We find that PMT has much lower assimilation errors than the other two methods. For synthetic observation data derived from output of the same model, PMT reduces the error in northern-hemisphere sea-ice extent by a factor of 6 and the error in northern-hemisphere sea-ice volume by a factor of 2, when compared to a model run without assimilation. Similar values are obtained for the gridpoint-wise error in ice concentration and mean ice thickness in the Arctic Ocean. For the assimilation of observed sea-ice concentration between 1979 and 2007, the extent error is reduced by a factor of 4, while a comparison with the few direct observations of sea-ice volume that are available suggests that at least the volume anomaly in 2007 is well captured.

The simplicity of the assimilation scheme allows us to investigate the potential

sources of assimilation errors with conceptual tools. Using a simple model for the local ice energy balance, and histograms of heat fluxes in the AOGCM, we quantify how sensitively the ice growth rate depends on ice concentration. Because of this sensitivity, the assimilated change in sea-ice concentration often causes an unrealistic change in mean ice thickness. We conclude that this causes the unacceptable assimilation errors in the CMT approach, where no adjustments to the mean thickness are made during the analysis update. We argue that ice concentration assimilation that aims at conserving mean ice thickness during the analysis update is therefore not feasible in an AOGCM, although it may work in ice–ocean models that are forced by atmospheric surface conditions [*Lindsay and Zhang*, 2006; *Stark et al.*, 2008]. Instead, in an AOGCM the assimilation method should update mean ice thickness in accordance with the model background error covariance between concentration and mean thickness.

The spatial structure of the background error covariance between concentration and thickness – as implied by the nudging weight matrix – is unrealistic for CMT, reasonable but deficient for CAT, and realistic for PMT. This finding gives an independent explanation of the differences in assimilation performance we find experimentally.

We conclude that skillful sea-ice initialization in an AOGCM from ice-concentration data is possible even with a simple Newtonian relaxation scheme if we choose an appropriate functional relationship between concentration and mean-thickness analysis updates.

Appendix 3.A A simple radiative sea-ice energy balance model

We start from the full model equations for mean thickness (3.1), concentration (3.2), and the thermodynamic source terms (3.5) and (3.6). Neglecting advection, the system reduces to two coupled ordinary differential equations:

$$\frac{\mathrm{d}h_m}{\mathrm{d}t} = g_i C + (1-C) g_w \tag{3.28}$$

$$\frac{\mathrm{d}C}{\mathrm{d}t} = \Theta(g_w)\frac{g_w}{h_0}(1-C) + \Theta(-S_h)\frac{C}{2h_m}S_h. \tag{3.29}$$

An explanation of the symbols is given in the main text.

To obtain a closed system of equations, we need to determine how the growth rates g_w and g_i depend on the forcing, i.e. downwelling longwave and shortwave radiation at the surface, and the state of the ice, i.e. concentration and mean thickness. These growth rates are directly proportional to the heat fluxes via

$$g_{w,i} = -\frac{\rho}{L} q_{w,i}, \tag{3.30}$$

where ρ is the density of sea ice, and L is the latent heat of fusion for water.

As motivated in the main text, we neglect turbulent atmospheric surface heat fluxes and oceanic heat flux to the bottom of the ice, and write the net heat fluxes over open-water q_w and over ice surface q_i as

$$q_{w,i} = (1-\alpha_{w,i})\mathrm{SW}_{\downarrow} + \mathrm{LW}_{\downarrow} - \sigma T_{w,i}^4. \tag{3.31}$$

The heat flux over open water in a partly ice-covered grid cell is easy to determine: the temperature of that open water is at the freezing point, so that the the upwelling longwave radiation is constant. The heat flux over ice is more difficult, since it depends on the ice surface temperature T_i. The ice surface temperature has to be determined from the balance of the heat flux at the ice surface q_i with the conductive heat flux through the ice q_c and a residual heat flux q_r that goes into surface melt:

$$q_i = q_c + q_r. \tag{3.32}$$

The conductive heat flux through the ice is assumed to be proportional to the difference between the temperature at the top of the ice T_i and the temperature at the bottom, which is always at the freezing temperature T_f. This is the so-called 0-layer model for ice growth suggested by *Semtner* [1976]. The proportionality constant is the heat conductivity of ice k divided by the actual ice thickness $h_t = h_m/C$. The conductive heat flux as a function of ice surface temperature then is

$$q_c(T_i) = \frac{kC}{h_m}\left(T_i - T_f\right). \tag{3.33}$$

In our model, sea ice is assumed to melt at the freshwater melting temperature $T_m = 0^\circ\,\mathrm{C}$ at the top. When $T_i < T_m$, there is no surface melt, $q_r = 0$, and T_i can be derived from $q_i = q_c$. With a linearization of the black-body radiation around T_m, we can solve for T_i and obtain

$$T_i = \frac{T_f kC/h_m + (1-\alpha_i)\mathrm{SW}_\downarrow + \mathrm{LW}_\downarrow + 3\sigma T_m^4}{kC/h_m + 4\sigma T_m^3}. \tag{3.34}$$

The ice surface temperature cannot get larger than T_m in the model, because for $T_i = T_m$ the residual heat flux becomes larger than zero, $q_r > 0$, and melts ice at the surface:

$$\begin{aligned} q_r\big|_{T_i=T_m} &= q_i(T_m) - q_c(T_m) \\ &= (1-\alpha_i)\mathrm{SW}_\downarrow + \mathrm{LW}_\downarrow - \sigma T_m^4 - \frac{kC}{h_m}\left(T_m - T_f\right). \end{aligned} \tag{3.35}$$

Inserting (3.33) and (3.35) into (3.32), we can write the net heat flux into the ice-covered part of the cell in a compact form:

$$q_i = \frac{kC}{h_m}\left(T_i - T_f\right) + \delta(T_i - T_m)\left(-\frac{kC}{h_m}\left(T_m - T_f\right) + (1-\alpha_i)\mathrm{SW}_\downarrow + \mathrm{LW}_\downarrow - \sigma T_m^4\right) \tag{3.36}$$

With this, we have obtained a closed set of equations for the mean ice thickness h_m and the ice concentration C with the downwelling shortwave and longwave radiation at the surface as an external forcing.

Appendix 3.B Advective response of sea ice to analysis updates

We briefly discuss the contribution of internal forces to the sea-ice dynamics, which can lead to problems for the assimilation of ice concentration and are especially relevant for the CAT scheme. For thick ice with high concentration, the internal forces are very large and dominate the momentum balance (3.3), as a scale analysis reveals.

We consider ice dynamics on a spatial scale of about 100 km ($L = 10^5$ m). Empirical velocities are $v_i = 10^{-1}$ m/s for the ice, $v_o = 10^0$ m/s for the ocean, and $v_a = 10^1$ m/s for the atmosphere. The magnitude of the Coriolis parameter f is 10^{-4}, for ice density ρ_i it is 10^3, and the sea-surface elevation ζ is assumed to be of order 10^{-1} m.

The magnitude of atmosphere and ocean drag are calculated according to

$$\tau_{a/o} = \rho_w C_w (v_{a/o} - v_i)^2,$$

where the drag coefficient C_w is of order 10^{-3}.

For the internal ice forces, we restrict ourselves to consider the internal pressure P, which describes the resistance of the ice pack against compression:

$$\boldsymbol{\sigma}_{ij} = -P\boldsymbol{\delta}_{ij}/2 \quad (+ \text{ shear stresses}).$$

The equation of state for the internal pressure chosen by *Hibler III* [1979], and adopted in ECHAM5/MPI-OM, is

$$P = P^* h_m \, e^{-\alpha(1-C)},$$

with the empirical constants $P^* = 5000$ Nm^{-2} and $\alpha = 20$.

Inserting the scales set above, and considering mean ice thicknesses that varies between 1 and 10 m and ice concentrations that varies between 50 and 100 %, the

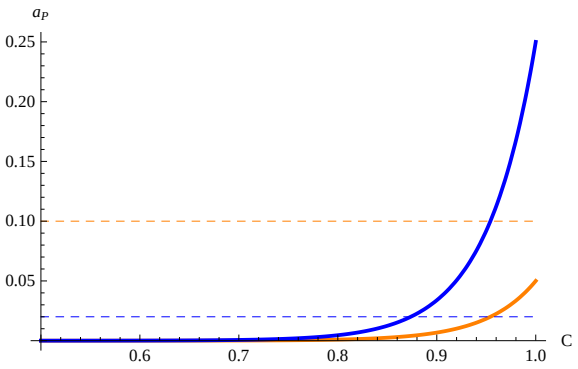

Figure 3.11: Ice acceleration due to internal pressure depending on ice concentration for the Hibler model. Thick orange for 1m average thickness, thick blue for 5m. The thin dashed lines give the strength of the atmospheric drag, which is next largest term in the momentum balance assuming a wind speed of 10m/s.

scale analysis of (3.3) gives

$$\begin{array}{ccccccc} \partial_t \mathbf{v} = & -f(\mathbf{k}\times\mathbf{v}) & -g\nabla\zeta & +\dfrac{\boldsymbol{\tau_a}}{\rho_i h_m} & +\dfrac{\boldsymbol{\tau_o}}{\rho_i h_m} & +\nabla\cdot\boldsymbol{\sigma}_{ij} \\ & 10^{-5} & 10^{-5} & 10^{-2\ldots-3} & 10^{-4\ldots-3} & 10^{-6\ldots-1} \end{array}$$

We see that the magnitude of the internal forces is extremely variable. For low ice concentrations, internal forces are negligible compared to other contributions, whereas for thick ice with high concentration they clearly dominate all other contributions. The reason for this is of course the exponential dependence of ice strength P on ice concentration.

Fig. 3.11 illustrates how the acceleration from internal pressure changes with concentration, and compares it to the atmospheric drag, which is the second largest contribution to the ice momentum balance when we assume a wind speed of 10 m/s. Note that for a mean ice thickness of 5 m, the internal pressure becomes larger than the atmospheric drag for concentrations higher than about 80%, and it shows a steep increase as concentration is increased further.

Consequently, if the analysis update artificially increases mean ice thickness or ice concentration in an area where they are already high, the model's ice advection reacts with strong compensating tendencies. This effect might not be desired in the data assimilation, as it will lead to an unrealistic sea-ice drift.

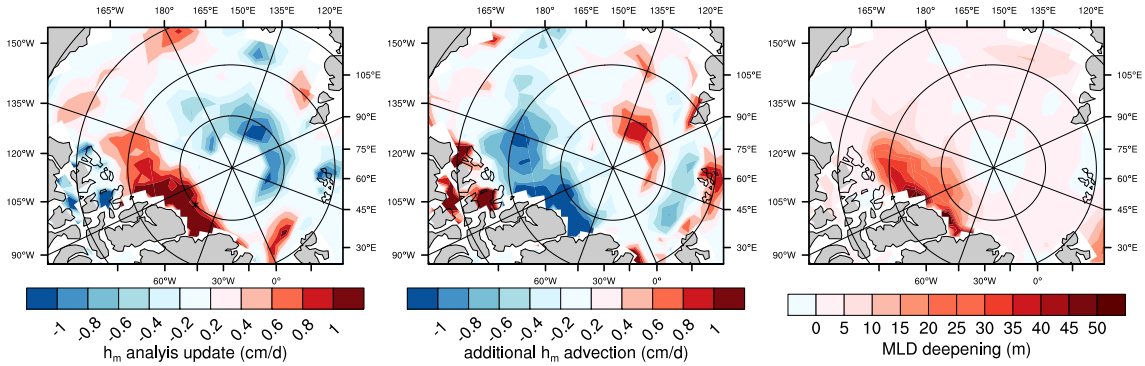

Figure 3.12: Mean-thickness analysis updates (left), additional mean-thickness advection (middle), and deepening of the mixed layer (right) when assimilating observed sea-ice concentration with the CAT method. Shown are the average September conditions north of the Canadian Archipelago in the decade 1990–1999. The middle and right plot are obtained by subtracting the average conditions in the 1990–1999 decade in the reference run.

In our assimilation experiments, this effect plays an important role north of the Canadian Archipelago during summer for the analysis updates that conserve actual thickness (CAT). North of the Canadian Archipelago, the model has a bias towards low ice concentrations during summer, and the mean ice thickness is quite high. Since for CAT the mean-thickness analysis updates are stronger when the background ice thickness is high, eq. (3.10), the analysis updates of ice volume are positive and strong there, and the ice pressure is kept at very high levels. The advective updates, as diagnosed from the AOGCM, then show a strong compensating reaction, which means that the ice is dispersed from this area into the rest of the Arctic ocean. Fig. 3.12 shows the typical situation in September, when the effect is most pronounced.

4 Predictability of large negative Arctic sea-ice anomalies

In the CMIP5 projections of 21st-century climate, Arctic sea ice declines, and at the same time exhibits strong interannual anomalies. Here, we investigate the potential to predict these strong sea-ice anomalies with the CMIP5 version of the Max-Planck-Institute Earth System Model under a perfect-model assumption. We study two cases of strong negative sea-ice anomalies: a five-year-long anomaly for present-day conditions, and a ten-year-long anomaly for conditions projected for the middle of the 21st century. We treat these anomalies in the CMIP5 projections as the truth, and use exactly the same model configuration for predictions of this synthetic truth. We start ensemble predictions at different times during the anomalies, considering two types of initial conditions: lagged-perfect and sea-ice-assimilated initial conditions. We find that the onset and amplitude of the interannual anomalies are essentially unpredictable. However, predictions of annual-mean sea-ice extent and volume that start from a state where the anomaly is already developed correctly predict the further deepening of the anomaly for typically one year lead time. These predictions are generally more skillful for present-day conditions than for conditions in the middle of this century. The magnitude of an extremely low summer sea-ice minimum is hard to predict: only for lead times up to a few months is the predictive skill better than damped persistence, and from lead times of two years on the predictive skill is not better than a climatology forecast. Initial conditions obtained by sea-ice data assimilation are competitive with lagged-perfect initial conditions for lead times of a year or less, but yield degraded skill on longer lead times. These results imply that there is limited and decreasing prospect of predicting the large sea-ice anomalies expected to occur throughout the 21st century.

4.1 Introduction

The mean state of Arctic sea ice has changed dramatically over the last few decades, and it is expected to continue to change at a high pace throughout the 21st century [*Arzel et al.*, 2005; *Boé et al.*, 2009]. The change in the mean state is accompanied by strong interannual to decadal variability [*Bengtsson et al.*, 2004; *Goosse et al.*, 2009]. Predictability of these unforced variations would be of great theoretical and practical value, because Arctic sea ice plays an important role in shaping weather and climate not only in polar regions, but also well beyond [*Bader et al.*, 2011]. Here, we use the Max-Planck-Institute Earth System Model to assess the predictability of large negative interannual anomalies in Arctic sea-ice cover.

Interannual predictions of Arctic sea ice for *perfect* initial conditions have been investigated by *Holland et al.* [2010]. They concluded that predictability of Arctic sea ice is lower for the 2010 decade than for the 1970 decade, supporting the notion that the strong trends in Arctic sea ice are associated with a changing predictability regime. Using similar experiments starting in the 2000 decade, *Blanchard-Wrigglesworth et al.* [2011b] pointed out that sea-ice predictability is dominated by secular trends for lead times that exceed three years.

However, predictions of real climate do not start from perfect initial conditions, because observations of the actual climate state are incomplete and climate models have errors. Therefore, predictions from non-perfect initial conditions that are obtained by assimilating observations into the climate model must be investigated.

Here, we test how much of the potential predictability determined in previous studies with perfect initial conditions can actually be realized when using non-perfect initial conditions obtained by the sea-ice data assimilation method developed in Chapter 3. We extend the discussion of Arctic sea-ice predictability to conditions expected for the 2050 decade under a moderate emission scenario, and specifically focus on predictions before and during large negative interannual sea-ice anomalies.

The chapter is structured as follows: Section 4.2 describes the climate model and the experimental methodology. Section 4.3 analyzes Arctic sea-ice variability in the climate-change projections that are used as the reference for the predictability study. Section 4.4 explains how we obtain initial conditions for ensemble predictions,

and Section 4.5 presents the results of the predictions. The chapter closes with an outlook in Section 4.6 and a summary of the main results in Section 4.7.

4.2 Model and methods

4.2.1 Earth system model and climate projections

We use the low-resolution version of the Max-Planck-Institute Earth System Model (MPI-ESM-LR) as it has been used for the Coupled Model Intercomparison Project Phase 5 (CMIP5). The atmosphere component is ECHAM6 with a T63 horizontal resolution and 47 vertical levels (M. A. Giorgetta et al., ECHAM6 model description, technical report in preparation). The model is the successor of ECHAM5 [*Roeckner et al.*, 2003], with the most notable improvements being related to the radiative transfer code. In comparison to the CMIP3 version of ECHAM5, the CMIP5 version of ECHAM6 has more vertical levels in the upper atmosphere, so that it is capable of representing internal variability in the stratosphere, which potentially has an impact on Arctic predictability via stratosphere–troposphere coupling [*Shepherd et al.*, 2011].

The ocean component is MPI-OM as described by *Marsland et al.* [2003] with a few minor modifications. The resolution of the ocean model is approximately 1.5° with 40 vertical levels. A dynamic–thermodynamic sea-ice model based on *Hibler III* [1979] is embedded in the ocean model. For a description of the ocean circulation obtained with MPI-OM when coupled to ECHAM5 see *Jungclaus et al.* [2006].

Land surface processes including a vegetation cover that dynamically adapts to changed climatic conditions are modelled with JSBACH [*Raddatz et al.*, 2007; *Brovkin et al.*, 2009]. Ocean biogeochemistry is modelled with HAMOCC [*Wetzel et al.*, 2005].

CMIP5 climate-change projections are defined in terms of representative concentration pathways (RCP). The RCP4.5 scenario prescribes a pathway of greenhouse gas concentration that approximately corresponds to an additional radiative forcing of $4.5\,\mathrm{Wm}^{-2}$ by 2100 [*Taylor et al.*, 2011; *Meinshausen et al.*, 2011]. The CMIP5 RCP4.5 climate projections for the 21st century obtained with MPI-ESM-LR serve as reference runs for the predictability case studies we perform.

4.2.2 Experimental methodology

We use three realizations of an RCP4.5 experiment with MPI-ESM-LR as reference runs. The sea-ice variability occurring in the reference runs is discussed in more detail in Section 4.3. By visual inspection, we select periods during the 21st century that show a pronounced difference in ice extent and ice volume between these runs. We treat the run with anomalously low sea ice as the truth and assess the potential to predict these anomalies, using exactly the same model setup but different initial conditions.

We compare predictions from two kinds of initial conditions: (i) *lagged-perfect initial conditions* that are obtained by perturbing the "true" model state that develops the anomaly and (ii) *sea-ice-assimilated initial conditions* that are derived from an independent model run which assimilates the "true" sea-ice concentration with the methods discussed in Chapter 3. Section 4.4 describes the method of obtaining ensemble initial conditions and their properties in more detail. All predictions are run with 9 ensemble members, so that we can diagnose some basic intra-ensemble statistical properties.

There are two important idealizations in the so-called perfect-model approach that we employ: first, model errors do not play a role in the predictability estimates we obtain, and second, we can start predictions from initial conditions that are as close to the truth as we want. Thus, predictability estimates obtained with the perfect-model approach are an optimistic *upper bound* on Arctic sea-ice predictability achievable with MPI-ESM-LR. If we do not find predictability in this setup, it is pointless to look for predictability in a more realistic setup. Hence, such a perfect-model predictability study helps guiding the research on predictability of the real climate.

We focus on two cases of strong negative interannual sea-ice anomalies for estimating sea-ice predictability: one for present-day conditions, and one for conditions in the middle of the 21st century. This allows us to compare predictability estimates at different times during the retreat of Arctic sea ice under a global warming scenario.

The case-study approach also allows for investigation of the relation between the *physical processes* and the presence or absence of predictability. As *Hermanson and*

Sutton [2009] pointed out, different initial climate states exhibit different degrees of predictability. Likewise, one would expect that the physical processes that govern this predictability depend on the initial climate state as well. A study that calculates predictive skill from the average over many predictions starting from many different climate states cannot make statements about the underlying processes if these change from case to case. As an example, consider the prediction of Arctic summer sea-ice extent. In one year, prevailing anomalous surface winds that push the ice together might be responsible for an anomalously low minimum [*Ogi et al.*, 2008], whereas in another year anomalous intrusion of warm surface water into the Arctic Ocean as discussed by *Woodgate et al.* [2010] might cause a similar response. Only by studying the two cases separately can we detect the underlying physical causes.

To quantify predictability, we compare the predicted sea-ice state to the sea-ice state of the synthetic truth and to two reference forecasts: climatology and damped persistence. Since Arctic climate is expected to change drastically during the 21st century, the definition of a climatology is complicated by the existence of strong secular trends. These trends lead to large predictive skill on interannual to decadal lead times if the model predicts the trend correctly. Although a skillful prediction based on that effect might be considered as a success when predicting the real climate, it is trivial in a perfect-model setup, where the trend is correctly predicted by construction. Hence, we neglect predictability that relies on trends and use a 30-year centered running mean as the time-dependent climatology. The so-defined climatology responds smoothly to the change in climate forcing and does not exhibit internally generated variability. To establish damped persistence as a second reference forecast, we approximate the anomaly time series of the sea ice state with an auto-regressive process and determine appropriate parameters (Section 4.3.3).

We use the *Brier skill score* (BSS) as a convenient nondimensional measure of the quality of a prediction [*von Storch and Zwiers*, 1999]. The BSS measures the skill of a prediction F relative to a reference forecast R by comparing the mean squared error of the forecast S_F^2 with the mean squared error of the reference forecast S_R^2:

$$\mathrm{BSS}_{RF} = 1 - \frac{S_F^2}{S_R^2}. \tag{4.1}$$

The BSS is 1 for a perfect forecast, 0 for a forecast that is as good as the reference forecast, and negative if the forecast is even worse than the reference.

We focus on predictions of yearly means and September means of northern-hemisphere sea-ice extent and volume. While yearly means are relevant for decadal time scales, the September minimum is the most interesting seasonal mean to predict, since (i) the variability is highest (see Section 4.3), and (ii) in September the ice edge is completely within the Arctic Ocean, whereas in winter the ice edge is spread over separate oceans such as the North Pacific, the North Atlantic, and the Labrador Sea. Hence, for summer predictability it should be feasible to identify a few important physical mechanisms, whereas winter predictability requires consideration of several unrelated physical mechanisms acting in the different regions.

4.3 Characterization of the reference runs

4.3.1 Arctic sea-ice variability

Three realizations of RCP4.5 climate projections with MPI-ESM-LR serve as the reference runs for our experiments. Figure 4.1 shows time series of some important Arctic climate variables for these runs between 1970 and 2100. During this time, Arctic sea-ice extent and volume decline (Fig. 4.1a–d), and Arctic surface air temperature and ocean heat content increase (Fig. 4.1e–f). In the second half of the 21st century, nearly ice-free summers in the Arctic Ocean start to occur. Note that the natural variability in these time series can be large enough to outweigh the secular trend for decades.

We obtain anomalies for each realization by subtracting the centered 30-year running mean. The resulting anomaly time series have a stationary mean by construction, whereas the variance might change over time. The variance of September ice extent (Fig. 4.1a) increases during the retreat of the ice. The mechanisms behind this were discussed by *Notz* [2009] and *Goosse et al.* [2009]. The variance of September ice volume (Fig. 4.1b), however, decreases. The variance for the annual-mean time series (Fig. 4.1c–f) stays approximately constant.

In this study, we will restrict ourselves to the prediction of Arctic sea ice itself. Nevertheless, there are strong correlations between anomalies in Arctic sea ice and

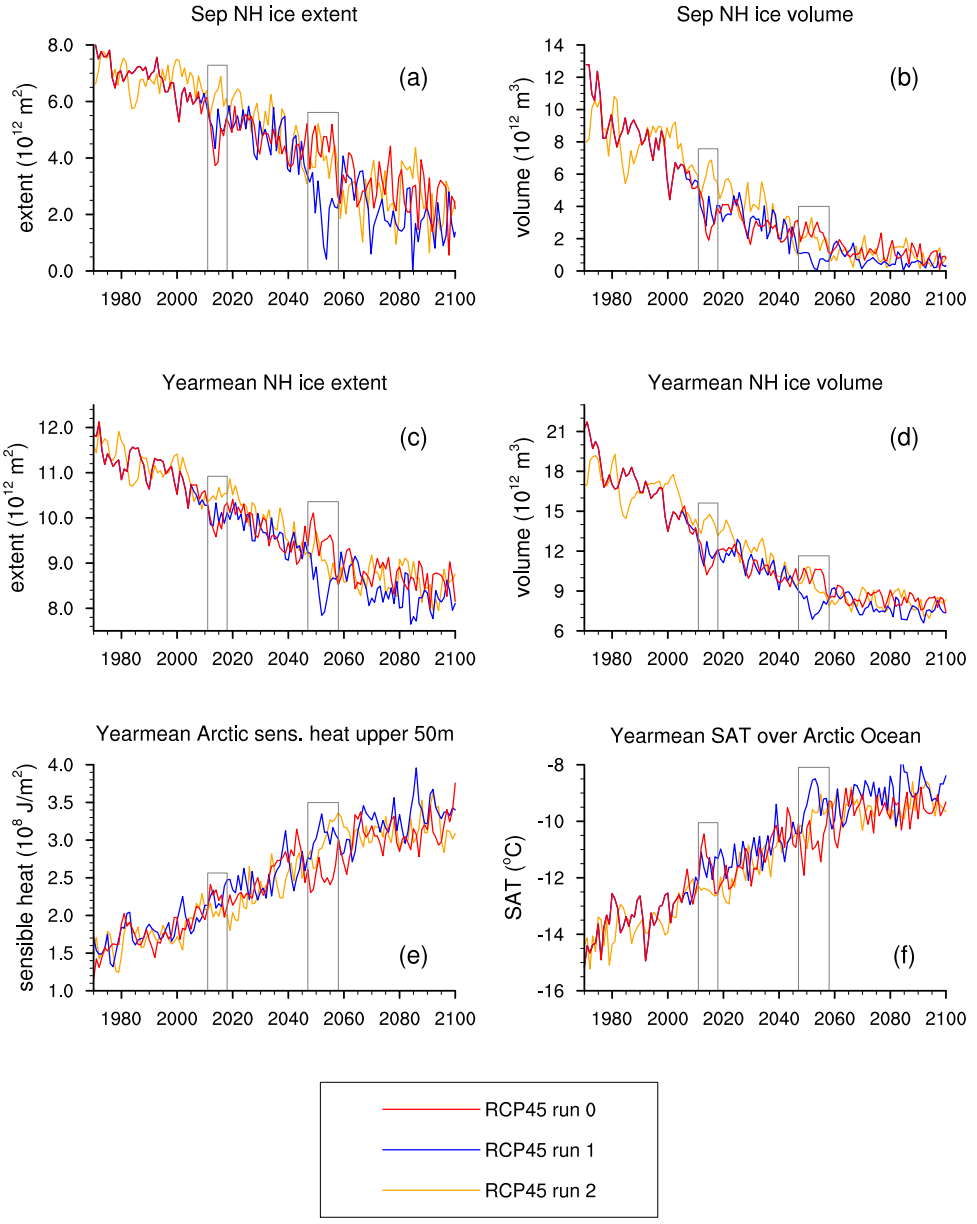

Figure 4.1: Time series of climate variables related to Arctic sea-ice cover for three realizations of the CMIP5 RCP4.5 climate projections with MPI-ESM-LR. Shown are September means of (a) ice extent and (b) ice volume, as well as annual means of (c) ice extent, (d) ice volume, (e) heat content in the upper 50 meters of the Arctic ocean, and (f) surface air temperature over the Arctic ocean. Rectangles mark the time windows of the strong interannual anomalies discussed in Sec. 4.3.2.

other Arctic climate variables. These correlations are clearly visible in Figure 4.2, which shows the scaled annual-mean anomalies of ice extent together with annual-mean anomalies of ice volume, heat content in the upper 50 m of the Arctic Ocean, and surface air temperature over the Arctic Ocean. We calculate cross-correlations between these anomalies by considering their time series for four RCP4.5 realizations. Three of these realization are the reference runs shown in Fig. 4.1, and a fourth is added to improve statistical robustness. This gives us 400 years of data, which show that sea-ice extent is positively correlated with sea-ice volume ($r = 0.75$), and negatively correlated with Arctic Ocean heat contet in the upper 50 m ($r = -0.67$) and Arctic surface air temperature ($r = -0.78$). The high absolute values of the correlation coefficient suggest that there are physical processes that robustly couple anomalies of these climate variables, so that sea-ice extent anomalies are a useful predictor (or proxy) for other Arctic climate variables.

4.3.2 A present-day and a mid-century case of a large interannual sea-ice anomaly

From visual inspection, we choose two cases where one realization of the RCP4.5 runs happens to have a strong negative anomaly, while another realization has a positive anomaly. We define the temporal extent of an interannual Arctic sea-ice anomaly using the 12-month running mean: the anomaly lasts as long as the 12-month running mean of northern-hemisphere ice volume is continuously below the climatological mean.

We choose one case for present-day conditions and one for mid-century conditions. In the present-day case, realization 0 has a strong negative sea-ice anomaly that starts in 2011 and lasts until 2017, with a maximal expression in 2014. In the mid-century case, realization 1 has a strong negative sea-ice anomaly that lasts from 2047 to 2057, with a maximal expression in 2053 (see Figure 4.1).

The range of natural variability demonstrated by these extreme cases is quite remarkable. Figure 4.3 shows the September ice extent in 2014 and 2053. In 2014, September ice extent is less than $4 \cdot 10^6\,\mathrm{km}^2$ in realization 0, while it is more than $7 \cdot 10^6\,\mathrm{km}^2$ in realization 2. In 2053, realization 1 is almost ice-free in September, while realization 2 shows an ice extent of more than $4 \cdot 10^6\,\mathrm{km}^2$.

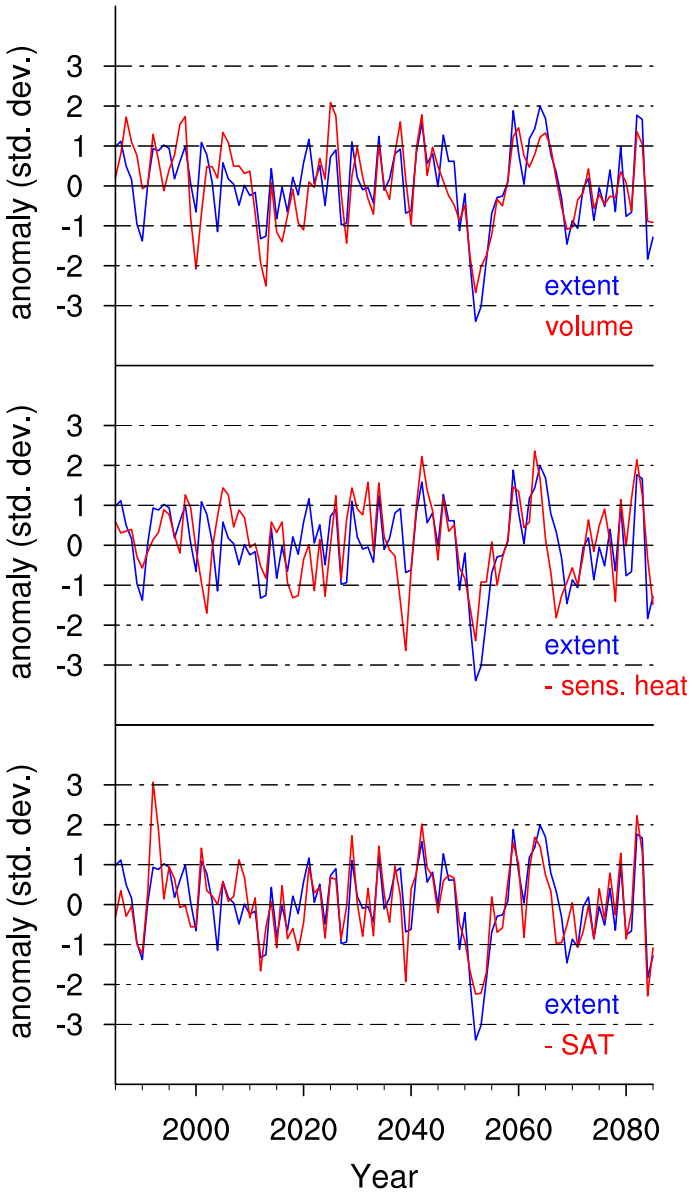

Figure 4.2: RCP4.5 run 1 annual-mean time series of anomalies of northern hemisphere sea-ice extent together with anomalies of northern-hemisphere sea-ice volume (top), inverted anomalies of heat content in the upper 50 m of the Arctic Ocean (middle), and inverted anomalies of surface air temperature over the Arctic Ocean (bottom). All anomaly time series are scaled by their respective standard deviations.

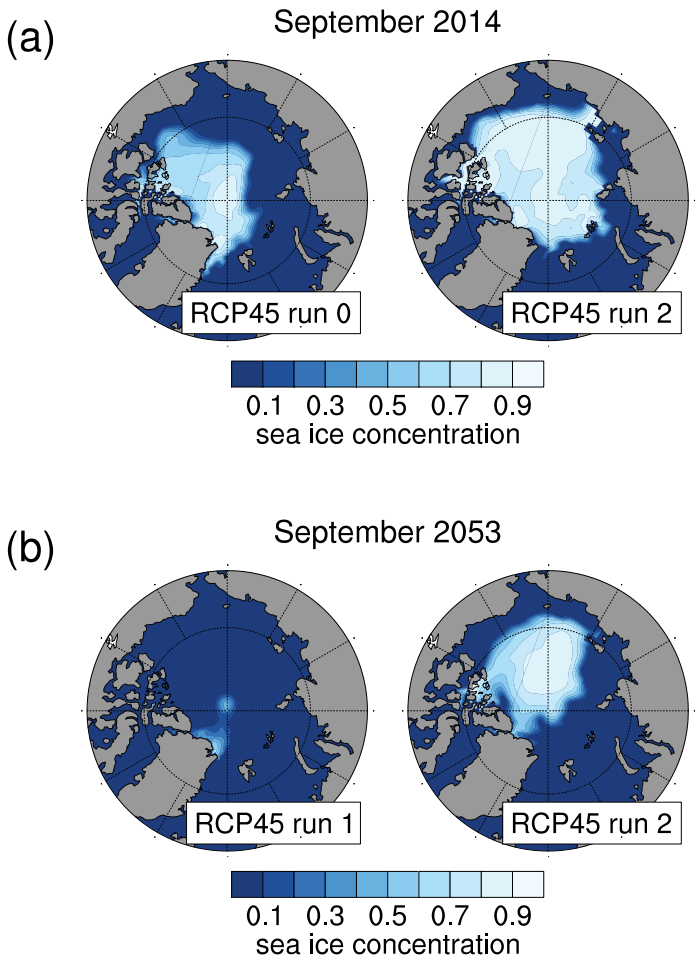

Figure 4.3: Comparison of northern-hemisphere sea-ice concentration in September for different realizations of the RCP4.5 experiments. (a) for 2014, the year with the lowest extent during the present-day anomaly, and (b) for 2053, the year with the lowest extent during the mid-century anomaly.

To judge if these anomalies are extreme, we compare them with the standard deviation of the anomaly time series between 1970 and 2100: The maximal amplitude of the mid-century anomaly is around three standard deviations for yearly-mean extent and volume, more than three standard deviations for September ice extent, and close to two standard deviations for September ice volume. For the present-day anomaly, the maximal expression is more than two standard deviations for yearly-mean ice extent, more than three standard deviations for yearly-mean ice volume, and around three standard deviations for September ice extent and volume.

4.3.3 Fitting an autoregressive process to sea-ice anomalies

We use an auto-regressive (AR) process to approximate the statistical properties of the anomaly time series of annual-mean sea-ice extent and volume. From the AR process, *damped-persistence* forecasts can easily be constructed, which then serve as a benchmark for dynamical predictions with MPI-ESM-LR. All methods used in this section can be found in the textbooks by *von Storch and Zwiers* [1999] and *Box et al.* [2008].

To estimate the parameters of the AR process that approximates the time series best, we calculate the autocorrelation function (ACF) and the partial autocorrelation function (PACF). The lag-k ACF of a stationary random process $\{x_t\}$ is defined as the correlation between two realizations of the process separated by a time difference k:

$$\mathrm{ACF}(k) = \mathrm{corr}[x_t, x_{t-k}].$$

The PACF is a helpful tool for determining the order of an AR process, because the PACF of an AR process of order k has a cutoff after lag k. The lag-k PACF of a stationary random process $\{x_t\}$ is defined as the correlation between the "adjusted values" of two realizations of the process separated by a time difference k:

$$\mathrm{PACF}(k) = \mathrm{corr}[x_t - \hat{x}_t, x_{t-k} - \hat{x}_{t-k}],$$

where the adjustments $\hat{x}_t$ and $\hat{x}_{t-k}$ are the best linear predictors of x_t and x_{t-k} based on the realizations $x_{t-1}, x_{t-2}, \ldots, x_{t-k+1}$ (*Box et al.* [2008], pp. 66ff.).

We estimate the ACF and the PACF from four RCP4.5 realizations for the time

between 1970 and 2100. Three of these realization are the reference runs introduced in Fig. 4.1, and a fourth is added to improve statistical robustness. The estimated ACF and PACF of annual-mean sea-ice extent and volume are shown in Figure 4.4.

Figures 4.4a,b show that both extent and volume have highly significant autocorrelation for a lag of one year, and marginally significant autocorrelation for a lag of two years. Interestingly, marginally significant negative correlation emerges at lags of about 10 years, which suggests that the time series tend to oscillate around the running mean with a 20-year period. However, for the purpose of constructing statistical reference forecasts for only a few years lead time these higher-order effects are not relevant, and so we do not discuss them here further.

The PACF of the annual-mean extent time series is not significantly different from zero for lags greater than one (Fig. 4.4c). This indicates that a first-order AR is an appropriate statistical model. The Yule-Walker estimate of the lag-1 autoregression coefficient for annual-mean ice extent is $\alpha_1 = 0.5$. For annual-mean sea-ice volume there is marginally significant negative partial autocorrelation for lag 2 (Fig. 4.4d), and so a second-order AR process is the appropriate description. The Yule-Walker estimate of the lag-1 and lag-2 autoregression coefficients for annual-mean ice volume are $\alpha_1 = 0.8$ and $\alpha_2 = -0.2$.

For September anomalies of sea-ice extent and volume, the same procedure suggests first-order autoregressive processes with estimates of the lag-1 autoregression coefficient of $\alpha_1 = 0.4$ and $\alpha_1 = 0.5$, respectively.

4.4 Obtaining ensemble initial conditions

We investigate predictions from two kinds of initial conditions: perfect initial conditions, where the full model state is close to the true state, and sea-ice-assimilated initial conditions, which are obtained from an independent run that assimilates the "true" sea-ice concentration with the methods described in Chapter 3. By comparing these two kinds of initial conditions, we can assess how much prognostic sea-ice predictability there is, and how much of it we can realize by initializing the sea-ice state.

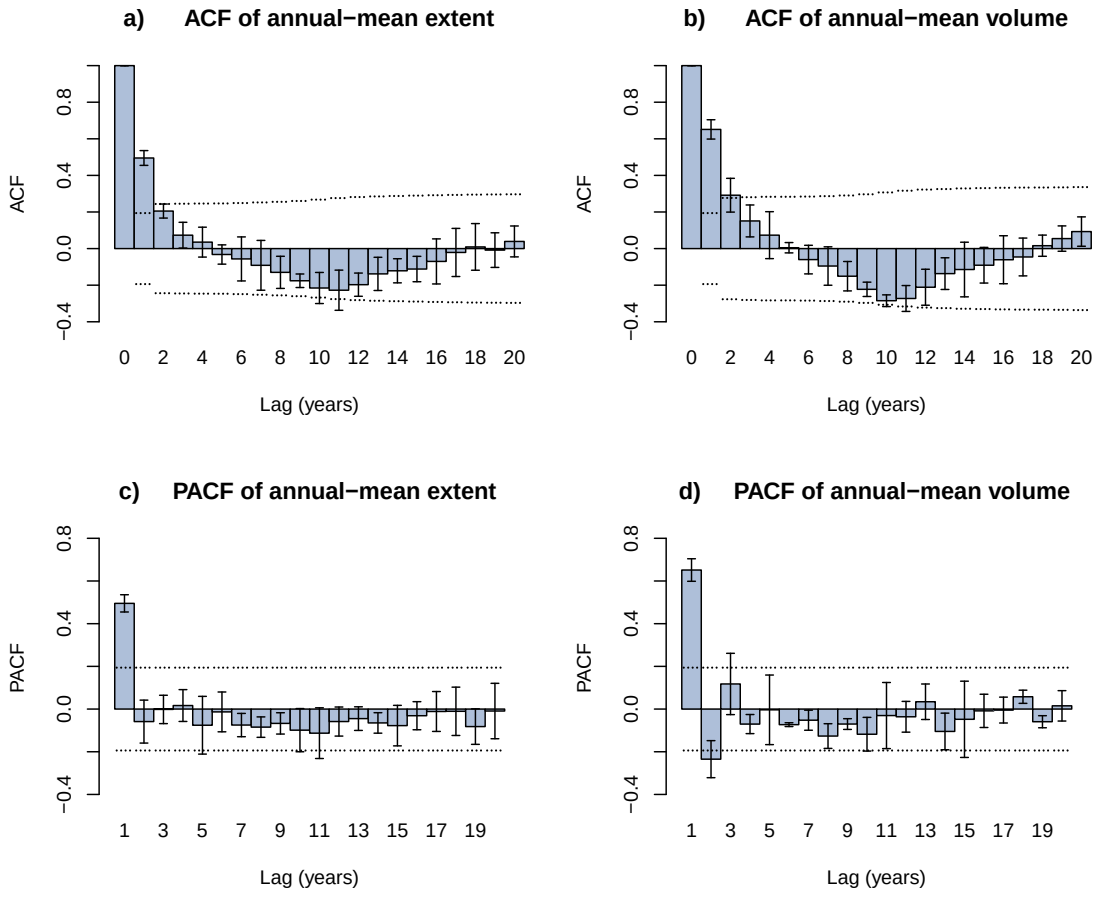

Figure 4.4: Autocorrelation function (ACF) and partial autocorrelation function (PACF) for annual-mean sea-ice extent and volume from four realizations of an RCP4.5 run. The ensemble mean and spread of (partial) autocorrelation are given by columns with standard error bars. Significance of (partial) autocorrelation can be inferred from the location of ensemble mean and spread with respect to the dotted lines, which represent the 95% confidence interval of the null hypothesis of zero (partial) autocorrelation. To obtain the lag-dependent confidence interval for the ACF, we use Bartlett's large-lag approximation. The confidence interval of the PACF is lag-independent (see *Box et al.* [2008]).

The sea-ice assimilation run starts from a RCP4.5 realization that shows a positive anomaly during the time when the truth run has a negative anomaly, so that the difference between the two is maximal during the time when we perform the assimilation. RCP4.5 realization 2 has such a positive sea-ice anomaly both for the present-day case study and the mid-century case study, so we take the initial conditions for the assimilation run from realization 2 (see Figures 4.1 and 4.3).

Figure 4.5 shows July monthly means of selected Arctic sea-ice related quantities during the present-day case study. The assimilation run starts in January 2010 from run 2, which exhibits a positive sea-ice anomaly from 2013 to 2018. We show the July monthly mean, because the interannual predictions in Section 4.5.1 all start in August. From Figure 4.5 we see that northern-hemisphere sea-ice extent and volume as well as the heat content in the upper 50 m of the Arctic Ocean agree reasonably well between the assimilation and the truth run. This means that the conditions in the true state of these variables were successfully assimilated. However, this is not true for other properties of the climate system. As an example, we show the heat content of the upper 500 m of the Arctic Ocean. This quantity potentially plays a role in sea-ice predictability, because the heat stored in that layer is sufficient to melt the entire ice cover several times over. Since the assimilation is restricted to surface properties, the 500 m heat content stays close to run 2 and is hence effectively not initialized.

For the mid-century case study, the assimilation run starts in January 2049 from RCP4.5 realization 2. The July time series of sea-ice related quantities show qualitatively the same behavior as in the present-day case study (Fig. 4.6). However, the assimilation error is a bit larger than in the present-day case.

We obtain an ensemble of initial conditions by using the model state from several days adjacent to the start date of the prediction. With an ensemble size of 9, we take the model state from the actual start date, from one to four days before the start date, and from one to four days after the start date.

With this so-called lag-initialization approach, the perturbations to the initial conditions are exactly the differences between model states separated by a few days. Thus, the perturbation in the initial conditions is small for slow components of the climate system like ocean water mass properties and sea-ice cover, and larger for fast components like the atmosphere.

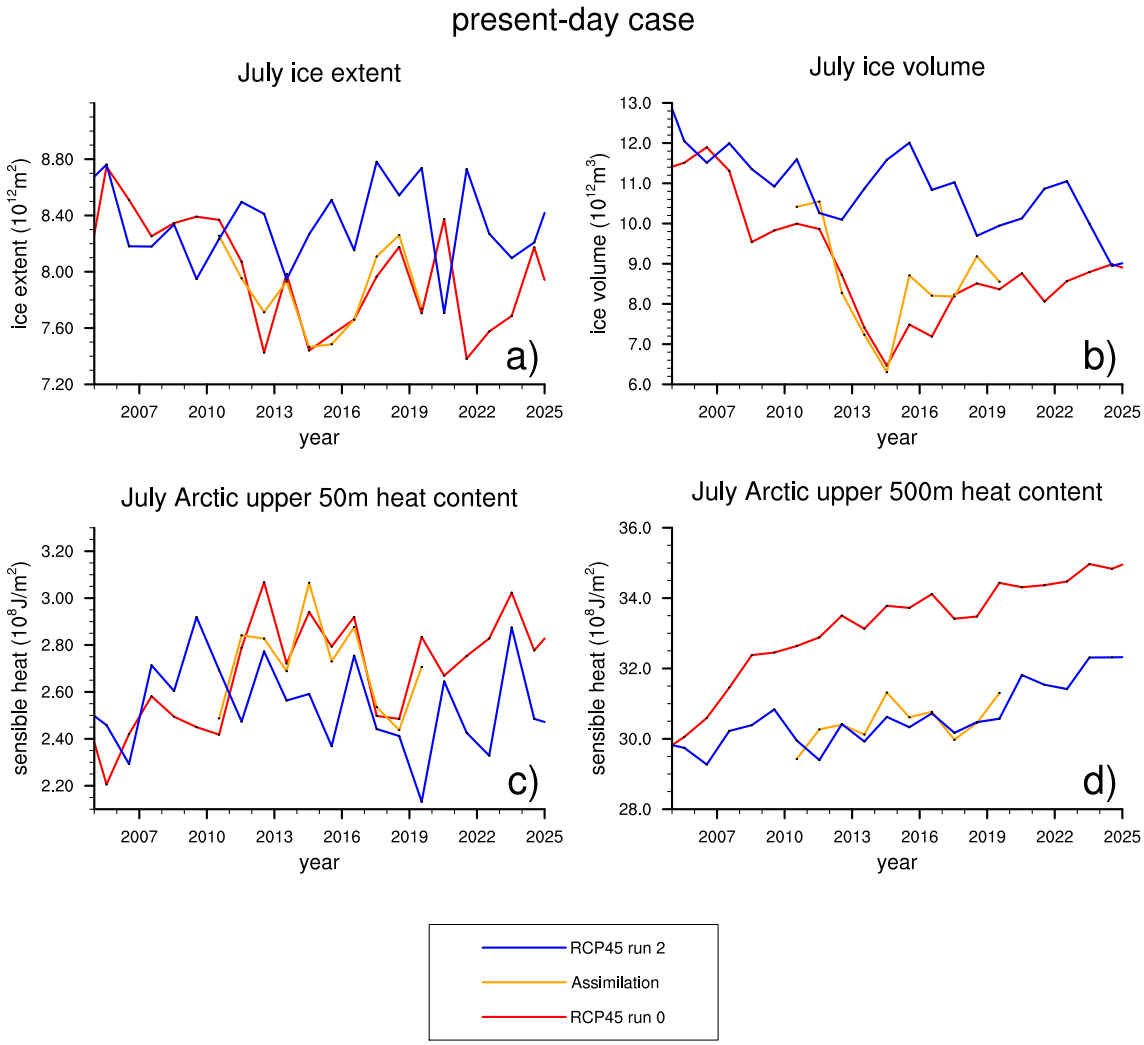

Figure 4.5: Time series of selected Arctic climate variables in July for the present-day case reference runs. Shown are (a) ice extent, (b) ice volume, (c) heat content in the upper 50 m and (d) in the upper 500 m of the Arctic Ocean. The assimilation run starts from the RCP4.5 run 2, which has high ice extent and volume, and assimilates ice concentration of the RCP4.5 run 0, which has low ice extent and volume.

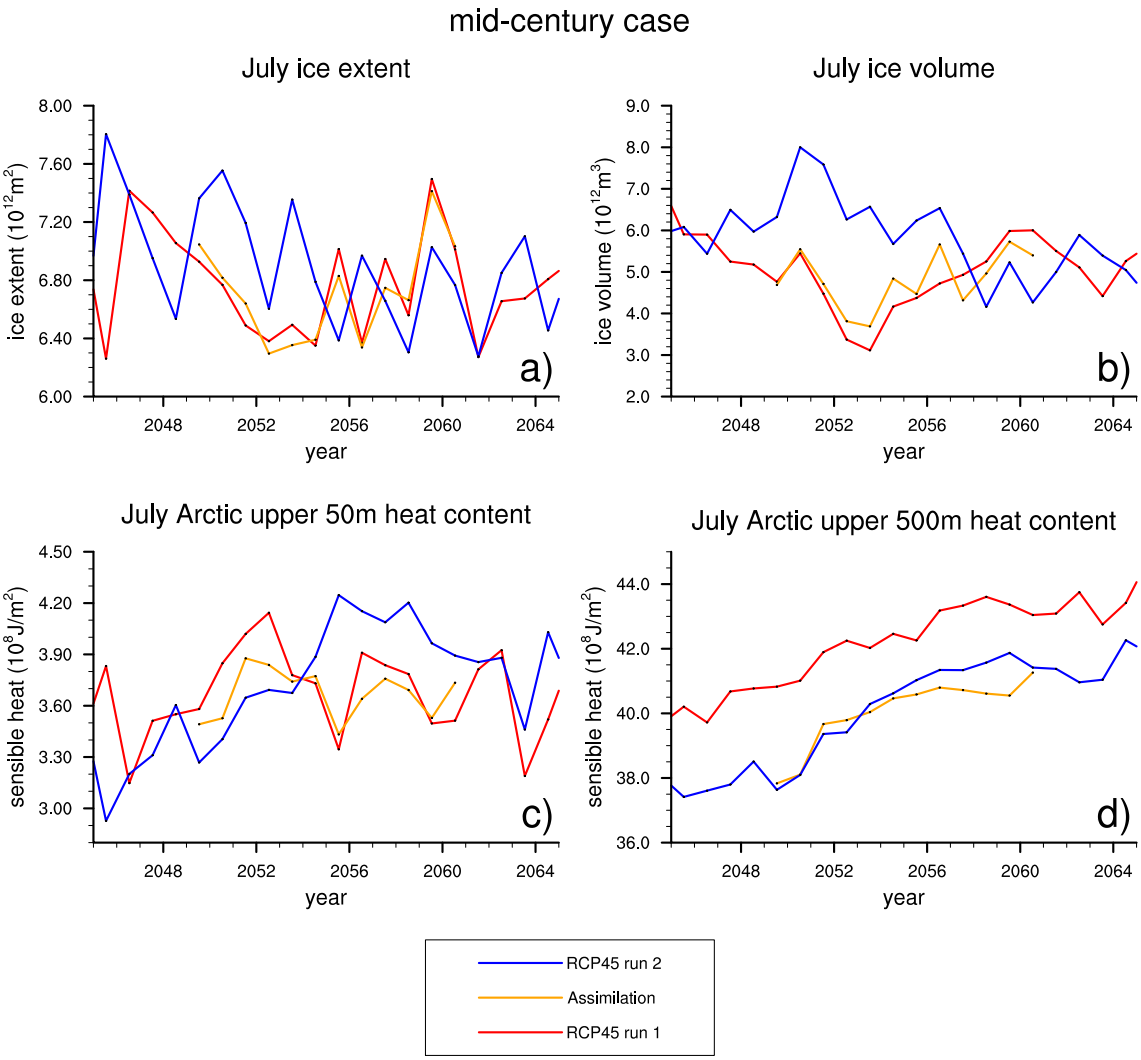

Figure 4.6: Time series of selected Arctic climate variables in July for the mid-century case reference runs. Shown are (a) ice extent, (b) ice volume, (c) heat content in the upper 50 m and (d) in the upper 500 m of the Arctic Ocean. The assimilation run starts from the RCP4.5 run 2, which has high ice extent and volume, and assimilates ice concentration of the RCP4.5 run 1, which has low ice extent and volume.

To illustrate the differences between the initialization of sea ice, ocean and atmosphere, we consider the fields of northern-hemisphere sea-ice thickness h, global ocean temperature T at 200 m depth, and global atmospheric surface pressure p. The perfect initial conditions for the prediction start day d are $h(P,d)$, $T(P,d)$ and $p(P,d)$. These fields are represented by their model state vector, which contains one entry for each of the N model grid cells. For h we write

$$h(P,d) \equiv \{h_i(P,d) : i = 1,\ldots,N\},$$

and the notation for T and p is analogous. Initial conditions from an arbitrary model run R at day $d \pm n$ are denoted by $h(R, d \pm n)$. We construct a simple measure of how "close" arbitrary initial conditions are to the perfect initial conditions by calculating the mean and variance of their field difference:

$$\mu_h(R,d\pm n) := \frac{1}{N}\sum_{i=1}^{N}\big(h_i(R,d\pm n) - h_i(P,d)\big)$$
$$\sigma_h^2(R,d\pm n) := \frac{1}{N}\sum_{i=1}^{N}\big(h_i(R,d\pm n) - h_i(P,d)\big)^2,$$

and analogously for the 200 m ocean temperature fields T and the atmospheric surface pressure fields p.

To decide whether the perturbation created by the lag initialization is small, we compare the mean and variance of the field difference with respect to the perfect initial conditions for (i) the lagged-perfect initial conditions, i.e. $\mu(P, d \pm n)$ and $\sigma(P, d \pm n)$, (ii) for S, the second RCP4.5 realization at the same day, i.e. $\mu(S,d)$ and $\sigma(S,d)$, and (iii) for A, the assimilation run at the same day, i.e. $\mu(A,d)$ and $\sigma(A,d)$.

Figure 4.7 shows the mean and variance of the difference of the initial condition fields to the perfect initial condition when starting a prediction on 1st August 2053. By construction $\mu(P,d) = \sigma(P,d) = 0$. With each day of lag forward or backward, the spread $\sigma(P, d \pm n)$ in the initial conditions becomes larger. For the sea-ice thickness field (Fig. 4.7a), the mean and spread of difference is comparable to lagged-perfect conditions for the assimilated-sea-ice initial conditions, but much larger for

initial conditions taken from S, the second RCP4.5 realization. This confirms that both lagged-perfect and assimilated initial conditions for sea ice are close to the perfect initial conditions when compared to the range of natural variability. For the ocean temperature field at 200 m depth (Fig. 4.7b), the lagged-perfect initial conditions show a much smaller spread than both the initial conditions from the sea-ice assimilation run and the second RCP4.5 realization, illustrating that the state of the subsurface ocean is well initialized in the lagged-perfect ensemble, but effectively not initialized in the assimilation run. Finally, the atmospheric fields (Fig. 4.7c) show a much faster separation of the initial conditions: already four days of lag are sufficient to reach the climatological spread, which does not become larger when considering the assimilation run or the second RCP4.5 realization. We conclude that (i) initial conditions from all runs have only weak constraints on the atmospheric state, (ii) initial conditions from the assimilation run do not constrain the global ocean state, and (iii) lagged-perfect initial conditions constrain both the ocean and the sea-ice state to a near-perfect initialization.

4.5 Sea-ice predictability

4.5.1 Predicting large interannual sea-ice anomalies

We now discuss predictions of pan-Arctic annual-mean ice extent and volume that are initialized at different stages of the large interannual sea-ice anomalies described in Section 4.3.2. The predictions start in August and have a lead time of three years. With this set of ensemble predictions, we assess the predictability of the *amplitude* and the *temporal extent* of the large interannual sea-ice anomalies. Additionally, we start one prediction in January before the onset of the mid-century anomaly that has a lead time of 12 years. With this ensemble prediction, we assess if the *onset* of the anomaly is predictable.

In our annual-mean prediction experiments, ensemble spread depends only weakly on the lead time and is only slightly below the level of natural variability. Nevertheless, we will see that the predictive skill is nontrivial and depends strongly on lead time. Therefore we must conclude that widely used indirect indicators of predictability that rely solely on the ensemble spread, such as the *potential prognostic*

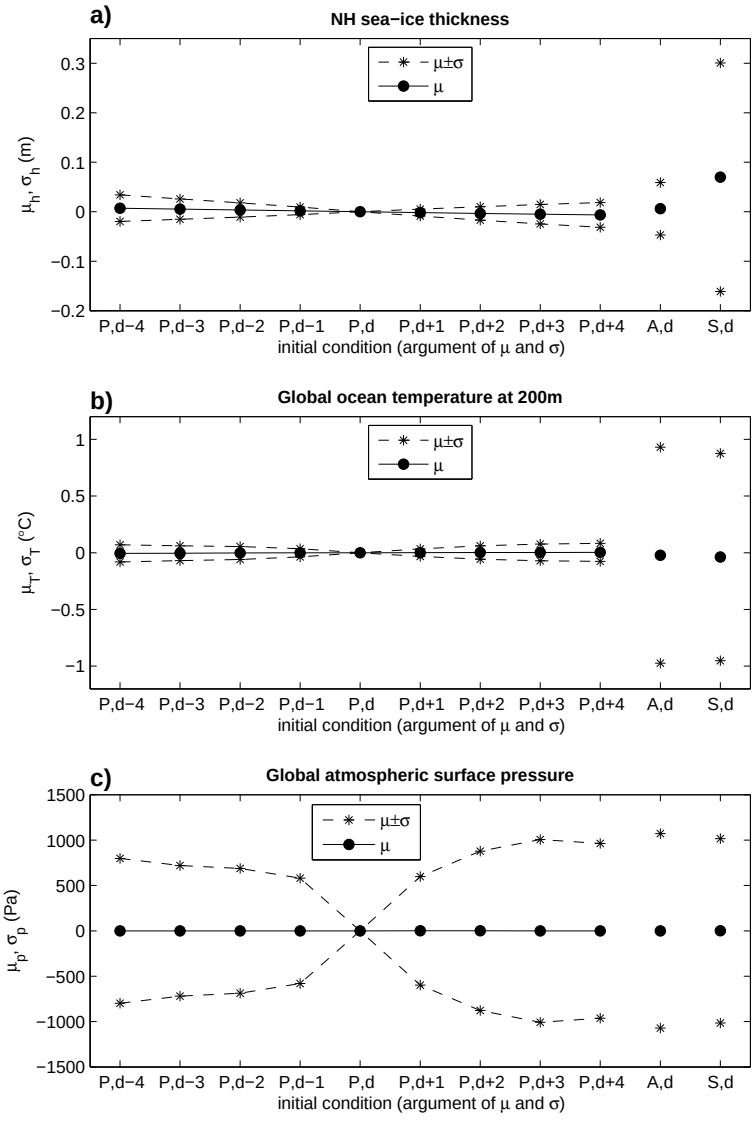

Figure 4.7: Mean and variance of the differences between initial condition (IC) fields used for the ensemble predictions. (a) sea-ice thickness north of 70°N, (b) global 200m ocean temperature, and (c) global atmospheric surface pressure. IC $(P, d-4)$ to $(P, d+4)$ are model states from the RCP4.5 run 1 between 27 Jul and 4 Aug 2053, which are used as the lagged-perfect initial conditions. IC (A, d) is from the sea-ice assimilation run on 31 Jul 2053, and IC (S, d) is from the RCP4.5 run 2 on 31 Jul 2053, which has higher ice volume and extent than the RCP4.5 run 1. All differences are calculated with respect to the IC (P, d), which are the perfect initial conditions that lead to a perfect prediction.

predictability [*Pohlmann et al.*, 2004; *Koenigk and Mikolajewicz*, 2008; *Holland et al.*, 2010], are not useful here.

The ensemble means of predicted sea-ice extent are shown in Figure 4.8 together with the reference run from which predictions are initialized and that they try to predict. The means of two reference forecasts are also shown, the time-dependent climatology and damped-persistence forecasts. Climatology is given by the centered 30-year running mean, and the damped-persistence forecasts are constructed according to *Box et al.* [2008] from the statistical model that was fitted to the sea-ice time series in Section 4.3.3. Initial conditions for the prediction ensembles are (i) lagged-perfect initial conditions and (ii) sea-ice-assimilated initial conditions (see Section 4.4). Since the ensemble spread depends only weakly on the lead time and is only marginally different for lagged-perfect and sea-ice-assimilated initial conditions, we show it as a single range. The results for the predicted sea-ice volume are similar to those of the predicted extent and are therefore not shown here.

For the present-day case study (Fig. 4.8a), the predictions in general show the following behavior: if started after the onset but before the maximal expression of the anomaly (start years 2012 and 2013), the ensemble mean correctly predicts the deepening of the anomaly for a certain lead time of typically one year. After that time, the predicted ensemble mean behaves similarly to damped persistence until the climatological mean is reached. If we extended the predictions to longer lead times, the predicted ensemble mean would follow the climatology (see discussion by *Branstator and Teng* [2010]). Predictions starting at the maximal expression of the anomaly (start year 2014) have a comparatively low mean error because their regression to the climatological mean coincides with the decay of the anomaly that happens in the reference run.

We consider the correct prediction of the deepening of the anomaly a very important point, since this is impossible using a simple damped-persistence forecast. However, the ensemble mean generally underestimates the strength of the deepening and returns to the climatological mean too early. Thus, neither the *amplitude* nor the *temporal extent* of the interannual anomaly are predictable.

The mean errors of the predictions in Figure 4.8a that start from sea-ice-assimilated initial conditions are sometimes comparable with, but generally higher than, those of the predictions started from lagged-perfect initial conditions. This result is to

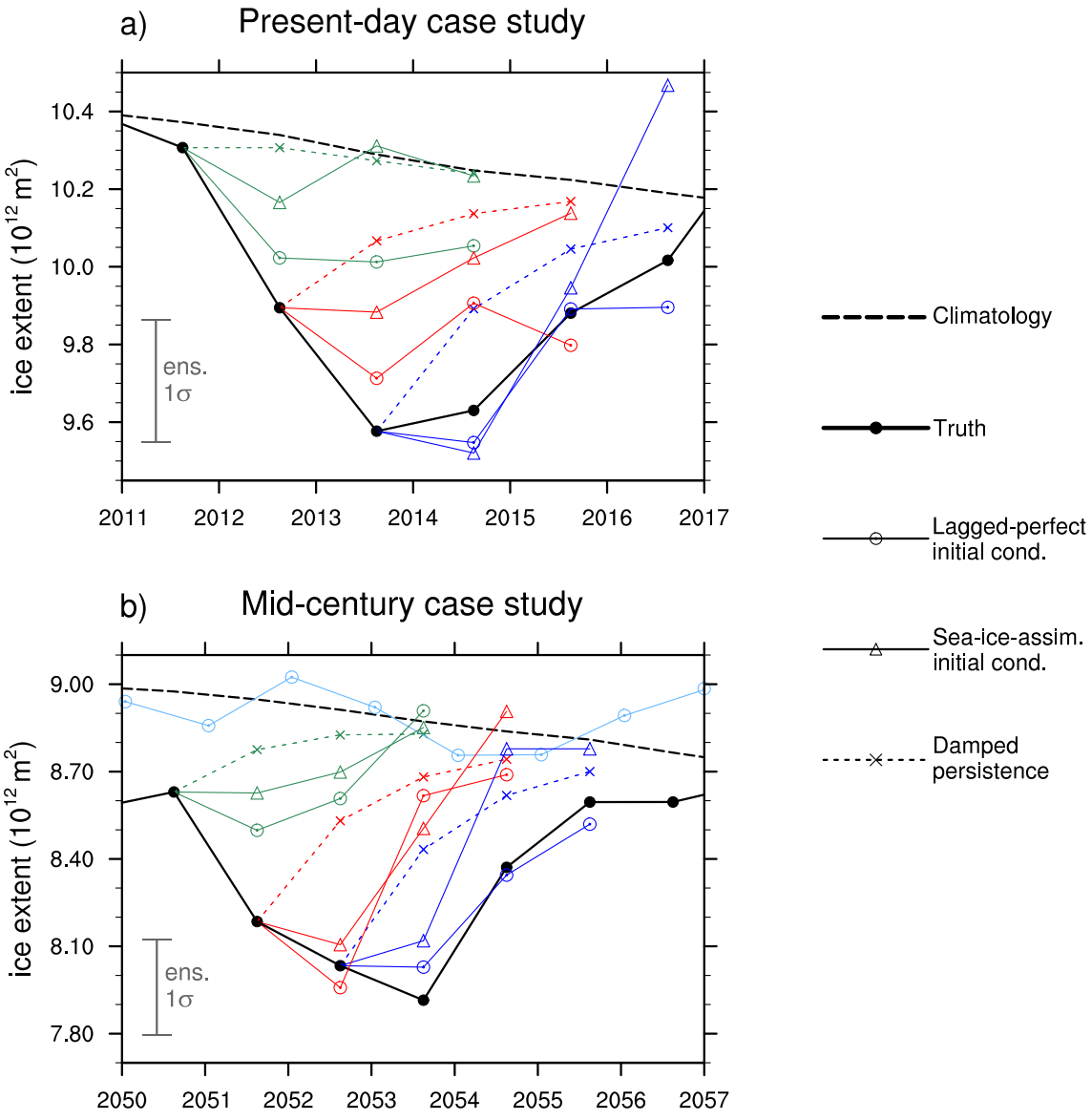

Figure 4.8: Predicted annual-mean northern-hemisphere sea-ice extent for (a) the present-day case study and (b) the mid-century case study. The black solid line is the annual mean of the RCP4.5 run that we consider as the truth. The black dashed line is the climatology defined by the centered 30-year mean. The ensemble mean of the predictions is denoted by the colored markers connected with solid lines. The ensemble spread of the predictions is indicated in the lower left of the plot. The means of damped-persistence reference forecasts are denoted by colored crosses connected with dashed lines. Colors correspond to the start year of the prediction: green for 2012/2051, red for 2013/2052, blue for 2014/2053, light blue for 2047.

be expected, as the components of the climate system that were not correctly initialized influence the sea-ice state. For the sea-ice-assimilated initial conditions, the predicted mean can overshoot the climatology instead of approaching it (start year 2014). This is most likely due to the fact that there is still information in the initial conditions about the "cold" state from which the assimilation run started, which is evident from the time series of heat content in the upper 500 m in the Arctic Ocean shown in Fig. 4.5d.

For the mid-century case study shown in Fig. 4.8b, the general features of the prediction means are as described for the present-day case study. We perform an additional prediction that starts from lagged-perfect initial conditions in January 2047, before the onset of the interannual anomaly. This ensemble does not predict the anomaly at all; instead, it stays close to the climatological mean throughout the whole lead time. From this we conclude that the *onset* of the mid-century interannual anomaly is essentially unpredictable.

To allow for a more convenient comparison of predictive skill between mid-century conditions and present-day conditions on the one hand, and between ice extent and ice volume on the other hand, we calculate the Brier Skill Score (BSS), defined in Eq. (4.1), of the prediction ensembles with respect to the climatological forecasts. The mean squared error of the predictions at each lead year is calculated from 24 individual prediction errors obtained from 3 different start dates with 8 lagged perfect initial condition each. The mean squared error of the climatological forecast is calculated from the known mean and standard deviation of the climatology.

Fig. 4.9 shows the BSS of the predictions from lagged-perfect initial conditions for lead years 1 to 3 with respect to a climatological forecast. The BSS is fairly similar for sea-ice extent and sea-ice volume. The strong lead-time dependence of BSS in all cases is evident. For the first lead year, BSS is 0.9 in all cases considered, whereas for the third lead year, it drops to 0.6 for present-day conditions and to 0.1 for mid-century conditions. We note that predictive skill for the third lead year is substantially higher for present-day than for mid-century conditions. This result is consistent with the intuitive notion that a thinner ice pack is less predictable and is supported by findings of *Holland et al.* [2010]. However, further analysis is required to determine the physical causes of such a loss of predictability during the thinning of the northern-hemisphere sea-ice cover.

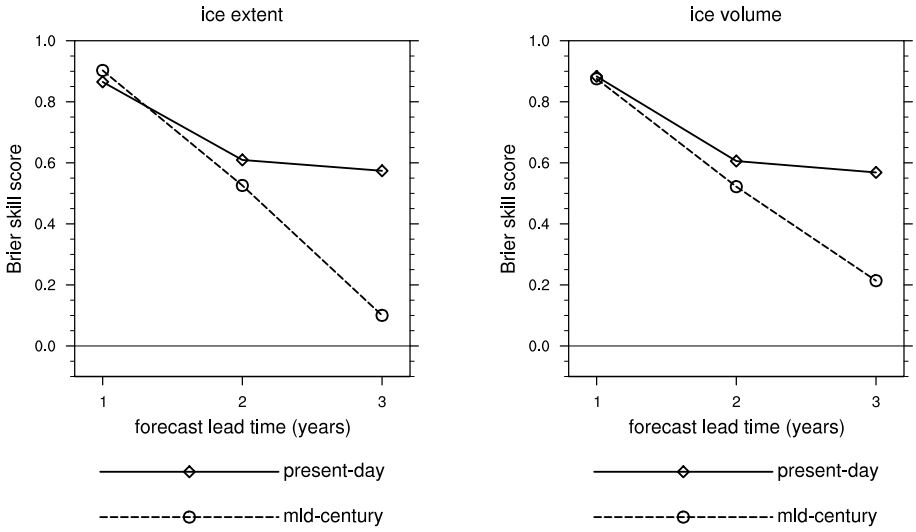

Figure 4.9: Lead-time dependence of Brier skill score for the predictions of annual-mean sea-ice extent (left) and annual-mean sea-ice volume (right). The score is calculated for the predictions started from lagged-perfect initial conditions with respect to a climatology forecast.

4.5.2 Predicting exceptionally low September sea ice

We now investigate the predictability of an exceptionally low September sea-ice minimum. The interannual sea-ice anomalies discussed in the previous section are most strongly pronounced in the summer season (see Section 4.3). For instance, while the run that we treat as the synthetic truth is almost ice-free in September 2053, realization 2 of the same model setup has an ice extent of more than $4 \cdot 10^6\,\mathrm{km}^2$, which is comparable to present-day conditions (Fig. 4.3b). Although the strong signal might encourage us to expect high predictability, a number of studies have shown that the magnitude of the summer minimum of Arctic sea ice is mostly controlled by fast atmospheric processes [*Ogi et al.*, 2008; *Kauker et al.*, 2009; *Holland et al.*, 2010], which suggests that there is little predictability.

We analyse ensemble predictions that are set up exactly in the same way as in the previous section. We focus on the lead-time dependence of predictability for two particular events: the September sea-ice state at the maximal expression of the interannual anomaly, which happens in 2014 for the present-day case study and in 2053 for the mid-century case study. The predictions start in August, May

and February of the same year, in August of the previous year, and in November two years before the September that we predict. As in the previous section, we compare predictions from lagged-perfect initial conditions and sea-ice-assimilated initial conditions.

Figure 4.10 shows the predicted ice extent as a function of lead time for September 2014 and September 2053. The results for the predicted sea-ice volume are similar to those of the predicted extent and are therefore not shown here.

For the present-day case study shown in Fig. 4.10a, all predictions except those with a very short lead time of one month are biased towards the climatological mean, which confirms the notion that the predictand is an extreme event. The ensemble means of the predictions starting from lagged-perfect initial conditions converge quite regularly towards the climatology with increasing lead time. Because of the perfect-model assumption, any prediction started sufficiently long in advance will on average predict the climatology. We see that this is already the case when starting in November two years before the predicted September. Therefore, for lead times of two years or more a skillful prediction of the extreme low in September sea ice extent is impossible. The damped-persistence forecast can only be beaten if predictions start in the winter before the predicted September, or even later.

From Fig. 4.10a we also see that the mean error of predictions from sea-ice-assimilated initial conditions is comparable to the mean error of predictions from lagged-perfect initial conditions for lead times of up to one year. Considering the results from the interannual predictions, this suggests that either (i) the importance of sea-ice initial conditions relative to the initial conditions of the other components of the climate system is higher for the prediction of summer conditions than for the prediction of annual-mean sea-ice conditions, or (ii) the initial conditions of non-sea-ice initial conditions only matter for lead times longer than a year.

For the mid-century case study shown in Fig. 4.10b, the general features of the mean predicted ice extent are as described for the present-day case study shown in Fig. 4.10a. However, there are two apparent differences: first, the mean error of the predictions from lagged-perfect initial conditions at lead times between 4 and 13 months relative to the mean error of a climatological forecast is higher than for the present-day case. Second, the predictions from sea-ice-assimilated initial

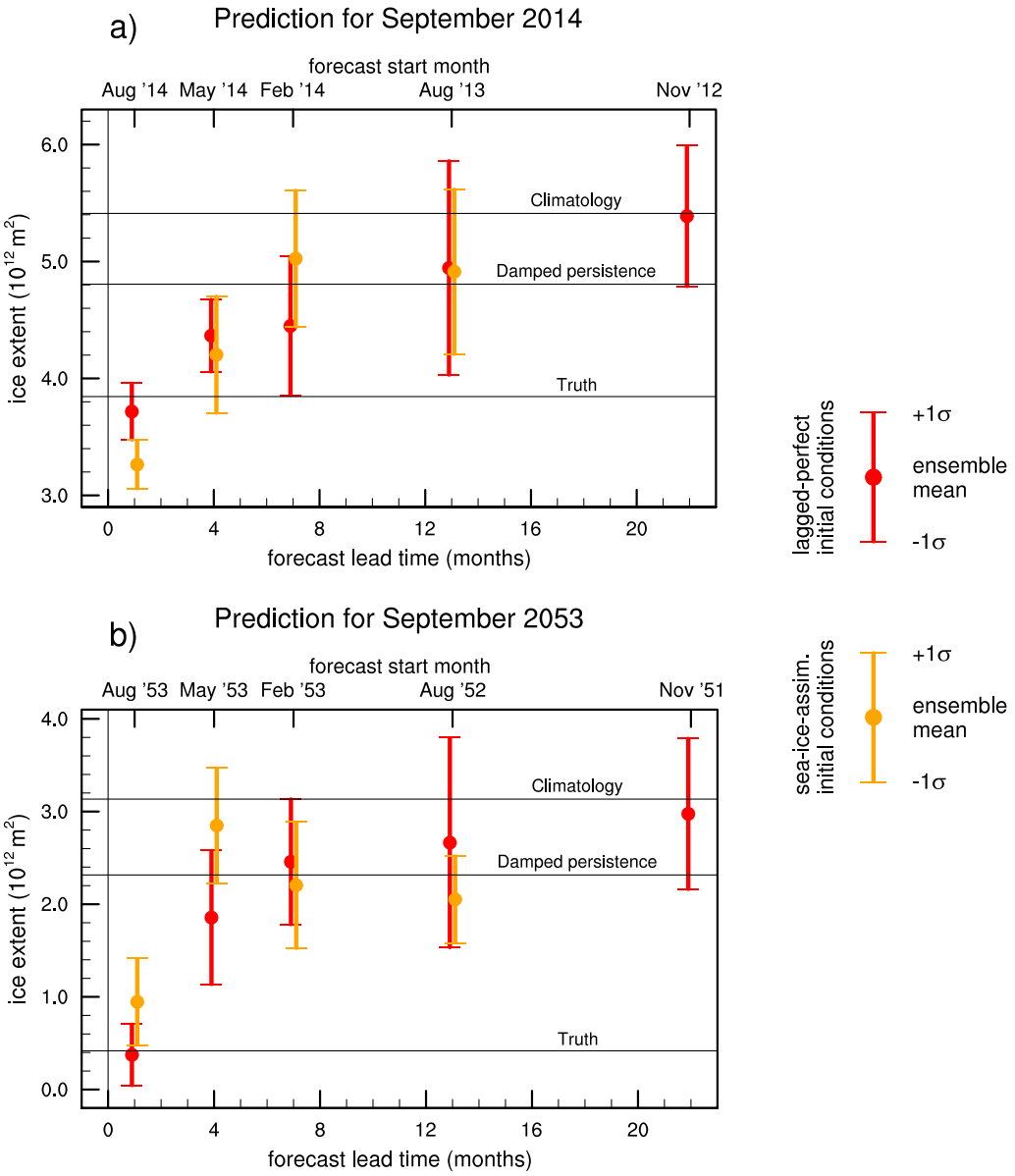

Figure 4.10: Predicted ice extent at different lead times for exceptionally low September sea ice in case studies for (a) present-day conditions and (b) mid-century conditions. Shown are prediction ensembles starting from lagged-perfect initial conditions (red) and from sea-ice-assimilated initial conditions (orange). The filled circle represents the ensemble mean, and the vertical lines indicate the standard deviation of the ensemble predictions. The true September extent, the previous-year damped-persistence forecast, and the climatological centered 30-year mean are drawn as horizontal reference lines.

conditions do not converge regularly towards climatology, but show non-monotonous lead-time dependence of the mean error. This is probably due to random errors in the assimilation run that translate into errors in the sea-ice initial conditions. For instance, in April 2053, there is too much sea ice in the assimilation run (not shown), which causes the prediction started in May 2053 to be biased towards too high ice extent.

To condense the information about the prediction from lagged-perfect initial conditions in Fig. 4.10, we present an estimate of the Brier Skill Score as defined in Eq. (4.1) for each lead time, in analogy to the annual-mean predictions from the previous Section. The climatological September value serves as a reference forecast. The mean squared error of the prediction is calculated from the eight ensemble members with lagged-perfect initial conditions, the mean squared error of the climatology is calculated from the known variability around the climatological value assuming a normal distribution.

Fig. 4.11 shows the dependence of BSS on lead time both for ice extent and ice volume and both for the present-day and the mid-century case study. This figure allows us to derive some important statements: (i) The maximal lead time at which we can expect predictive skill at all is two years. This is further evidence that two years is a strong limit on predictability of Arctic summer sea ice and is in agreement with the findings by *Holland et al.* [2010] and *Tietsche et al.* [2011]. (ii) Predictive skill is higher for ice volume than for ice extent. This is in contrast to the results of the annual-mean predictions, and understanding this requires further analysis. Finally, (iii) predictive skill is higher for present-day conditions than for mid-century conditions. This confirms what we find from the annual-mean predictions: sea-ice predictability decreases as the ice cover becomes thinner.

4.6 Outlook

We present estimates of predictive skill that are based on predictions started in a specific climate state at the onset of large negative Arctic sea-ice anomalies. This case-study approach allows us to assess the predictability for a specific climate state and is a convenient test for the usefulness of the sea-ice-assimilated initial conditions.

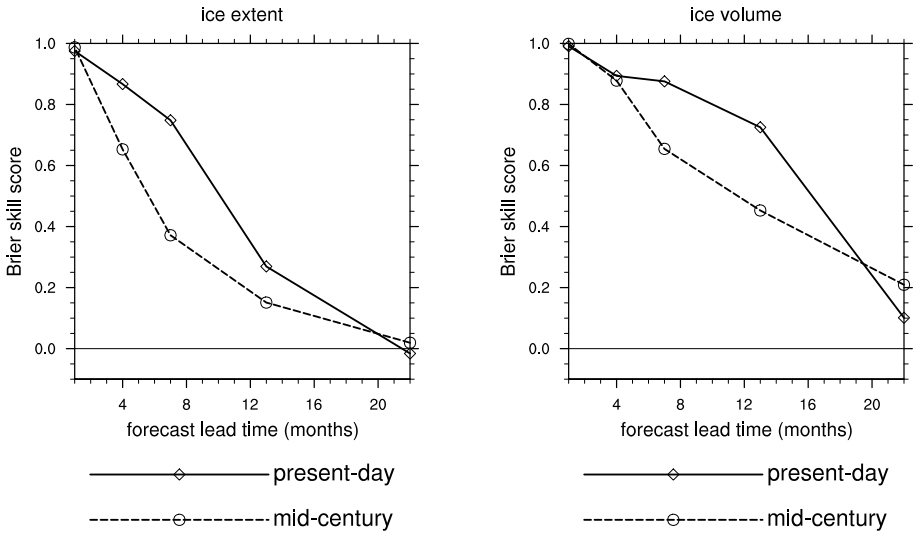

Figure 4.11: Lead-time dependence of Brier skill score for the predictions of exceptionally low September sea-ice conditions. Shown are the scores for sea-ice extent (left) and sea-ice volume (right). The score is calculated for the predictions started from lagged-perfect initial conditions with respect to a climatology forecast.

A complementary study would estimate a generic predictability from predictions started from many different climate states. This generic estimate might differ from the one presented here.

When transferring our results to the prediction of real climate, it is important to remember the idealizing assumptions that we have made: (i) the model is perfect and (ii) the initial conditions are perfectly known. Any prediction of real climate will be less skillful, because (i) the model has limitations in the representation of Arctic climate processes and (ii) the initialization of the model with the observed climate state is imperfect.

A natural continuation of the research presented here would be to determine the predictability of other Arctic climate variables from the same experiments. This would confirm or oppose our hypothesis stated in Sec. 4.3 that predictability of Arctic sea ice can be used as a "proxy" for the predictability of Arctic climate.

Using the output of MPI-ESM-LR, it is also possible to investigate the connection of Arctic sea-ice predictability with phenomena outside the Arctic. A prominent example is the recently suggested influence of low Arctic sea-ice minima on anomalously cold Eurasian winters [*Honda et al.*, 2009].

Finally, we see it as an integral part of studying climate predictability to establish the link between the statistical quantification of predictability and the physical processes that govern the predictability. We hypothesize that atmospheric rather than oceanic processes dominate the predictability of Arctic sea ice, as is suggested by the rather short time scales of predictability.

4.7 Summary and Conclusions

To establish upper bounds for predictability of large negative interannual Arctic sea-ice anomalies in a CMIP5-class global climate model, we perform predictions with MPI-ESM-LR under the perfect-model assumption. We compare predictions starting from lagged-perfect initial conditions to predictions that start from sea-ice-assimilated initial conditions under both present-day and mid-century conditions.

We find that the magnitude of an exceptionally low September sea-ice minimum during the maximal expression of the interannual anomaly is hard to predict. While predictive skill is better than a climatology forecast for up to two years lead time, predictive skill is better than a damped-persistence forecast only if predictions are started less than a year in advance.

Predictions of annual-mean northern-hemisphere sea-ice extent and volume show the following generic features when starting at a time when the sea-ice anomaly has already started to develop: They correctly predict the deepening of the anomaly for a lead time of typically one year. After that, they start regressing to the climatological mean. Thus, although such predictions always underestimate the amplitude and temporal extent of the anomaly, they are potentially useful to decide if an observed accelerated sea-ice loss is due to a secular trend or natural variability on interannual to decadal time scales.

By comparing predictions under climate conditions today and in the middle of the 21st century, we find evidence that predictability of Arctic sea ice decreases during its retreat forced by 21st-century climate change. Annual-mean predictions have significantly higher skill in the third lead year for present-day when compared to mid-century conditions, and September predictions have higher skill for seasonal lead times.

Finally, we find that predictions started from sea-ice-assimilated initial conditions are less skillful, but still comparable to, predictions started from lagged-perfect initial conditions. The degradation of skill is small for lead times of up to one year and becomes substantial for longer lead times. This implies that the initialization of the sea-ice state alone allows for skillful predictions of Arctic sea ice with a global climate model for lead times of up to one year.

5 Summary

In this thesis I have discussed the role of initial and boundary conditions on the predictability of Arctic sea ice, and developed a new method to assimilate observed sea-ice conditions in a global climate model. I conclude by giving concise answers to the research questions posed in Chapter 1. For more detail, please refer to the individual conclusions of Chapters 2, 3 and 4.

Recovery mechanisms of sea ice

Does the ice–albedo feedback lead to threshold behavior during the transition of the Arctic Ocean to a seasonally ice-free state? If not, what are the mechanisms that allow the sea-ice to recover from anomalous losses?

From perturbation experiments with ECHAM5/MPI-OM, I conclude that there is no threshold behavior during the retreat of Arctic sea ice. Sea ice recovers from prescribed ice-free conditions at the beginning of summer within typically two years. The perturbation in the large-scale Arctic energy budget is re-reinforced by the ice–albedo effect during the first summer. In winter, however, heat fluxes at the surface, the top and the lateral boundaries of the Arctic atmosphere adapt to compensate for the anomaly. Thus, even a complete loss of Arctic sea ice during a single summer is reversible, as the ice–albedo feedback is alleviated by large-scale recovery mechanisms.

Sea-ice data assimilation

Is it possible to improve the simulation of sea-ice concentration and thickness in a global climate model by assimilating only observations of sea-ice concentration? How do sea-ice concentration and sea-ice thickness inter-

act under different atmospheric and oceanic conditions, and how is this reflected in the choice of appropriate assimilation methods?

I develop a new technique for sea-ice data assimilation in ECHAM5/MPI-OM that is based on Newtonian relaxation of sea-ice concentration to observations and a prescribed proportionality between analysis updates of sea-ice concentration and sea-ice thickness. I show that this method is able to significantly reduce the discrepancy between observed and modelled sea-ice concentration and sea-ice thickness. I construct an ice-energy-balance model to demonstrate that the strong dependence of sea-ice growth on sea-ice concentration needs to be accounted for in the data assimilation. The structure of the model background error gives further support for the newly-developed assimilation method.

Sea-ice predictability

How predictable are large negative interannual anomalies of Arctic sea-ice? How much of this predictability can be realized by using initial conditions obtained by the sea-ice assimilation methods developed in this thesis? How does the change in the mean state during the 21st century affect predictability of the first kind?

I estimate upper limits of Arctic sea-ice predictability by performing ensemble prediction experiments with MPI-ESM-LR under a perfect-model assumption. I find that onset and amplitude of large negative interannual sea-ice anomalies are essentially unpredictable. However, ensemble predictions started from initial conditions where the anomaly has already started to develop correctly predict its deepening for lead times of typically one year. After that, they regress to the climatological mean. Initial conditions obtained with the sea-ice assimilation methods developed in this thesis yield predictive skill comparable to that from lagged-perfect initial conditions for lead times of up to one year. There is evidence that predictability of Arctic sea-ice that comes from initial conditions is higher for present-day conditions than for conditions in the middle of the 21st century.

Bibliography

Arzel, O., T. Fichefet, and H. Goosse (2005), Sea ice evolution over the 20th and 21st centuries as simulated by current AOGCMs, *Ocean Modell.*, *12*, 401–415, doi:10.1016/j.ocemod.2005.08.002.

Bader, J., M. D. S. Mesquita, K. I. Hodges, N. Keenlyside, S. Østerhus, and M. Miles (2011), A review on northern hemisphere sea-ice, storminess and the North Atlantic Oscillation: Observations and projected changes, *Atmospheric Research*, *101*(4), 809–834, doi:10.1016/j.atmosres.2011.04.007.

Bengtsson, L., V. A. Semenov, and O. M. Johannessen (2004), The early twentieth-century warming in the Arctic – a possible mechanism, *J. Climate*, *17*, 4045–4057, doi:10.1175/1520-0442(2004)017<4045:TETWIT>2.0.CO;2.

Bitz, C. M., and G. H. Roe (2004), A mechanism for the high rate of sea ice thinning in the Arctic Ocean, *J. Climate*, *17*, 3623–3632.

Blanchard-Wrigglesworth, E., K. C. Armour, C. M. Bitz, and E. DeWeaver (2011a), Persistence and inherent predictability of Arctic sea ice in a GCM ensemble and observations, *J. Climate*, *24*, 231–250, doi:10.1175/2010JCLI3775.1.

Blanchard-Wrigglesworth, E., C. M. Bitz, and M. M. Holland (2011b), Influence of initial conditions and climate forcing on predicting Arctic sea ice, *Geophys. Res. Lett.*, *38*, L18,503, doi:10.1029/2011GL048807.

Boé, J. L., A. Hall, and X. Qu (2009), September sea-ice cover in the Arctic Ocean projected to vanish by 2100, *Nature Geoscience*, *2*(5), 341–343.

Bouttier, F., and P. Courtier (1999), Data assimilation concepts and methods – training course lecture notes, from http://www.ecmwf.int, accessed 15 Nov 2011.

Box, G. E. P., G. M. Jenkins, and G. C. Reinsel (2008), *Time Series Analysis: Forecasting and Control*, Wiley series in probability and statistics, Wiley.

Branstator, G., and H. Y. Teng (2010), Two limits of initial-value decadal predictability in a CGCM, *J. Climate*, *23*(23), 6292–6311, doi:10.1175/2010JCLI3678.1.

Brovkin, V., T. Raddatz, C. H. Reick, M. Claussen, and V. Gayler (2009), Global biogeophysical interactions between forest and climate, *Geophys. Res. Lett.*, *36*, L07,405, doi:10.1029/2009GL037543.

Budikova, D. (2009), Role of Arctic sea ice in global atmospheric circulation: A review, *Global and Planetary Change*, *68*(3), 149–163, doi: 10.1016/j.gloplacha.2009.04.001.

Cavalieri, D., C. Parkinson, P. Gloersen, and H. J. Zwally (1996, updated 2008), Sea ice concentrations from Nimbus-7 SMMR and DMSP SSM/I passive microwave data, from http://nsidc.org/data/nsidc-0051.html, accessed 15 Nov 2011.

Chapman, W. L., and J. E. Walsh (2007), Simulations of Arctic temperature and pressure by global coupled models, *J. Climate*, *20*(4), 609–632, doi: 10.1175/JCLI4026.1.

Collins, M., and M. R. Allen (2002), Assessing the relative roles of initial and boundary conditions in interannual to decadal climate predictability, *J. Climate*, *15*, 3104–3109.

Dulière, V., and T. Fichefet (2007), On the assimilation of ice velocity and concentration data into large-scale sea ice models, *Ocean Science*, *3*(2), 321–335.

Eisenman, I., and J. S. Wettlaufer (2009), Nonlinear threshold behavior during the loss of Arctic sea ice, *Proc. Nat. Acad. Sci. USA*, *106*(1), 28–32, doi: 10.1073/pnas.0806887106.

Gloersen, P. (1995), Modulation of hemispheric sea-ice cover by ENSO events, *Nature*, *373*(6514), 503–506, doi:10.1038/373503a0.

Goosse, H., O. Arzel, C. M. Bitz, A. de Montety, and M. Vancoppenolle (2009), Increased variability of the Arctic summer ice extent in a warmer climate, *Geophys. Res. Lett.*, *36*, L23,702, doi:10.1029/2009GL040546.

Hermanson, L., and R. T. Sutton (2009), Case studies in interannual to decadal climate predictability, *Clim. Dynam.*, doi:10.1007/s00382-009-0672-y.

Hibler III, W. D. (1979), A dynamic thermodynamic sea ice model, *J. Phys. Oceanogr.*, *9*(4), 815–846.

Hoffman, P. F., A. J. Kaufman, G. P. Halverson, and D. P. Schrag (1998), A Neoproterozoic snowball earth, *Science*, *281*(5381), 1342–1346, doi: 10.1126/science.281.5381.1342.

Holland, M. M., C. M. Bitz, and B. Tremblay (2006), Future abrupt reductions in the summer Arctic sea ice, *Geophys. Res. Lett.*, *33*, L23,503, doi: 10.1029/2006GL028024.

Holland, M. M., C. M. Bitz, L.-B. Tremblay, and D. A. Bailey (2008), The role of natural versus forced change in future rapid summer Arctic ice loss, in *Arctic Sea Ice Decline: Observations, Projections, Mechanisms, and Implications*, *Geophys. Monogr. Ser.*, vol. 180, edited by E. T. DeWeaver, C. M. Bitz, and L.-B. Tremblay, pp. 133–150, AGU, Washington D. C.

Holland, M. M., D. A. Bailey, and S. Vavrus (2010), Inherent sea ice predictability in the rapidly changing Arctic environment of the Community Climate System Model, version 3, *Clim. Dynam.*, doi:10.1007/s00382-010-0792-4.

Honda, M., J. Inoue, and S. Yamane (2009), Influence of low Arctic sea-ice minima on anomalously cold Eurasian winters, *Geophys. Res. Lett.*, *36*, L08,707, doi: 10.1029/2008GL037079.

Hurrell, J., G. A. Meehl, D. Bader, T. L. Delworth, B. Kirtman, and B. Wielicki (2009), A unified modeling approach to climate system prediction, *Bull. Amer. Meteor. Soc.*, *90*(12), 1819–1832, doi:10.1175/2009BAMS2752.1.

Johannessen, O. M., and M. W. Miles (2011), Critical vulnerabilities of marine and sea ice-based ecosystems in the high Arctic, *Regional Environmental Change*, *11*, 239–248, doi:10.1007/s10113-010-0186-5.

Jungclaus, J. H., H. Haak, M. Latif, and U. Mikolajewicz (2005), Arctic–North Atlantic interactions and multidecadal variability of the meridional overturning circulation, *J. Climate*, *18*, 4013–4031.

Jungclaus, J. H., N. Keenlyside, M. Botzet, H. Haak, J.-J. Luo, M. Latif, J. Marotzke, U. Mikolajewicz, and E. Roeckner (2006), Ocean circulation and tropical variability in the coupled model ECHAM5/MPI-OM, *J. Climate*, *19*, 3952–3972.

Kalnay, E. (2003), *Atmospheric modeling, data assimilation and predictability*, Cambridge University Press.

Kattsov, V. M., V. E. Ryabinin, J. E. Overland, M. C. Serreze, M. Visbeck, J. E. Walsh, W. Meier, and X. D. Zhang (2010), Arctic sea-ice change: a grand challenge of climate science, *Journal of Glaciology*, *56*(200), 1115–1121.

Kauker, F., T. Kaminski, M. Karcher, R. Giering, R. Gerdes, and M. Vossbeck (2009), Adjoint analysis of the 2007 all time Arctic sea-ice minimum, *Geophys. Res. Lett.*, *36*, L03,707.

Koenigk, T., and U. Mikolajewicz (2008), Seasonal to interannual climate predictability in mid and high northern latitudes in a global coupled model, *Climate Dynamics*, *32*(6), 783–798, doi:10.1007/s00382-008-0419-1.

Koenigk, T., U. Mikolajewicz, H. Haak, and J. Jungclaus (2006), Variability of Fram Strait sea ice export: causes, impacts and feedbacks in a coupled climate model, *Clim. Dynam.*, *26*(1), 17–34, doi:10.1007/s00382-005-0060-1.

Koldunov, N. V., D. Stammer, and J. Marotzke (2010), Present-day Arctic sea ice variability in the coupled ECHAM5/MPI-OM model, *J. Climate*, *23*(10), 2520–2543, doi:10.1175/2009JCLI3065.1.

Kwok, R., and D. A. Rothrock (2009), Decline in Arctic sea ice thickness from submarine and ICESat records: 1958–2008, *Geophys. Res. Lett.*, *36*, L15,501, doi:10.1029/2009GL039035.

Lemke, P. (1987), A coupled one-dimensional sea ice–ocean model, *J. Geophys. Res.*, *92*(C12), 13,164–13,172.

Levermann, A., J. Mignot, S. Nawrath, and S. Rahmstorf (2007), The role of northern sea ice cover for the weakening of the thermohaline circulation under global warming, *J. Climate*, *20*, 4160–4171, doi:10.1175/JCLI4232.1.

Lindsay, R. W., and J. Zhang (2006), Assimilation of ice concentration in an ice–ocean model, *J. Atmos. Oceanic Technol.*, *23*, 742–749, doi:10.1175/JTECH1871.1.

Lisæter, K. A., J. Rosanova, and G. Evensen (2003), Assimilation of ice concentration in a coupled ice–ocean model, using the Ensemble Kalman filter, *Ocean Dynamics*, *53*, 368–388, doi:10.1007/s10236-003-0049-4.

Lorenz, E. N. (1975), The physical bases of climate and climate modelling, in *Climate Predictability*, *GARP Publication Series*, vol. 16, pp. 132–136, WMO.

Marsland, S. J., H. Haak, J. H. Jungclaus, M. Latif, and F. Röske (2003), The Max-Planck-Institute global ocean/sea ice model with orthogonal curvilinear coordinates, *Ocean Modell.*, *5*, 91–127.

Maykut, G. A., and N. Untersteiner (1971), Some results from a time-dependent thermodynamic model of sea ice, *J. Geophys. Res.*, *76*(6), 1550–1575.

McNeall, D., P. R. Halloran, P. Good, and R. A. Betts (2011), Analyzing abrupt and nonlinear climate changes and their impacts, *Wiley Interdisciplinary Reviews-climate Change*, *2*(5), 663–686, doi:10.1002/wcc.130.

Meinshausen, M., et al. (2011), The RCP greenhouse gas concentrations and their extensions from 1765 to 2300, *Climatic Change*, *109*(1), 213–241.

Merryfield, W. J., M. M. Holland, and A. H. Monahan (2008), Multiple equilibria and abrupt transitions in Arctic summer sea ice extent, in *Arctic Sea Ice Decline: Observations, Projections, Mechanisms, and Implications*, *Geophys. Monogr. Ser.*, vol. 180, edited by E. T. DeWeaver, C. M. Bitz, and L.-B. Tremblay, pp. 151–174, AGU, Washington D. C.

Murray, R. J., and I. Simmonds (1995), Responses of climate and cyclones to reductions in Arctic winter sea ice, *J. Geophys. Res.*, *100*(C3), 4791–4806, doi: 10.1029/94JC02206.

Nakamura, N., and A. H. Oort (1988), Atmospheric heat budgets of the polar regions, *J. Geophys. Res.*, *93*(D8), 9510–9524.

Nakićenović, N., et al. (Eds.) (2000), *Special Report on Emissions Scenarios*, Special Reports of the Intergovernmental Panel on Climate Change, 559 pp., Cambridge University Press.

North, G. R. (1984), The small ice cap instability in diffusive climate models, *J. Atmos. Sci.*, *41*(23), 3390–3395.

Notz, D. (2009), The future of ice sheets and sea ice: Between reversible retreat and unstoppable loss, *Proc. Nat. Acad. Sci. USA*, *106*(49), 20,590–20,595, doi: 10.1073/pnas.0902356106.

Ogi, M., I. G. Rigor, M. G. McPhee, and J. M. Wallace (2008), Summer retreat of Arctic sea ice: Role of summer winds, *Geophysical Research Letters*, *35*(24), L24,701, doi:10.1029/2008GL035672.

Parkinson, C. L., and D. J. Cavalieri (2008), Arctic sea ice variability and trends, 1979–2006, *J. Geophys. Res.*, *113*, C07,003, doi:10.1029/2007JC004558.

Pohlmann, H., M. Botzet, M. Latif, A. Roesch, M. Wild, and P. Tschuck (2004), Estimating the decadal predictability of a coupled AOGCM, *J. Climate*, *17*, 4463–4472.

Pohlmann, H., J. H. Jungclaus, A. Köhl, D. Stammer, and J. Marotzke (2009), Initializing decadal climate predictions with the GECCO oceanic synthesis: Effects on the North Atlantic, *J. Climate*, *22*(14), 3926–3938, doi: 10.1175/2009JCLI2535.1.

Raddatz, T. J., C. H. Reick, W. Knorr, J. Kattge, E. Roeckner, R. Schnur, K. G. Schnitzler, P. Wetzel, and J. Jungclaus (2007), Will the tropical land biosphere dominate the climate–carbon cycle feedback during the twenty-first century?, *Clim. Dynam.*, *29*(6), 565–574, doi:10.1007/s00382-007-0247-8.

Rigor, I. G., J. M. Wallace, and R. L. Colony (2002), Response of sea ice to the Arctic Oscillation, *Journal of Climate*, *15*(18), 2648–2663, doi:10.1175/1520-0442(2002)015¡2648:ROSITT¿2.0.CO;2.

Rind, D., R. Healy, C. Parkinson, and D. Martinson (1995), The role of sea ice in $2 \times CO_2$ climate model sensitivity. Part I: The total influence of sea ice thickness and extent, *J. Climate*, *8*, 449–463.

Roeckner, E., et al. (2003), The atmospheric general circulation model ECHAM5, *Tech. Rep. 349*, Max Planck Institute for Meteorology, Hamburg.

Royer, J. F., S. Planton, and M. Déqué (1990), A sensitivity experiment for the removal of Arctic sea ice with the French spectral general circulation model, *Clim. Dynam.*, *5*, 1–17.

Saha, S., et al. (2010), The NCEP climate forecast system reanalysis, *Bull. Amer. Meteor. Soc.*, *91*(8), 1015–1057, doi:10.1175/2010BAMS3001.1.

Schröder, D., and W. M. Connolley (2007), Impact of instantaneous sea ice removal in a coupled general circulation model, *Geophys. Res. Lett.*, *34*(14), L14,502, doi: 10.1029/2007GL030253.

Schwierz, C., C. Appenzeller, H. C. Davies, M. A. Liniger, W. Mller, T. F. Stocker, and M. Yoshimori (2006), Challenges posed by and approaches to the study of seasonal-to-decadal climate variability, *Clim. Change*, *79*, 31–63, doi: 10.1007/s10584-006-9076-8.

Screen, J. A., and I. Simmonds (2010), The central role of diminishing sea ice in recent Arctic temperature amplification, *Nature*, *464*(7293), 1334–1337.

Semtner, A. J. (1976), A model for the thermodynamic growth of sea ice in numerical investigations of climate, *J. Phys. Oceanogr.*, *6*, 379–389.

Serreze, M. C., and J. A. Francis (2006), The Arctic amplification debate, *Clim. Change*, *76*, 241–264, doi:10.1007/s10584-005-9017-y.

Serreze, M. C., M. M. Holland, and J. Stroeve (2007a), Perspectives on the Arctic's shrinking sea-ice cover, *Science*, *315*(5818), 1533–1536, doi: 10.1126/science.1139426.

Serreze, M. C., A. P. Barrett, A. G. Slater, M. Steele, J. Zhang, and K. E. Trenberth (2007b), The large-scale energy budget of the Arctic, *J. Geophys. Res.*, *112*, D11,122, doi:10.1029/2006JD008230.

Shepherd, T. G., J. M. Arblaster, C. M. Bitz, T. Furevik, H. Goosse, V. M. Kattsov, J. Marshall, V. Ryabinin, and J. E. Walsh (2011), Report on WCRP workshop on seasonal to multi-decadal predictability of polar climate (Bergen, Norway, 25–29 October 2010), *SPARC Newsletter*, *no. 36*, 11–19.

Sluijs, A., et al. (2006), Subtropical Arctic Ocean temperatures during the Palaeocene/Eocene Thermal Maximum, *Nature*, *441*(7093), 610–613, doi: 10.1038/nature04668.

Smith, D. M., S. Cusack, C. Andrew W, C. K. Folland, G. R. Harris, and J. M. Murphy (2007), Improved surface temperature prediction for the coming decade from a global climate model, *Science*, *317*, 796–799, doi:10.1126/science.1139540.

Stark, J. D., J. Ridley, M. Martin, and A. Hines (2008), Sea ice concentration and motion assimilation in a sea ice–ocean model, *J. Geophys. Res.*, *113*, C05S91, doi:10.1029/2007JC004224.

Taylor, K. E., R. J. Stouffer, and G. A. Meehl (2011), A summary of the CMIP5 experiment design, *Tech. rep.*, IPCC.

Tietsche, S., D. Notz, J. H. Jungclaus, and J. Marotzke (2011), Recovery mechanisms of Arctic summer sea ice, *Geophys. Res. Lett.*, *38*, L02,707, doi: 10.1029/2010GL045698.

Tonboe, R., and E. Nielsen (2010), Global sea ice concentration reprocessing validation report, *Tech. rep.*, Danish Meteorological Institute.

von Storch, H., and F. W. Zwiers (1999), *Statistical Analysis in Climate Research*, Cambridge University Press.

Wetzel, P., A. Winguth, and E. Maier-Reimer (2005), Sea-to-air CO_2 flux from 1948 to 2003: A model study, *Global Biogeochemical Cycles*, *19*(2), GB2005, doi: 10.1029/2004GB002339.

Winton, M. (2006), Does the Arctic sea ice have a tipping point?, *Geophys. Res. Lett.*, *33*, L23,504, doi:10.1029/2006GL028017.

Winton, M. (2008), Sea ice-albedo feedback and nonlinear Arctic climate change, in *Arctic Sea Ice Decline: Observations, Projections, Mechanisms, and Implications*, *Geophys. Monogr. Ser.*, vol. 180, edited by E. T. DeWeaver, C. M. Bitz, and L.-B. Tremblay, pp. 111–131, AGU, Washington D. C.

Woodgate, R. A., T. Weingartner, and R. Lindsay (2010), The 2007 Bering Strait oceanic heat flux and anomalous Arctic sea-ice retreat, *Geophys. Res. Lett.*, *37*, L01,602, doi:10.1029/2009GL041621.

Yi, D., and J. Zwally (2010), Arctic sea ice freeboard and thickness, from http://nsidc.org/data/nsidc-0393.html, accessed 15 Nov 2011.

Acknowledgements

First and foremost, I wish to thank Jochem Marotzke and Dirk Notz for being excellent scientific mentors throughout my PhD. They always granted me the great privilege to follow my own curiosity in research, but shared their insight and advice with me whenever I needed it. I thank Johann Jungclaus for his steady support as a co-adviser and Bjorn Stevens for chairing my PhD panel.

Many thanks to all the colleagues at the MPI for the innumerable occasions when I profited from their experience and knowledge. I am especially indebted to Wolfgang Müller, Helmuth Haak, Daniela Matei and Thorsten Mauritsen for many fruitful discussions.

I would like to thank Antje and Connie for filling the IMPRS-ESM with life and providing so much support with so much personal commitment. It is really them who make the IMPRS-ESM an outstanding environment to do a PhD.

Many thanks to all my fellow PhD students that made the time here as enjoyable as it was. Special thanks to Aiko Voigt, Nils Fischer, Florian Rauser, Korbinian Freier, Daniel Klocke, Laura Niederdrenk, Werner Bauer and Peter Düben for the many coffee and lunch breaks, when we indulged ourselves either in crazy jokes or grand disputes about science and how to save the world. A very special thanks goes to my roommates Mario Krapp and Jaison Ambadan, who shared all the good and the tough moments with me.

Finally, I am deeply grateful to my family for their steady love and support, and to Fanny, for being the sun in my life.



ISSN 1614-1199